CONSTRAINING DARK MATTER THROUGH COSMOLOGICAL OBSERVATIONS

A Dissertation

by

STEVEN JAMES CLARK

Submitted to the Office of Graduate and Professional Studies of
Texas A&M University
in partial fulfillment of the requirements for the degree of

DOCTOR OF PHILOSOPHY

Chair of Committee,	Bhaskar Dutta
Co-Chair of Committee,	Louis E. Strigari
Committee Members,	Stephen A. Fulling
	Teruki Kamon
Head of Department,	Grigory Rogachev

August 2019

Major Subject: Physics

ABSTRACT

While gravitational effects of dark matter are observed at galactic and larger scales, other behaviors are more elusive. Two approaches for extra-solar studies of dark matter interaction are from an energy perspective and through spectral searches. Energy injections into the intergalactic medium over the age of the Universe from exotic interactions, including dark matter, result in a perturbed gas evolution which has measurable impacts on both the cosmic microwave background (CMB) as well as the 21 cm absorption line. Sizable particle spectra are also produced in areas of dense matter concentrations. This work studies the effects of energy injections and spectral signals in the context of dark matter, and limits are placed on multiple models using results from *Planck*, Fermi-LAT, MAGIC, VERITAS, AMS, and EDGES. Decaying dark matter is well constrained by 21 cm absorption, especially for $2e$ and 2γ modes and most models with dark matter lighter than 20 GeV. Primordial black hole evaporation strongly affects both the CMB and the 21 cm line; while the limits from CMB measurements are comparable to current leading bounds, those from 21 cm absorption are an order of magnitude stronger. In four-body annihilation models, spectral signals weaken slightly while the CMB remains mostly unchanged. Gauge boson bremsstrahlung annihilation improves the reach of velocity suppressed model searches with spectral signals from the galactic center proving the most stringent.

DEDICATION

To my mother for all of her support through the years; my father, an example to live up to; and my wife, my rock in recent time.

ACKNOWLEDGMENTS

We acknowledge the Texas A&M University Brazos HPC cluster that contributed to the research presented here.

The contents of this work first appeared in the following articles and have been reproduced with permission:

S. Clark, B. Dutta, Y. Gao, L. E. Strigari, and S. Watson, "Planck Constraint on Relic Primordial Black Holes," *Phys. Rev.* **D95** no. 8, (2017) 083006, arXiv:1612.07738 [astro-ph.CO]. © 2017 American Physical Society

S. J. Clark, B. Dutta, and L. E. Strigari, "Dark Matter Annihilation into Four-Body Final States and Implications for the AMS Antiproton Excess," *Phys. Rev.* **D97** no. 2, (2018) 023003, arXiv:1709.07410 [astro-ph.HE]. © 2018 American Physical Society

S. Clark, B. Dutta, Y. Gao, Y.-Z. Ma, and L. E. Strigari, "21 cm limits on decaying dark matter and primordial black holes," *Phys. Rev.* **D98** no. 4, (2018) 043006, arXiv:1803.09390 [astro-ph.HE]. © 2018 American Physical Society

S. J. Clark, J. B. Dent, B. Dutta, and L. E. Strigari, "Indirect detection of the partial p wave via the s wave in the annihilation cross section of dark matter," *Phys. Rev.* **D99** no. 8, (2019) 083003, arXiv:1901.01454 [hep-ph]. Published by the American Physical Society.

CONTRIBUTORS AND FUNDING SOURCES

Contributors

This work was supported by a dissertation committee consisting of Professors Bhaskar Dutta [advisor], Louis Strigari [co-advisor], and Teruki Kamon of the Department of Physics and Astronomy and Professor Stephen Fulling of the Department of Mathematics.

Work for the dissertation was conducted by the student in collaboration with Professors Bhaskar Dutta and Louis Strigari of the Department of Physics and Astronomy as well as Professors Yu Gao of the Chinese Academy of Sciences, Yin-Zhe Ma of the University of KwaZulu-Natal, and Scott Watson of Syracuse University.

Funding Sources

Graduate study was supported by the Graduate Merit Fellowship from Texas A&M University. We also acknowledge support from the NASA Astrophysics Theory grant NNX12AC71G and the DOE grant de-sc001081.

TABLE OF CONTENTS

Page

Page

LIST OF FIGURES

FIGURE Page

FIGURE Page

LIST OF TABLES

TABLE Page

1. INTRODUCTION

Dark matter composes over 20% of the Universe today. However, its very nature makes it difficult to measure; as such, there are numerous models that aim to describe its properties. These models can be tested through experimental approaches ranging from direct detection, measuring dark matter interactions with the detector; collider experiments, searching for dark matter creation through missing energy in a high energy particle collision; and indirect detection, looking for the effects of dark matter on other structures such as galaxies or the entire Universe.

Different dark matter models can be probed and have their parameter spaces constrained by current high energy experiments. In this work, we focus on probing different well-motivated models through numerous indirect detection methods. These constraints are imposed by searching experimental results for deviations from the standard. Experiments of particular interest for this work are *Planck* [1], EDGES [2, 3], and Fermi [4–8] as they allow for different approaches to be considered and produce complimentary limits.

Planck measured the cosmic microwave background (CMB), an imprint of the Universe at redshift $z \approx 1100$ as photon radiation decoupled from matter. Dark matter interacted during this time and injected energy into the Universe, thus increasing the ionization fraction and the temperature of the intergalactic medium. These in turn changed how the CMB formed and propagated.

EDGES measured the 21 cm absorption line, a photon spectral feature associated with the Hydrogen hyperfine structure corresponding to the energy involved in flipping a Hydrogen electron's spin. The absorption line is produced once the Universe has cooled sufficiently, $z \approx 20$. The line is also sensitive to the gas temperature; as it increases, the amount of absorption decreases. This feature is of particular interest because it allows for a probe of the "dark ages" before star and galaxy formation.

Dark matter interactions also produce their own spectra which contributes to the cosmic ray flux. Fermi-LAT measured the gamma-ray flux for the entire sky which is used to constrain dark matter interactions by searching for particle flux greater than the predicted background. The galactic center and dwarf spheroidal satellite galaxies are locations of particular interest for these searches as they contain a high expected signal rate or a low background, respectively.

In this work, we use experimental results to place constraints on different decaying and annihilating dark matter models, as well as investigate the fraction of dark matter content that may be composed of primordial black holes (PBH), a black hole that formed in the early Universe. In Sec. 2, we describe the process by which energy is injected into the Universe by different dark matter interactions, describe the efficiencies of different absorption processes (Sec. 2.1) and look at their effect on the CMB (Sec. 2.3) and the 21 cm absorption line (Sec. 2.4). Sec. 3 investigates methods by which we may use the spectra produced by dark matter interactions produced in our galaxy (Sec. 3.1) and in satellite dwarf spheroidal galaxies (Sec. 3.2). Descriptions and constraints for the different models explored are presented in Sec. 4. The individual models investigated are decaying dark matter (Sec. 4.1), primordial black holes (Sec. 4.2), annihilating dark matter into two- and four-body final states (Sec. 4.3), and dark matter annihilation via a bremsstrahlung gauge boson (Sec. 4.4). The results are summarized in the conclusion (Sec. 5).

2. ENERGY DEPOSITION IMPRINTS*

The ΛCDM model provides a good description for the evolution of the Universe as it expanded and cooled. It includes all Standard Model particle interactions; any additional particle interaction not included that couples to the Standard Model will interact with the intergalactic medium (IGM). For our purposes, the IGM includes all matter in the Universe. These interactions transfer energy to the Universe, affecting its evolution. Dark matter interactions that couple to the Standard Model are no different. With the additional energy source provided by these interactions, perturbations to the Universe's standard history will form, and they will leave an imprint observable today. [9–16]

The Universe's evolution can be contained within two parameters: the history of the ionization fraction, x_e, and the IGM temperature, $T_{\rm IGM}$. The total amount of energy injected into the Universe will vary depending on the daughter products in the additional interactions. We will present the particular form of the injection rate for the different models investigated later in their respective sections. For now, we will simply express the injection rate by its simple symbolic definition, $\mathrm{d}E/\mathrm{d}V\mathrm{d}t$, the differential rate at which energy enters the system over time and volume. While we will discuss the energy injections under the assumption that they are being produced by dark matter,

*Parts of this section are reprinted with permission from:

S. Clark, B. Dutta, Y. Gao, L. E. Strigari, and S. Watson, "Planck Constraint on Relic Primordial Black Holes," *Phys. Rev.* **D95** no. 8, (2017) 083006, arXiv:1612.07738 [astro-ph.CO]. © 2017 American Physical Society

S. J. Clark, B. Dutta, and L. E. Strigari, "Dark Matter Annihilation into Four-Body Final States and Implications for the AMS Antiproton Excess," *Phys. Rev.* **D97** no. 2, (2018) 023003, arXiv:1709.07410 [astro-ph.HE]. © 2018 American Physical Society

S. Clark, B. Dutta, Y. Gao, Y.-Z. Ma, and L. E. Strigari, "21 cm limits on decaying dark matter and primordial black holes," *Phys. Rev.* **D98** no. 4, (2018) 043006, arXiv:1803.09390 [astro-ph.HE]. © 2018 American Physical Society

S. J. Clark, J. B. Dent, B. Dutta, and L. E. Strigari, "Indirect detection of the partial p wave via the s wave in the annihilation cross section of dark matter," *Phys. Rev.* **D99** no. 8, (2019) 083003, arXiv:1901.01454 [hep-ph]. Published by the American Physical Society.

the approach presented is valid for any new energy interaction with the IGM.

The energy produced by additional interactions add pressure to the evolution of x_e and $T_{\rm IGM}$ by inducing an increased level of ionization and gas heating. These additions are described by [14, 16–19]

$$\frac{\mathrm{d}x_e}{\mathrm{d}z} = \left(\frac{\mathrm{d}x_e}{\mathrm{d}z}\right)_{\rm orig} - \frac{1}{(1+z)H(z)}(I_{\rm i}(z) + I_\alpha(z)), \tag{2.1}$$

$$\frac{\mathrm{d}T_{\rm IGM}}{\mathrm{d}z} = \left(\frac{\mathrm{d}T_{\rm IGM}}{\mathrm{d}z}\right)_{\rm orig} - \frac{2}{3k_{\rm B}(1+z)H(z)}\frac{K_{\rm h}(z)}{1+f_{\rm He}+x_e}, \tag{2.2}$$

where $(\mathrm{d}x_e/\mathrm{d}z)_{\rm orig}$ and $(\mathrm{d}T_{\rm IGM}/\mathrm{d}z)_{\rm orig}$ are the standard recombination equations without additional energy injections and are described in detail in Ref. [16, 17] and are shown in Equations 2.7 and 2.8 for convenience. $H(z)$ is the Hubble parameter, $k_{\rm B}$ is the Boltzmann constant, and $f_{\rm He}$ is the helium fraction. $I_{\rm i}$, I_α, and $K_{\rm h}$ are factors that relate energy injection to hydrogen's ground state ionization, Lyman-α excited hydrogen ionization, and heating the gas respectfully. They have the form [16]

$$I_{\rm i}(z) = f_{\rm i}(E,z)\frac{\mathrm{d}E/\mathrm{d}V\mathrm{d}t}{n_{\rm H}(z)E_{\rm i}}, \tag{2.3}$$

$$I_\alpha(z) = f_\alpha(E,z)(1-C)\frac{\mathrm{d}E/\mathrm{d}V\mathrm{d}t}{n_{\rm H}(z)E_\alpha}, \tag{2.4}$$

$$K_{\rm h}(z) = f_{\rm h}(E,z)\frac{\mathrm{d}E/\mathrm{d}V\mathrm{d}t}{n_{\rm H}(z)}, \tag{2.5}$$

$$C = \frac{1+K\Lambda_{2s,1s}n_{\rm H}(1+x_{\rm e})}{1+K\Lambda_{2s,1s}n_{\rm H}(1-x_{\rm e})+K\beta_{\rm B}n_{\rm H}(1-x_{\rm e})}. \tag{2.6}$$

where $\mathrm{d}E/\mathrm{d}V\mathrm{d}t$ is the energy injection from the interaction method. The particular form for each model will be discussed in their individual sections. $n_{\rm H}$ is the hydrogen number density. $E_{\rm i}$ and E_α are respectfully the energy required to ionize the ground and first excited energy states in hydrogen. $\Lambda_{2s,1s}$ is the decay rate from the $2s$ to $1s$ energy level. $\beta_{\rm B}$ is the effective photoionization rate, and $K = \lambda_\alpha^3/(8\pi H(z))$, with λ_α as the Lyman-α wavelength. C is a parameter relating to the probability that an

excited hydrogen electron will decay through two-photon emission before being ionized. Collisional de-excitation effects are subdominate and not included [15, 16, 20]. $f_c(E, z)$ with $c = \mathrm{i}, \alpha, \mathrm{h}$ are effective efficiencies [19, 21] for the injection to be absorbed into different channels. Because the injections for masses considered here are relativistic, energy injected into the gas may not be absorbed until a later redshift. This results in energy absorption produced during different epochs occurring at the same time. $f_c(E, z)$ encapsulates this behavior and is defined as the ratio of energy absorbed to the amount injected into the IGM at a given redshift. This energy pile-up effect can cause the effective efficiency to be greater than one. The procedure used for calculating the effective efficiencies will be discussed in Sec. 2.1.

As stated earlier, the terms with lower script "orig" in Equations 2.1 and 2.2 refer to the unaltered standard evolution equations [16, 17],

$$\left(\frac{\mathrm{d}x_e}{\mathrm{d}z}\right)_{\mathrm{orig}} = \frac{C}{(1+z)H(z)} \times (x_{\mathrm{e}}^2 n_{\mathrm{H}} \alpha_{\mathrm{B}} - \beta_{\mathrm{B}}(1-x_{\mathrm{e}}) e^{-h\nu_{2s}/k_{\mathrm{B}}T_{\mathrm{G}}}), \tag{2.7}$$

$$\left(\frac{\mathrm{d}T_{\mathrm{IGM}}}{\mathrm{d}z}\right)_{\mathrm{orig}} = \frac{8\sigma_{\mathrm{T}} a_{\mathrm{R}} T_{\mathrm{CMB}}^4}{3 m_{\mathrm{e}} c H(z)(1+z)} \frac{x_{\mathrm{e}}}{1+f_{\mathrm{He}}+x_{\mathrm{e}}} (T_{\mathrm{G}} - T_{\mathrm{CMB}}), \tag{2.8}$$

where α_{B} is the effective recombination rate. These equations describe the interactions between neutral and ionized hydrogen gas as it cools and thermalizes. Dark matter energy injections provide additional pressure that leads to increased ionization and heating. One outcome of the injections is an increase to the surface of last scattering for photons that will make up the CMB.

2.1 Effective Efficiency

In the formalism presented in Sec. 2, all interaction transient behavior has been combined into the effective efficiency for each absorption channel, $f_c(E, z)$. These have been calculated previously for photon and electron injections into several channels of interest [19, 21]. Previously, effective efficiencies have been approximated by simple x_e dependent equations where the energy injection is taken to be instantaneous. This

technique is known as the "SSCK" method and is described in further detail in Ref. [16, 22]. This approach does not incorporate the pile-up features that were discussed earlier. Here we extend upon the analyses from Ref. [19, 21] to include additional interactions, and also expand the effective efficiency calculation to higher energies. In particular, we will be describing trends that arise in general when calculating an effective efficiency from a spectra and leave any model specific properties for their individual discussion.

The various $f_c(E, z)$ equations are complex, developed from the interactions of high energy particles with the IGM as they thermalize with the environment. They are species, energy, redshift, and channel dependent. However, the effective efficiency of a specific interaction can be simplified by first determining the individual effective efficiencies for single long lived products, principally photons, electrons, neutrinos, protons, and their antiparticles, as well as the spectra of these products for the particular interaction of interest. The single efficiencies and the spectra are then combined into an effective efficiency for the interaction through

$$f_c(m_\chi, z) = \frac{\sum_s \int f_c(E, z)_s E(\mathrm{d}N/\mathrm{d}E)_s \mathrm{d}E}{\sum_s \int E(\mathrm{d}N/\mathrm{d}E)_s \mathrm{d}E}, \tag{2.9}$$

where s is the particle species, c is the channel by which the energy is absorbed by the environment, E is the initial injection energy, $(\mathrm{d}N/\mathrm{d}E)_s$ is the particle spectrum, and $f_c(E, z)$ is the effective efficiency for this particular particle [23]. For our analysis, we use the effective efficiencies for electrons and photons calculated in Refs. [19, 21]. Also similar to these authors, we set the neutrino and proton efficiencies to be zero. This assumption is warranted for neutrinos interact weakly with the IGM and protons do not significantly impact the CMB [11]. We also assume that unstable particles produced in the initial interaction decay instantaneously; all medium interactions are solely attributed to stable decay products.

For some of the efficiency calculations performed, it is necessary to include injections

greater than those presented in Ref. [21] requiring the additional assumption that the efficiency remains constant at high energies. This assumption is supported by Ref. [22]. They observed that the efficiency asymptotes to a constant at high energies as the dominant behavior becomes a pair production/Inverse Compton scattering cascade.

To provide a descriptive example for effective efficiency calculations, we will consider annihilation cascade models with two- and four-body final states as an illustrative example. The particulars of these models will be discuss in more detail later. We calculate the spectra of stable products with PYTHIA [24–26]. Results from our calculation for several representative cases are shown in Figure 2.1. Unless explicitly stated, we assume that the mass of the mediator is related to the mass of the dark matter as $m_\phi = m_\chi/2$. The four-body interactions are $\chi\chi \to \phi\phi$ where the ϕ then decays into two Standard Model particles. Also, while we assume ϕ is a scalar, the constraints imposed are equally valid for a vector particle. From Figure 2.1, we note that quark and lepton spectra are very similar to other quark and lepton spectra regardless of flavor or the number of final products. As an extension, this indicates that their efficiencies should also be similar. Also of note, because only photons and electrons interact strongly with the IGM, energy that is deposited into the proton and neutrino spectra is be associated with missing energy and will result in a reduction to the interaction's efficiency. Furthermore, electroweak corrections [26, 27] were not taken into account in these spectral calculations. However, these corrections mainly influence the spectra at low energies and thus will result in only a very minor alteration.

The spectra in Figure 2.1, the efficiencies from Ref. [21], and Equation 2.9, combine to calculate the efficiencies for each interaction. The efficiencies for $\chi\chi \to \phi\phi$ followed by $\phi \to b\bar{b}$ are shown in Figure 2.2. Other interactions have a nearly identical structure, where the primary difference between each interaction is a shift in the magnitude of the efficiency. This is a result of more energetic particles receiving a larger weight due to the calculation being an energy efficiency map explained in more detail below.

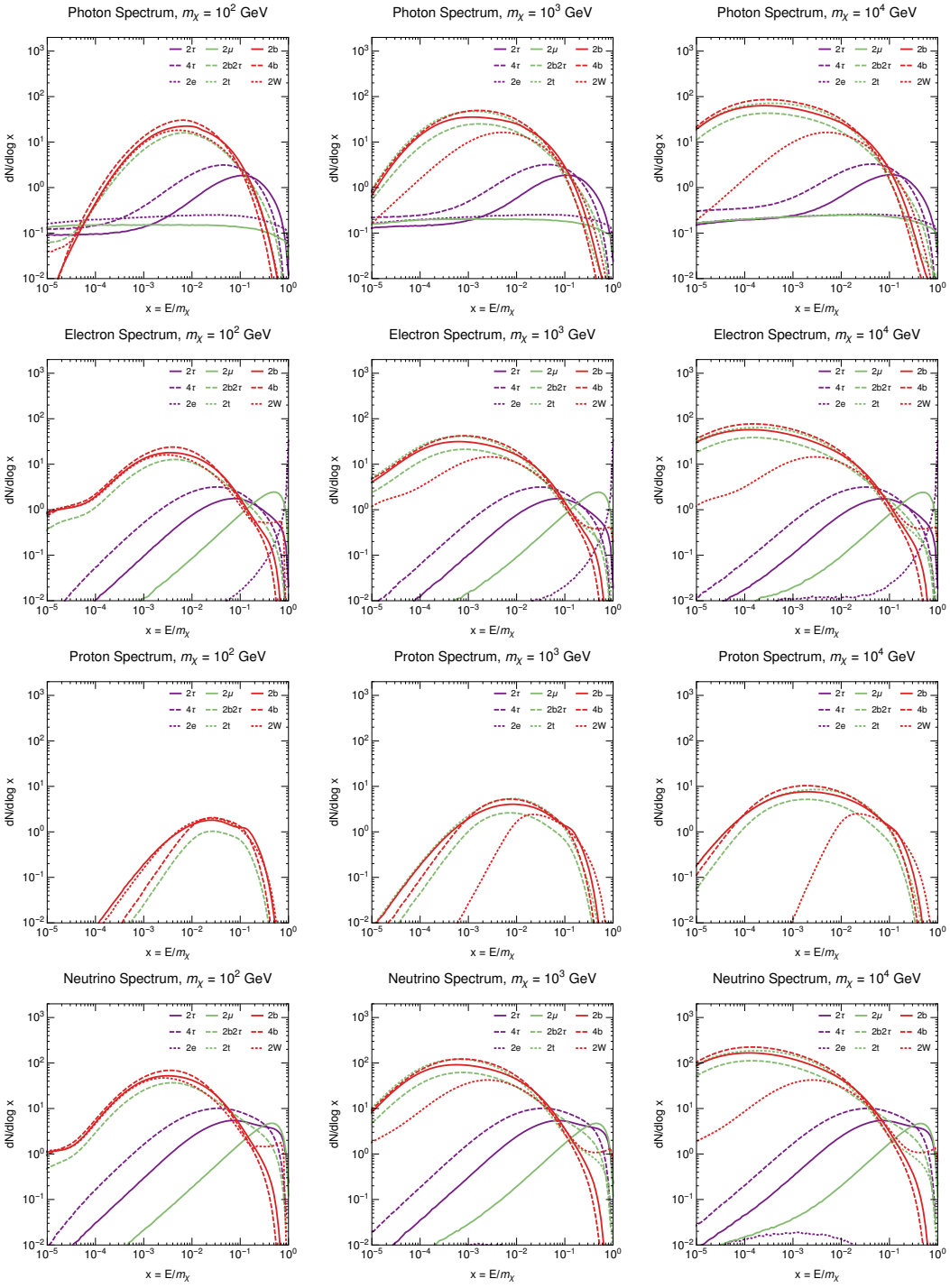

Figure 2.1: Two- and four-body annihilation spectra for various channels. E is the particle's kinetic energy. Spectra: (top to bottom) photon, electron, proton, neutrino. Dark matter mass: (left to right) 10^2, 10^3, 10^4 GeV. The spectra from the various quark channels are all very similar in both magnitude and shape. Reprinted with permission from Ref. [28].

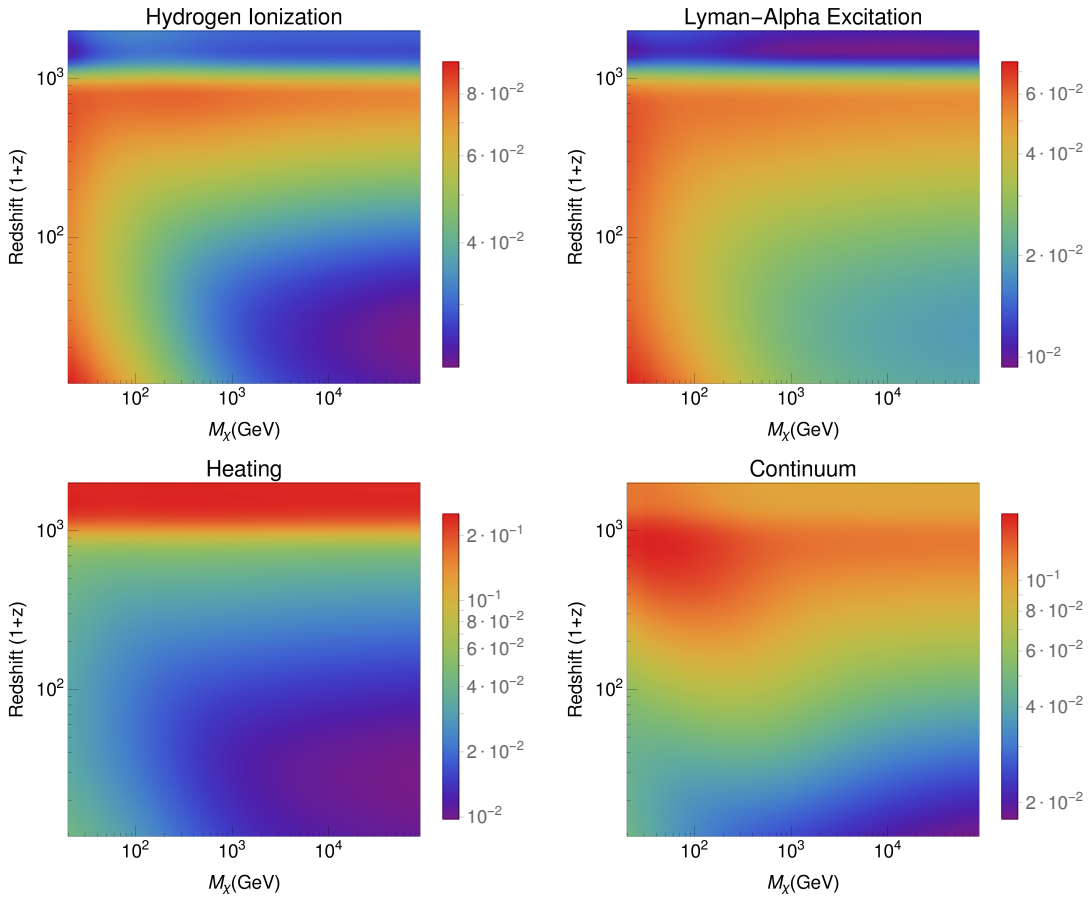

Figure 2.2: Effective efficiency maps for dark matter annihilation to $4b$. The $4b$ interaction is $\chi\chi \to \phi\phi$ followed by $\phi \to b\bar{b}$. Different annihilation interactions have a map with a nearly identical structure but with slight differences in amplitude as seen in Figure 2.3. Reprinted with permission from Ref. [28].

Another important feature is, at a single redshift, the efficiency is nearly uniform over mass, especially from $z = 200 - 1000$. As a result, the constraints established by this energy injection have a simple dependence on dark matter mass.

Figure 2.3 shows the effective efficiency as a function of redshift for various channels calculated with a dark matter mass of 10^3 GeV. The redshift dependence for these curves are similar, with the most significant variation coming in their amplitudes. This feature can easily be understood by noting that the efficiency is energy dependent, favoring contributions by higher energy particles. Since the efficiency is a ratio of the

total energy absorbed to the total energy injected into the environment, the higher energy structure of the spectrum contributes the most to the shape of the efficiency, and for all cases, the leading term is the electron injection. Other terms contribute minor alterations, particularly at late times when high energy particles make weaker contributions. The normalization factor is a result of the amount of energy contributing to other products, in particular protons and neutrinos. Since this energy is considered lost in the calculation, any energy entering these channels results in a loss of efficiency.

Another feature that results in the uniformity between the different interaction types and also the various mass ranges is due to the averaging effect that comes from Equation 2.9. While the original efficiencies observed in Ref. [19, 21] have a substantial degree of variance with injection energy, combining efficiencies together with a continuous spectrum results in washing out these features, adding to the similarities observed in Figure 2.3 as well as the near uniform features observed with energy in Figure 2.2.

For convenience and in order to establish a comparison to other works, Table 2.1 provides equivalent average effective efficiencies for an injection following the "SSCK" approach discussed in Ref. [15, 16]. To make a comparison between the values reported in Ref. [16], the hydrogen ionization, Lyman-α excitation, and heating channels were summed into a single efficiency and averaged over $z = 800 - 1000$. The energy absorbed by the environment in our method of utilizing individual channels is comparable to approaches that use a single averaged value provided by similar works at the 5% level.

The trends discussed are fairly constant when high energy particles are created due to increased weight given to the more energetic particles. Even more so, at very high energies, the particles tend to have the same efficiency. Large variations do occur as can be observed on the left side of the efficiency graphs in Figure 2.2. To illustrate these large differences, Figure 2.4 presents the effective efficiencies for primordial black holes emitting Hawking radiation in the $10^{15} - 10^{17}$ g mass range. This is another model that will be considered and is detailed later. The emitted particles are both cooler, resulting

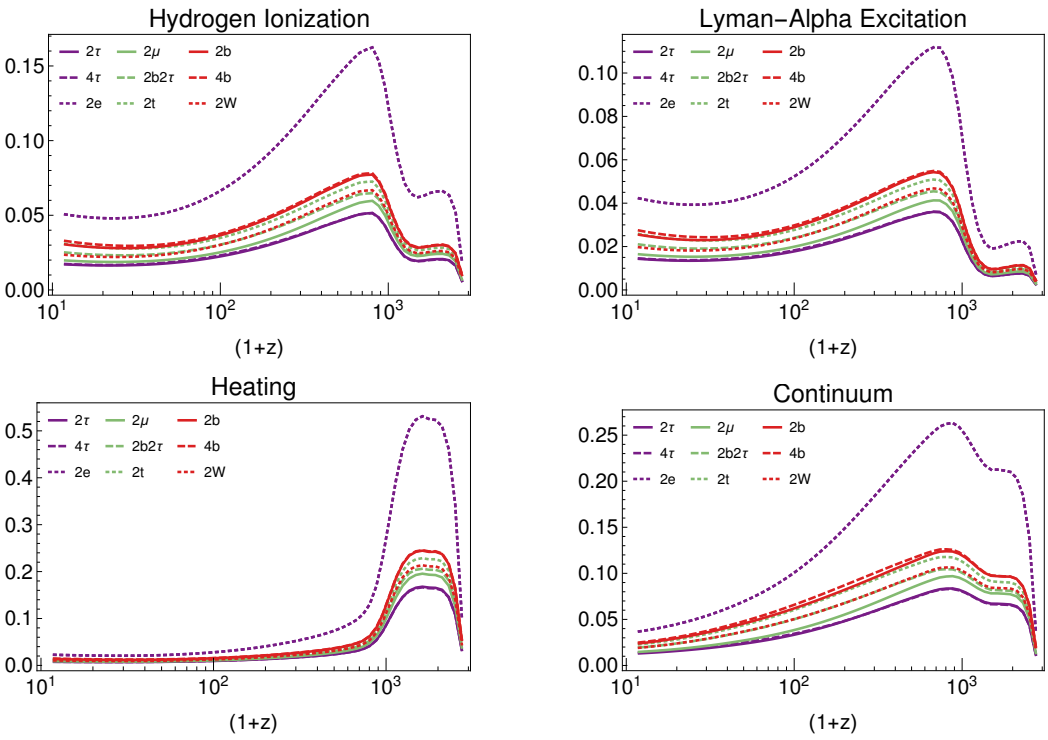

Figure 2.3: Effective efficiency for various annihilation final states for a dark matter mass of 10^3 GeV. The structural features of each channel are nearly identical. Reprinted with permission from Ref. [28].

Annihilation Model	m_χ [GeV]	f_{eff}	Annihilation Model	m_χ [GeV]	f_{eff}
$\chi\chi \to e\bar{e}$	10^2	0.4322	$\chi\chi \to b\bar{b}$	10^2	0.2098
	10^3	0.4290		10^3	0.2036
	10^4	0.4293		10^4	0.1981
$\chi\chi \to \mu\bar{\mu}$	10^2	0.1664	$\chi\chi \to \phi\phi$	10^2	0.2093
	10^3	0.1579	$\phi \to b\bar{b}$	10^3	0.2057
	10^4	0.1604		10^4	0.1989
$\chi\chi \to \tau\bar{\tau}$	10^2	0.1414	$\chi\chi \to \phi\phi$	10^2	0.1446
	10^3	0.1364	$\phi \to \tau\bar{\tau}$	10^3	0.1359
	10^4	0.1381		10^4	0.1367
$\chi\chi \to W^+W^-$	10^2	0.1821	$\chi\chi \to \phi\phi$	10^2	0.1769
	10^3	0.1763	$\phi \to b\bar{b}$ or $\tau\bar{\tau}$	10^3	0.1708
	10^4	0.1720	each at 50% branching ratio	10^4	0.1679
$\chi\chi \to t\bar{t}$	10^3	0.1911			
	10^4	0.1873			

Table 2.1: The integrated channel technique for calculating effective efficiencies compared with the "SSCK" approach. The "SSCK" approach is discussed in detail in Ref. [15, 16]. Reprinted with permission from Ref. [28].

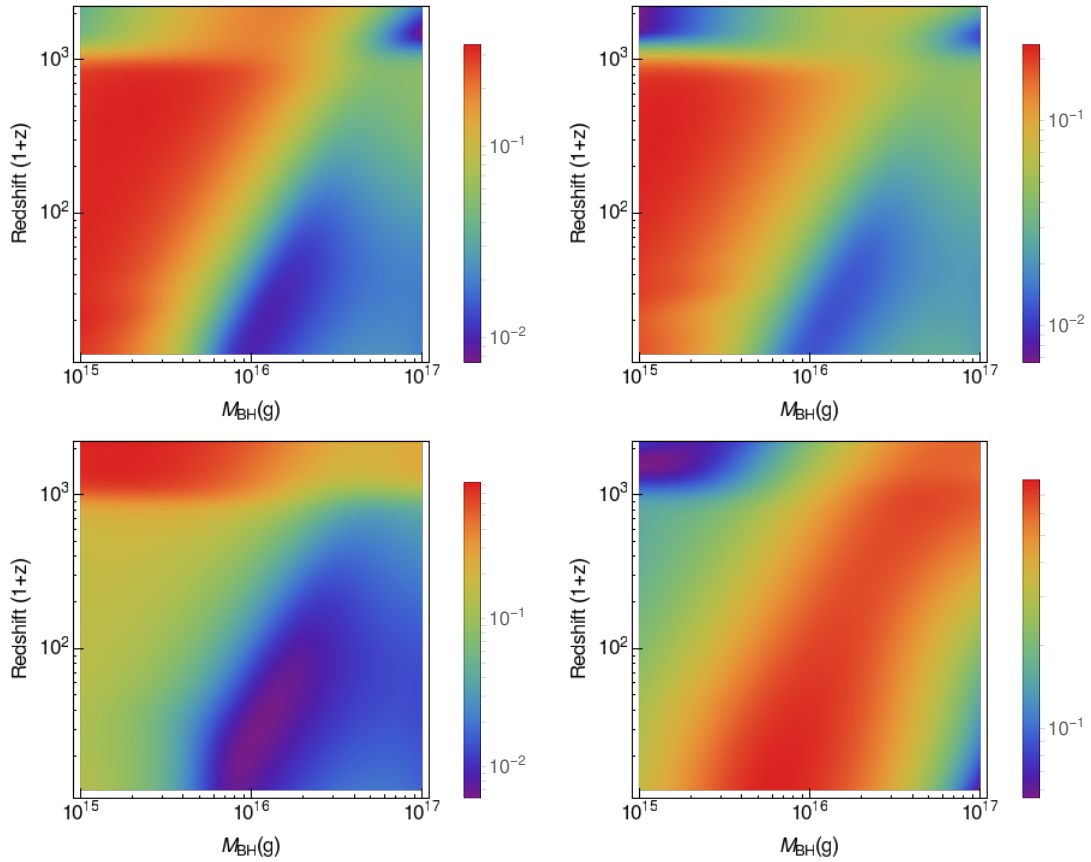

Figure 2.4: Effective efficiency maps for primordial black holes emitting Hawking radiation. Channels: (left to right, top to bottom) hydrogen ionization, Lyman-α excitations, heating, and continuum photons. Reprinted with permission from Ref. [23].

in more variation in the efficiencies, as well as the interaction's redshift dependence is quite different. Black hole radiation is dependent on the black hole number density while annihilation depends upon the number density squared. An interesting feature in the black hole efficiency maps is the quick transition from high efficiency to poor efficiency with increasing mass. This efficiency "edge" also moves with redshift and is observable in some of the experiments discussed below.

2.2 Recombination History

In order to illustrate the effects of energy injections on the Universe, alterations to x_e and $T_{\rm IGM}$ are shown for a few example PBH masses in Figure 2.5. The percent

change relative to the standard is indicated. Figure 2.5 shows that there is only a minor variation relative to the standard case in both x_e and $T_{\rm IGM}$ at large redshifts, with significant deviations only apparent at $\sim z = 200 - 300$. The minimal deviation at high redshift supports the use of the effective efficiencies [22] for high redshift calculations like the CMB described below. In addition, constraints set at later redshifts have the potential to be more stringent by imposing strict behavior. As will be seen in Sec. 2.4, matter temperature variations are even more suppressed. Comparing to direct measurements, x_e and $T_{\rm IGM}$ are both well below observational limits [29–31] for standard values of cosmological parameters,

$$\begin{aligned} x_e(z \sim 7) &= 0.66^{+0.12}_{-0.09} & x_e(z \sim 8) &< 0.35 \\ \log_{10}(T_{\rm IGM}(z = 4.8)) &= 3.9 \pm 0.1 & \log_{10}(T_{\rm IGM}(z = 6.08)) &= 4.21^{+0.06}_{-0.07}. \end{aligned} \tag{2.10}$$

We note that contributions from reionization and structure formation are not included in this calculation, though it may be possible that PBHs around the masses studied can represent a significant contribution to reionization [18].

Since there is a large variation in the ionization fraction at later times, assumptions made about the effective efficiencies weaken. In order to observe possible errors introduced due to this large deviation, an ionization history developed using the "SSCK" prescription [16, 22] and the same cosmological parameters is also given in Figure 2.5. While there is an even larger variation at late times, up to two orders of magnitude, x_e and $T_{\rm IGM}$ are still far below the observational constraints. Additionally, they have only minor variation relative to the standard during the period of interest at high redshift.

2.3 Cosmic Microwave Background

The cosmic microwave background (CMB) is an image of the background radiation spectrum from the time of recombination $z \sim 1100$. It formed as the photon background decoupled from matter due to ions condensing to form neutral atoms. While it

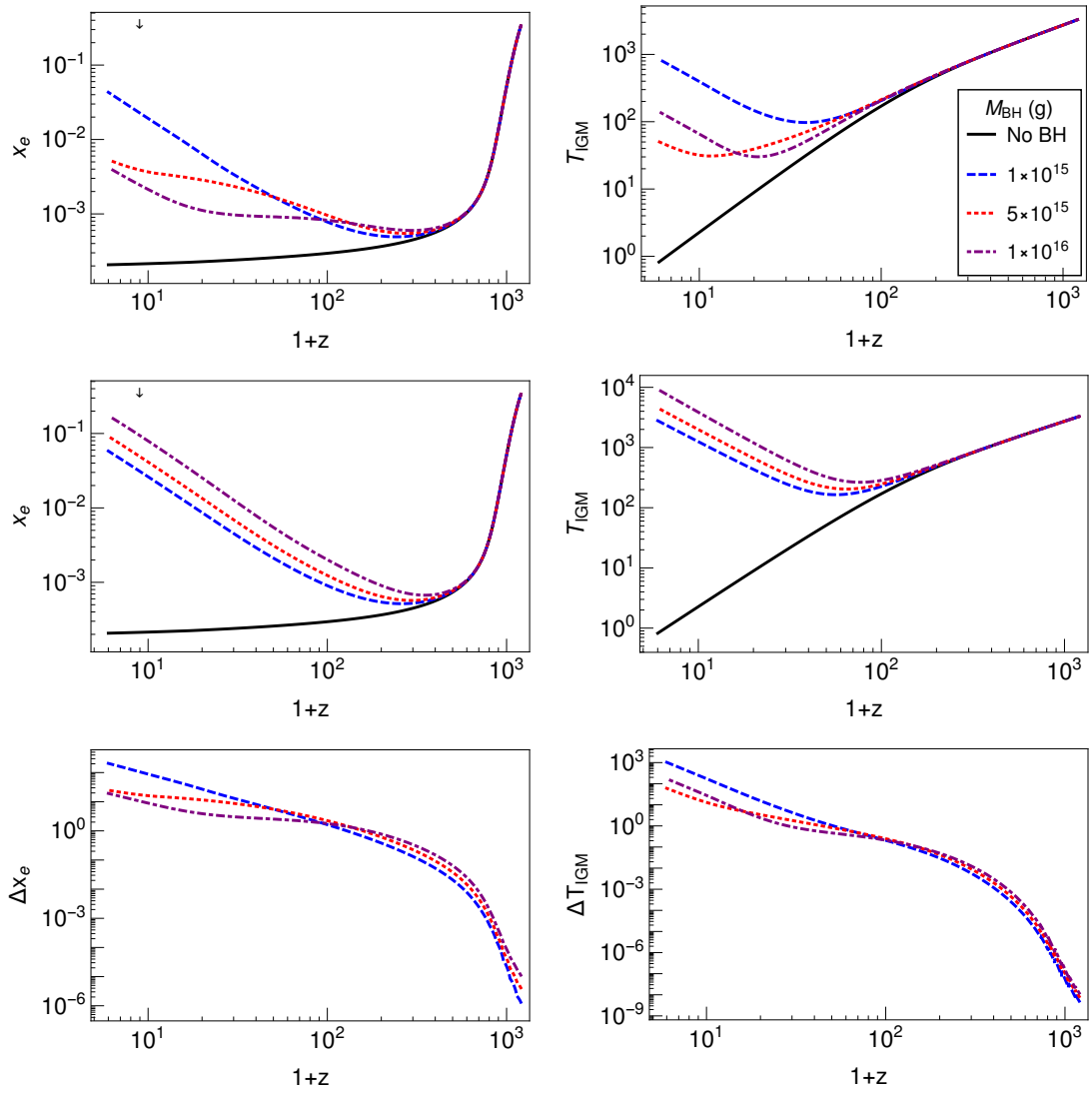

Figure 2.5: Comparison of x_e and $T_{\rm IGM}$ evolution for different models. Ionization fraction (left) and temperature of the IGM (right) due to PBH energy injection using effective efficiencies (top), using the "SSCK" prescription (middle), and percent change from the no PBH case (bottom). Bounds on the parameters are also plotted. The PBH density $\Omega_{\rm BH}$ for each mass is taken to be at the 95% confidence limit discussed in this work for *Planck* constraints. The legend applies to all graphs. Reprinted with permission from Ref. [23].

is very uniform, small spatial features do exist and correspond to thermal equilibrium distances. Injections from particle interactions discussed in Sec. 2 help to disguise these variations by allowing pockets to be stronger coupled. Figure. 2.6 shows how injections can alter correlations between different regions. The main properties used are the CMB anisotropy power spectra correlations Temperature-Temperature(TT), Temperature-(E-mode) (TE), and (E-mode)-(E-mode) (EE). E-mode is the electric polarization of the photon background. For this figure, the injections are assumed to be provided by PBHs where their abundance includes all the dark matter content. Note that smaller PBHs inject more energy. This increased energy injection scales as the inverse cubic of the mass.

The energy injection results in a scale-dependent deviation from the standard case; there is an increase in the power spectrum at small multipoles and a decrease at large multipoles (large multipoles correspond to small angular separations). This behavior occurs because the energy injection increases the width of the last scattering surface. Perturbations on scales smaller than this width are suppressed as photons are able to be correlated at larger distances, as can be most easily seen for TT correlations. In addition, the TE and EE spectra peaks shift with increasing injections. These shifts are due to increased contributions by monopole perturbations which trace to polarization and are introduced with the increase to the scattering surface [9].

To place constraints on model properties from CMB, we fit the simulated spectra to *Planck* half mission data [32]. The likelihood used was TT,TE,EE+lowP, a combination of TT, TE, and EE correlations as well as B-mode correlations for $l \leq 29$. Figure 2.7 shows the posterior probability densities for a few example cosmological parameters, both with and without PBHs. The distributions are consistent with each other, up to minor shifts well within experimental uncertainties. Allowing us to fix them for ease of calculation without introducing large systematic uncertainties due to correlations between parameters. Note that this has been highlighted in previous studies of the

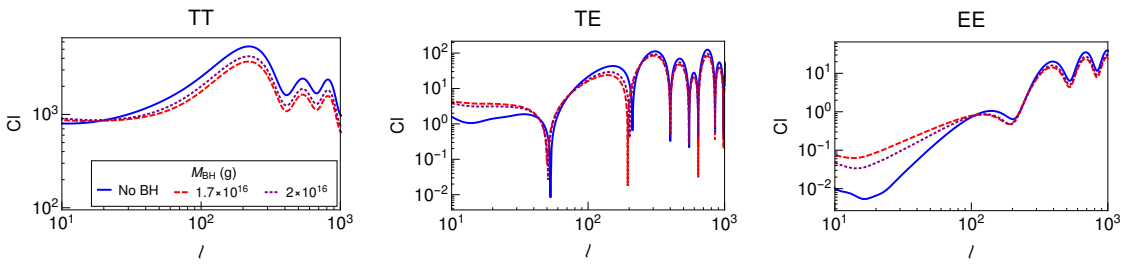

Figure 2.6: Alterations to the CMB power spectrum from energy injections. CMB correlations TT (left), TE (middle), and EE (right) for various PBH masses. Effects from annihilation and decay have similar effects. Reprinted with permission from Ref. [23].

impact of dark matter annihilation and decay on the CMB [33].

For calculating the constraints, we use the CMB theoretical modeling software CAMB [34, 35] and a modified version of HyRec [17]. Again, the *Planck* data likelihood set used was *Planck* TT,TE,EE+lowP [1]. Fitting parameters were performed for a single mass with CosmoMC [36, 37] using all *Planck* polarization amplitudes [1] in addition to parameters specific to each model. Since there is little variation in the base cosmological parameters, for computational convenience, we take the six principal cosmological parameters to be fixed to their best fit values in the case of no additional energy injection [1] unless otherwise stated. The six principal cosmological parameters are: the physical baryon density, $\Omega_b h^2 = 0.022252$; the physical CDM matter density, $\Omega_c h^2 = 0.11987$; the CMB acoustic scale parameter, $100\theta_{MC} = 1.040778$; the reionization optical depth, $\tau = 0.0789$; primordial curvature perturbations, $\ln(10^{10} A_s) = 3.0929$; and the scalar spectral index, $n_s = 0.96475$ [1, 38]. The confidence limit is defined as the cumulative distribution centered around the median, which corresponds closely to the peak of the distributions in Figure 2.7.

We note that since the six base cosmological parameters were fixed, the parameters may be more strongly constrained than in a fit with more parameter freedom. Systematics induced by parameter fixing were checked by performing a fit with all of the

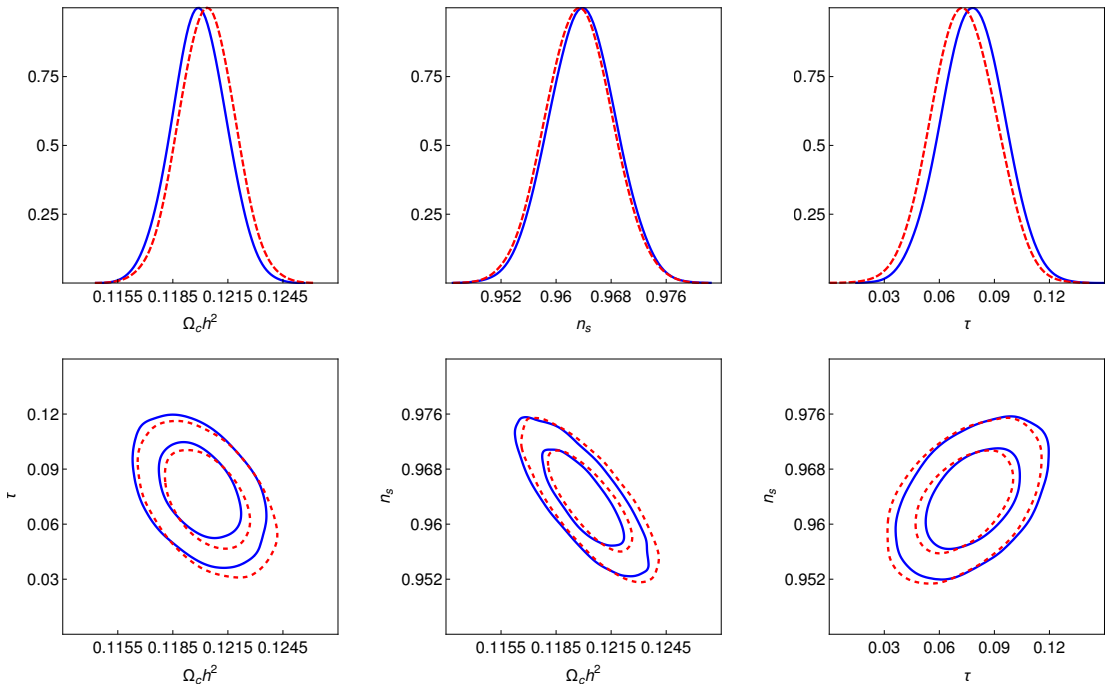

Figure 2.7: Change in the posterior probability distributions for a few principal cosmological parameters for injections from PBHs of mass $2 \times 10^{16} g$. Single variable distributions (top) with most probable values normalized to one, where blue (solid) lines represent no PBH case while red (dashed) includes PBHs. Correlations between different parameters (bottom) with inner and outer curves correspond to 68% and 95% confidence levels respectfully. Reprinted with permission from Ref. [23].

base cosmological parameters free to vary for a single PBH mass of 2×10^{16} g. The constraint on $\Omega_{\rm BH}$ weakened by up to a factor of three.

2.4 21 cm Absorption Line

The measurement of the 21 cm line is a target of several current and future observations, and is projected to provide a wealth of new cosmological data that will shed light on the so-called "Dark Ages" of cosmology prior to star formation. (For reviews see, Ref. [39, 40])

Recently the Experiment to Detect the Global Epoch of Reionization Signature (EDGES) reported the observation of 21 centimeter absorption lines at high redshift $z = 15 - 20$, with an absorption signature of $T_{21} = -500^{+200}_{-500}$ mK (99% C.L.) at a redshift of $z \approx 17.2$ with a central value of 78 MHz. It had a best-fit neutral hydrogen spin temperature $T_{\rm S}$ much lower than conventional astrophysical expectations, leading to strong absorption signals [2]. If confirmed, the abrupt lowering of $T_{\rm S}$ relative to the cosmic microwave background temperature $T_{\rm CMB}$ near $z \sim 20$ has been interpreted [2, 3] as due to the re-coupling of $T_{\rm S}$ to the hydrogen gas temperature $T_{\rm G}$ by the Wouthuysen-Field effect [41, 42], where a lower-than-standard hydrogen gas temperature has been proposed that may arise from cooling effects [3] via interactions with hypothetical particles. This result can be interpreted as demonstrating a stronger absorption signal than standard astrophysical expectations, and has sparked a flurry of studies in the dark matter literature, including implications for dark matter-baryon couplings [43–51], dark matter annihilation [52–55], decaying dark matter [55–57], primordial black holes [56, 58], fuzzy dark matter [59], dark sectors [60–63], and non-cold dark matter models including warm dark matter and axions [64–69].

From another perspective, the observation of 21 cm signals also places a bound [52] on hypothetical processes that are capable of heating up the intergalactic medium (IGM) prior to the reionization time, e.g., by the energy injection from the annihilation of dark matter [70–72].

Beside mapping the Universe's mass distribution at high redshift, the 21 cm absorption line(s) measurement is also a potent probe of the temperature evolution in the CMB and the intergalactic medium. Before the light from the first stars ionized the intergalactic gas, the neutral hydrogen resonantly absorbs the 1.42 GHz radiation line as the CMB passed through. This 1.42 GHz or 21 cm wavelength spectral line corresponds to the hyperfine energy split between aligning and anti-aligning the spin of the electron and that of the nucleus in the ground state of the neutral hydrogen, which form a spin-0 singlet and a spin-1 triplet. The population ratio between the triplet and singlet states is described by the spin temperature as $N_1/N_0 = 3\,\mathrm{e}^{-0.068\mathrm{K}/T_\mathrm{S}}$, where 0.068 K is the equivalent temperature of the 21.1 cm wavelength corresponding to the hyperfine energy splitting $\Delta E = 5.9 \times 10^{-6}\,\mathrm{eV}$.. The 21 cm absorption intensity from the radiation background, i.e. the CMB, is given by the brightness temperature [73],

$$T_{21} \approx 0.023\mathrm{K} \cdot x_{\mathrm{H_I}}(z) \left(\frac{0.15}{\Omega_\mathrm{m}} \cdot \frac{1+z}{10}\right)^{\frac{1}{2}} \frac{\Omega_\mathrm{b} h}{0.02} \left(1 - \frac{T_\mathrm{CMB}}{T_\mathrm{S}}\right), \tag{2.11}$$

where $x_{\mathrm{H_I}}$ is the neutral ($\mathrm{H_I}$) fraction of the intergalactic hydrogen gas. For redshift $z \geq 20$ prior to reionization time, $x_{\mathrm{H_I}} \simeq 1$ in standard astrophysics. Ω_m and Ω_b are the total matter and baryon fractions of the critical energy density of the Universe, and h is the Hubble constant in the unit of 100 km $\mathrm{s}^{-1}\mathrm{Mpc}^{-1}$. The latest precision measurements of these cosmological parameters are given by the *Planck* experiment [1]. With the presence of neutral hydrogen $x_{\mathrm{H_I}} > 0$ and a colder spin temperature than the radiation background, $T_\mathrm{S} < T_\mathrm{CMB}$, the absorption feature in the CMB will emerge with $T_{21} < 0$.

Hydrogen atoms decouple from the CMB at $z \sim 200$. The background radiation temperature scales with redshift as $T_\mathrm{CMB} = 2.7\mathrm{K} \cdot (1+z)$, while the matter temperature scales as $(1+z)^2$ and cools faster than the CMB after decoupling. Hence, for hydrogen gas, its T_S and T_G drop below T_CMB during the cosmic "dark age", as observed in

Figure 2.8. The CMB photons can still flip the H_I hyperfine states and bring T_S into equilibrium with T_{CMB}. In this period, we typically expect $T_G < T_S < T_{CMB}$, with T_S approaching T_{CMB} as interactions with CMB photons flip the hyperfine state and draw the spin temperature towards the CMB temperature. Entering the reionization epoch, the Lyman-α emissions from stars recouple T_S to T_G through the Wouthuysen-Field effect [41, 42, 74, 75], and T_S demonstrates a rapid drop to the colder T_G. This leads to a drop in T_{21} and the expectation for a 21 cm absorption signal.

EDGES measured a rapid lowering of T_S at $z \simeq 21$, that would require $T_S \simeq T_{CMB}$ to be reached before $z \simeq 21$, and T_S quickly re-couples to T_G by $z \sim 17-18$ [2]. While the 21 cm absorption signal prior to $z \sim 14$ is consistent with the cosmic reionization picture [76], the maximal signal strength $T_{21} = -500$ mK [2] at $z = 15-20$ is more than twice compared to the expectation from standard astrophysics. The central redshift of the T_{21} trough is earlier than expected and indicates for an enhanced star formation rate in galaxies [77]. The flat shape of $T_{21}(z)$ in this redshift range is also unaccounted for in a standard evolution process [2]. Ref. [3] reported this low T_{21} result as a 3.8σ-strong absorption excess, and that the widened gap between T_S from T_{CMB} may rise from new physics.

However, the foreground contamination for radio astronomy observations is at least four orders of magnitude higher than the 21 cm brightness temperature. This makes it extremely tricky to remove and measure the underlying signal. In Ref. [2], the EDGES group used the polynomial foreground model to fit the galactic synchrotron and atmospheric signal in frequency space and remove it. But there could be some low-level foreground or systematics in the system that can potentially bias the results. The EDGES data can be tested and verified by future 21 cm experiments like PRIZM [78], HERA [79], LEDA [80], and SKA [81]. Here, we adopt a similar approach as in Ref. [52], that such detection of strong 21 cm absorption by EDGES would constrain the amount of accumulated high-energy particle injection that could have heated up

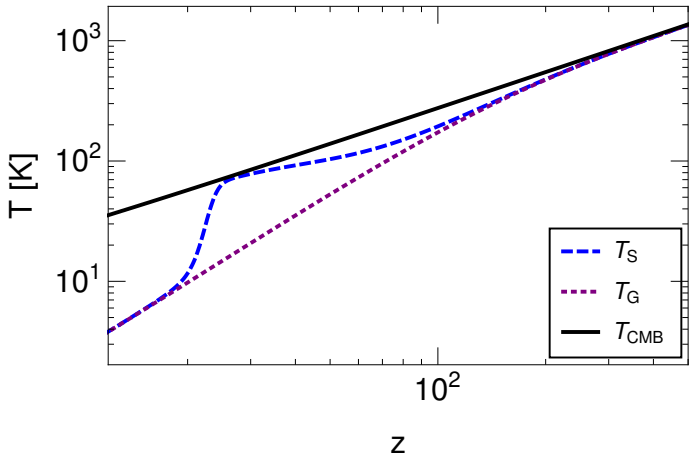

Figure 2.8: T_G, T_S, and T_{CMB} evolution in standard astrophysics. T_S approaches T_{CMB} after the $z \sim 200$ decoupling, suppressing the 21 cm absorption until T_S recouples to T_G after the formation of the earliest stars. Reprinted with permission from Ref. [56].

T_G by the reionization epoch, which would narrow down the difference between T_S and T_{CMB} for $z = 15 - 20$ and cause significant reduction in the 21 cm absorption signal.

Dark matter interactions can be a steady source of Standard Model particles as discussed in Sec. 2. The photons and electrons, injected at high energy and can typically reach up to $O(10^{-1})M_{DM}$, gradually lose energy by interacting [14, 18, 19] with the intergalactic medium via ionization, Lyman-α excitations, gas temperature heating, as well as scattering off the background continuum photons that is studied in Ref. [53] as another explanation of the EDGES data with a heated photon radiation background. For 21 cm measurements, both the corrections to x_e and T_G can affect T_{21}, especially at a time when T_S re-couples to T_G. A reasonable choice to consider is at the central redshift $z \simeq 17$ where EDGES detected absorption signals. Constraints can be placed by requiring the heating from new physics raises the radiation temperature by ΔT_{21} no more than 100 or 150 mK, this limit corresponds to a less than half or 3/4 suppression of the standard astrophysical $T_{21} = -200$ mK absorption strength. In standard astrophysics this temperature rise can wipe out or greatly suppress the 21 cm absorption

signal. It is also larger than EDGES's T_{21} 1σ up-fluctuation uncertainty (+200 mK by 99% credence level [2]).

The $\Delta T_{21} = +100$ or +150 mK limits are based on the temperature evolution by standard astrophysical processes, and should be considered as proof-of-principle estimates for new physics' heating effect on the IGM in light of a 21 cm signal discovery. As EDGES measures a stronger 21 cm signal than that from standard astrophysics, if hypothetic gas cooling also exists, it could partially negate the effect of heating processes, and the same ΔT_{21} would require a larger energy injection rate. In case of dark matter, gas cooling demands a prohibitive DM-baryon scattering cross-section [44, 45] with a limited dark matter mass range. Under the minimal coupling assumptions, a 10^{24-26}s decay lifetime is usually mediated by effective interactions that are too weak to facilitate sufficient DM-baryon scattering, thus additional DM-SM coupling structures would become necessary to make dark matter's cooling effect significant, which introduces more modeling assumptions on dark matter. Also, the potentially large uncertainty in the low frequency range of the cosmic radiation field [61, 82, 83] can lead to significant correction to the 21 cm absorption rate, which would also affect the required amount of energy injection heating accordingly. Alternative new physics mechanisms, and radiation field background assessment can be probed or improved from future experiments.

We use the numerical package HyRec [17] to compute the temperature evolutions, with the energy injection corrections implemented into the evolution equations. The Wouthuysen-Field effect is included into the calculation by defining [73]

$$T_{\rm S} = \frac{T_{\rm CMB} + y_{\rm c} T_{\rm G} + y_{\rm Ly\alpha} T_{\rm Ly\alpha}}{1 + y_{\rm c} + y_{\rm Ly\alpha}}, \tag{2.12}$$

$$y_{\rm c} = \frac{C_{10}}{A_{10}} \frac{T_\star}{T_{\rm G}}, \tag{2.13}$$

$$y_{\rm Ly\alpha} = \frac{P_{10}}{A_{10}} \frac{T_\star}{T_{\rm Ly\alpha}}, \tag{2.14}$$

where $A_{10} = 2.85 \times 10^{-15} s^{-1}$ is transition's spontaneous emission coefficient, C_{10} is the collisional de-excitation rate of the triplet hyperfine level, $P_{10} \approx 1.3 \times 10^{-12} S_\alpha J_{-21} s^{-1}$ is the indirect de-excitation rate due to Lyman-α absorption, $T_\star = h\nu_0/k_{\rm B} = 0.068$ K is the Lyman-α energy, $T_{\rm G}$ is the hydrogen gas temperature and is the same as $T_{\rm IGM}$ from Sec. 2, $T_{\rm Ly\alpha}$ is the Lyman-α background temperature, and $T_{\rm Ly\alpha} = T_{\rm G}$ for the period of interest, S_α is a factor of order unity that incorporates spectral distortions [74], and J_{-21} is the Lyman-α background intensity written in units of 10^{-21} erg cm^{-2} s^{-1} Hz^{-1} sr^{-1} and is estimated by an average of the early and late reionization results of Ref. [84].

This work does not aim at a rigorous analysis of astrophyiscal reionization models. Instead, we assume $T_{\rm S}$ reaches the strong coupling limit, with $J_{-21} \gg 1$ [73] during EDGES' signal creation at the early redshift range $17 < z < 20$ of the reionization era. We model J_{-21} by taking the average of the two scenarios in Ref. [84], and this assumption will qualify as a conservative constraint on the heating from new physics energy injections: Our choice J_{-21} suffices for the strong coupling limit. As long as the strong coupling limit is satisfied, the $T_{\rm S}$ result and its associated new-physics constraint remains unchanged for different values of J_{-21}. In the case of a much lower J_{-21} away from the strong coupling limit, the coupling between $T_{\rm S}$ and $T_{\rm G}$ is weaker, less new-physics heating is required, and the bound strengthens.

It is also noted that we do not include the X-ray heating effects for the depth of T_{21} signal at $z \sim 17$, which would become dominant at later redshift and closes the T_{21} trough near full ionization, which EDGES measurement indicates to happen at $z = 14$. In this analysis we focus on the maximal T_{21} strength that depends on the gas temperature at the beginning of the reionization era, and our bounds without X-ray effects is conservative as additional astrophysical heating reduces the 21 cm signal. To fully describe the T_{21} features form the EDGES data, a detailed model that incorporates astrophysical heating would be needed.

Also note, that by the measurement's definition, deviations of $T_{\rm IGM}$ must be much larger in the late Universe compared to restrictions we required in Sec. 2.2 around the time of recombination. While this introduces an error to the effective efficiencies, the amount of deviation is minimal and incorporating the effect would lead to stronger bounds due to the increased coupling of the ionized gas to the photon background.

We use the cosmological parameters $\Omega_{\rm m} = 0.3$, $\Omega_{\rm b} = 0.04$, $\Omega_\Lambda = 0.7$, and $h = 0.7$ for 21 cm calculations throughout this work unless stated otherwise. Figure 2.9 illustrates the heating effect on $T_{\rm G}$ and T_{21} from dark matter decay, assuming contribution from 100% of the relic density and the DM$\rightarrow e^+e^-$ channel. Also shown are the same results for PBHs. Heating of neutral hydrogen becomes manifest at near-reionization time. Note that variations in cosmological parameters do slightly affect the result. Cosmological parameter variation within *Planck*'s constraint is expected to lead to $\mathcal{O}(1)$ correction. As an example, for the best fit of *Planck*'s TT,TE,EE+lowP data, $\Omega_{\rm m} = 0.316$, $\Omega_{\rm b} = 0.049$, $\Omega_\Lambda = 0.684$, and $h = 0.67$ [1], the 21 cm constraints shown in Sec. 4 weaken by a factor of 1.6. Tested specifically for PBH and decaying models. Constraints utilizing the 21 cm estimates were made by requiring the T_{21} correction to its standard astrophysical value at $z \simeq 17$ to be less than 100 and 150 mK, namely $T_{21}(z = 17) < -100$ and -50 mK respectively.

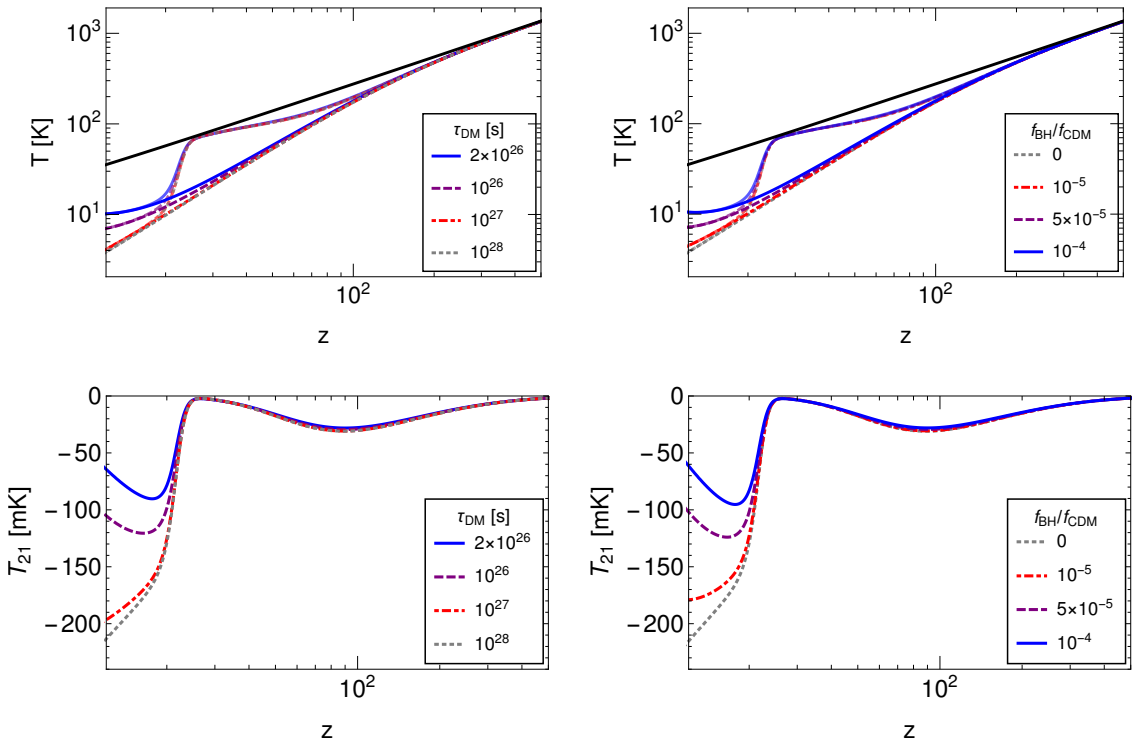

Figure 2.9: Effect of energy injections on 21 cm parameters. Dark matter decay (left) and primordial black hole evaporation (right) lead to higher $T_{\rm G}$ (top) and T_{21} (bottom) in the reionization epoch. Here dark matter mass is 100 GeV and decays into an e^+e^- final state. The black hole mass is 10^{16} g. For convenience, $T_{\rm CMB}$ (black) and $T_{\rm S}$ (faded) are also shown in the $T_{\rm G}$ graphs. Reprinted with permission from Ref. [56].

3. INTERACTION SPECTRA DETECTION*

During a dark matter interaction, particle spectra are produced. In Sec. 2, we looked at the effects that these particles have on the IGM and proceeded to investigate methods by which to constrain dark matter by its influence on the evolution of the Universe. An alternative method is to observe dark matter spectra directly. Galaxies form dense regions of dark matter. These locations can be treated as sources for different scenarios. The measured particle flux from these sources can be compared with predicted spectra to place bounds on the associated model. The spectra for a particular model is calculated in the exact same way as for effective efficiency calculations, see Sec. 2.1. The initial products from the interaction are produced. These particles propagate through their decay chains until they reach a stable form. In some cases, the spectra should be further altered to account for interaction the particles experience as they transverse from creation to observation at Earth, such as passing through galactic dust.

The particle flux predicted by a dark matter interaction originating from an object is characterized by [8]

$$\Phi_{\rm dec} = \frac{1}{4\pi}\frac{1}{m_\chi \tau_\chi}\int_{E_{\rm min}}^{E_{\rm max}} \frac{{\rm d}N}{{\rm d}E}{\rm d}E J_{\rm dec}, \tag{3.1}$$

$$\Phi_{\rm ann} = \frac{1}{4\pi}\frac{\langle\sigma v\rangle_\chi}{2m_\chi^2}\int_{E_{\rm min}}^{E_{\rm max}} \frac{{\rm d}N}{{\rm d}E}{\rm d}E J_{\rm ann}, \tag{3.2}$$

where m_χ is the dark matter mass, τ_χ is the dark matter lifetime, and $\langle\sigma v\rangle_\chi$ is the dark

*Parts of this section are reprinted with permission from:

S. J. Clark, B. Dutta, and L. E. Strigari, "Dark Matter Annihilation into Four-Body Final States and Implications for the AMS Antiproton Excess," *Phys. Rev.* **D97** no. 2, (2018) 023003, arXiv:1709.07410 [astro-ph.HE]. © 2018 American Physical Society

S. J. Clark, J. B. Dent, B. Dutta, and L. E. Strigari, "Indirect detection of the partial p wave via the s wave in the annihilation cross section of dark matter," *Phys. Rev.* **D99** no. 8, (2019) 083003, arXiv:1901.01454 [hep-ph]. Published by the American Physical Society.

matter thermally averaged cross-section. $E_{\rm min}$ and $E_{\rm max}$ form the range of measured energies. $J_{\rm dec}$ and $J_{\rm ann}$ are the J-factors for decay and annihilation. The J-factors contain all of the astrological information of the interaction, while the rest of the equations describe the particle physics interaction. The J-factors for the two cases are

$$J_{\rm dec} = \int_{\Delta\Omega} {\rm d}\Omega \int_{\rm l.o.s.} \rho_\chi(\mathbf{r}) {\rm d}s, \tag{3.3}$$

$$J_{\rm ann} = \int_{\Delta\Omega} {\rm d}\Omega \int_{\rm l.o.s.} \rho^2_\chi(\mathbf{r}) {\rm d}s, \tag{3.4}$$

where they are integrated over the line of sight from the source to the observer and all observed angles. ρ_χ is the dark matter distribution function. As will be seen, primordial black holes can be treated identically as decaying dark matter models for this purpose.

The two main locations considered for a signal in this manner are the galactic center (GC) and dwarf spherical galaxies (dSph). The GC has the benefit of producing a large flux due to the high dark matter density. However, it suffers from large uncertainties. On the other hand, dSph have low uncertainties and produce very clean signals; however, they suffer from a lack of signal. In the following subsections, we will look at the general approaches used to constrain dark matter characteristics through spectra observations.

3.1 Galactic and Galactic Center Analysis

We begin discussing the constraints from diffuse gamma-ray data. As a note, in Sec. 4.3, we perform an analysis that incorporates estimates on the same data. This was an early work, and the approach is outlined in the section. It is similar to the antiproton comparison outlined in Sec. 3.3. Our data selection and analysis method generally follow that of Refs. [85, 86]; we will note the particular aspects in which they differ. We use Fermi Science Tools version v11r5p3[1], and select Pass 8 SOURCE-class

[1] `https://fermi.gsfc.nasa.gov/ssc/data/analysis/software/`

events for mission elapsed time 239557417 s to 554861541 s. We apply the recommended `(DATA_QUAL>0)&&(LAT_CONFIG==1)` filter to ensure quality data and a zenith cut $z_{max} = 100^\circ$ to filter background gamma-ray contamination from the Earth's limb.

For our Region-of-Interest (ROI), we take the R90 region as defined in Ref. [86], corresponding to a cut on the photon direction 90° from the galactic center. This amounts to taking data from half of the sky, with the regions in the galactic plane, corresponding to longitudes $> 6^\circ$ and galactic latitudes $> 5^\circ$, masked out. In this region, we take the dark matter density profile to be isothermal, $\rho(r) = \rho_0/[1+(r/r_s)^2]$, where $r_s = 5$ kpc, and ρ_0 is normalized so that the dark matter density at the location of Sun is $\rho\,(r_\odot = 8.5 \text{ kpc}) = 0.4$ GeV cm^{-3}. This density profile was chosen because it provides the least stringent constraints on the models that we consider. We have verified this by examining the impact of alternative distributions, in particular NFWc from Ref. [86]. For the NFWc profile constraints, we use photons within only a 3° angle from the galactic center. NFWc is an adiabatically contracted NFW dark matter profile, $\rho(r) = \rho_0/[(r/r_s)^\gamma(1 + r/r_s)^{3-\gamma}]$, where $r_s = 20$kpc and $\gamma = 1.3$.

To produce constraints for a given dark matter mass, $m_{\rm DM}$, we consider photons emitted from models that contain a line like feature within the energy range $0.4m_{\rm DM} < E_\gamma < 2.25m_{\rm DM}$. This peak will typically be from a bremsstrahlung gamma-ray emission in our analysis, but it can be applied to any such line-like feature. The lower bound is set in order to contain photons from the peak of a bremsstrahlung emission of the spectrum. The maximum energy was chosen so as to include a large sample of background photons, to ensure that the background is well fit by a power law. We have verified that for our entire mass range, we are in the regime in which our uncertainties are dominated by statistics rather than systematics, so that the power law fit for the background is a good description of the data. Within this energy range we perform a binned likelihood analysis, with photons in equally spaced logarithmic bins, with 50 bins per decade. We determine the best fit power law index for the background, and

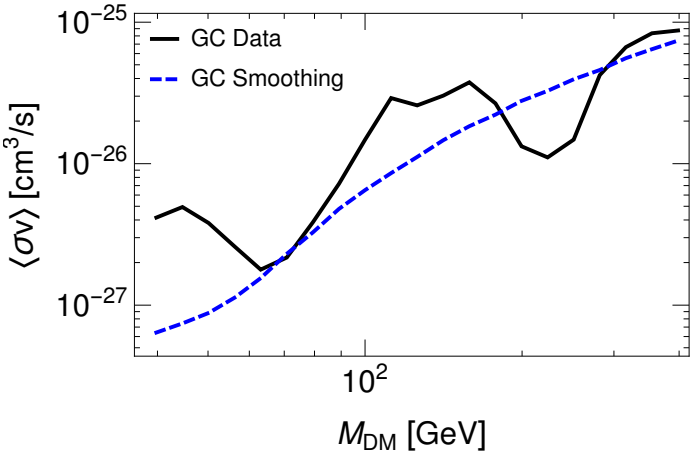

Figure 3.1: Comparison between different galactic center fitting techniques. The averaging routine (dashed) is approximately the median of the result directly obtained from the galactic center data (solid). The fitted spectrum is produced from annihilation to electrons plus a boson with a mediator mass ratio 1.1. Reprinted with permission from Ref. [87].

then generate a new set of pseudo-data from this fit. We fit this pseudo-data to a background plus the desired model. For a given model, we define the limits as where the TS statistic for the log-likelihood exceeds TS > 1.355.

In Figure 3.1, we demonstrate differences that arise between our smoothing algorithm and our analysis that calculates the galactic center constraints straight from the Fermi data. Our smoothing approach fits the data to a power law and then performs the least likelihood analysis off the fit. This approach helps remove statistical fluctuations present in the data. However, we lose the capacity to identify a positive source signal. Comparing the two, the smoothed result is approximately the median of the baseline calculation.

3.2 Dwarf Spheroidals

Constraints using dwarf spheroidal galaxies (dSph) were performed through use of the pre-generated likelihood functions provided in Ref. [88]. The photon flux observed

at Earth is calculated by

$$\Phi = \frac{1}{8\pi} \frac{\langle \sigma v \rangle}{m_{\rm DM}^2} \times J, \tag{3.5}$$

where J is the J-factor, which incorporates the dark matter distribution within the dSph as well as its distance from the observer. For our analysis we adopt the J-factor values used in Ref. [8]. A log-likelihood analysis is performed on the combined system of all the dSphs to obtain the null likelihood probability for the stacked flux [8].

The pre-generated likelihood functions used were evaluated with the assumption of a continuum signal. As such, they are not effective at performing the line searches discussed in Sec. 3.1. However, they are ideal for identifying continuum signals. These types of signals are frequently present in hadronizing decay chains. The bremsstrahlung model mentioned before produces large numbers of W/Z bosons making this an ideal search method.

3.3 Antiproton Excess

AMS [89] has recently published a measurement of the anti-proton spectrum, hinting at a possible excess relative to those expected from astrophysical sources. This measurement is also of interest because, unlike the gamma-ray [90] and positron excess [91], it is unlikely that these results can be explained by unresolved sources such as pulsars that contribute to diffuse radiation. This measurement may be important for dark matter, because antiprotons are a major constituent of some dark matter annihilation spectra.

Several authors have considered antiproton production from annihilating dark matter in light of the AMS data, and have found preferred models, such as $\chi\chi \to b\bar{b}$ [92]. We utilize these results to extend the constraints of one of our models, annihilation to a four-body final state model, but they can also be performed for other scenarios. We make the comparison by using the spectrum outputs by PYTHIA discussed pre-

viously as an additional source term in GALPROP[2] [93]. This provides us with the antiproton spectra measured on Earth as a result of dark matter annihilation in the galaxy. For GALPROP, we use parameters that are similar to those in Ref. [92], specifically an NFW dark matter density profile with a characteristic halo radius of 20 kpc and a fixed characteristic density of 0.43 GeV/cm^3 at radius 8.5 kpc.

Antiproton spectra between the two- and four-body cases are very similar. The most pertinent degree of freedom for comparison is the mediator mass. Figure 3.2 shows the annihilation antiproton flux spectra after propagation through the galaxy. The shape of the spectra is mostly unaltered when comparing to the injection spectrum before propagation. Photon spectra for the same cases is also shown highlighting a key difference between the antiproton and the photon spectra for different mediator masses. While different mediator masses result in minimal variation in the photon spectrum, there is a significant difference in the antiproton spectrum, allowing antiprotons to be used as a probe of mediator properties. These differences arise from the kinematics and decay properties of the mediator daughter particles.

These post-propagation spectra are used to estimate four-body antiproton excess constraints by association with the constraints calculated in Ref. [92]. The comparison between the two- and four-body constraints is made by matching dark matter masses between the two models with the same spectral midpoint, defined as the energy where half of the antiprotons have greater energy. The cross-section comparison is performed through

$$\langle \sigma v \rangle_4 = \langle \sigma v \rangle_2 \times \int_{E_{min}}^{E_{max}} \frac{\mathrm{d}\Phi_2}{\mathrm{d}E_{\bar{p}}} \mathrm{d}E_{\bar{p}} \times \left(\int \frac{\mathrm{d}\Phi_4}{\mathrm{d}E_{\bar{p}}} \mathrm{d}E_{\bar{p}} \right)^{-1}, \tag{3.6}$$

where $\langle \sigma v \rangle_i$ is the thermally averaged cross-section. $\mathrm{d}\Phi_i/\mathrm{d}E_{\bar{p}}$ is the post-propagation antiproton flux at Earth for a reference cross-section of $2 \times 10^{-}26\mathrm{cm}^3/\mathrm{s}$. $E_{\bar{p}}$ is the antiproton energy. E_{min} and E_{max} are the minimum and maximum energy of the experiment. For AMS antiprotons, this energy is $\sim$ 430 MeV to 1.8 TeV. Note that

[2] `https://galprop.stanford.edu`

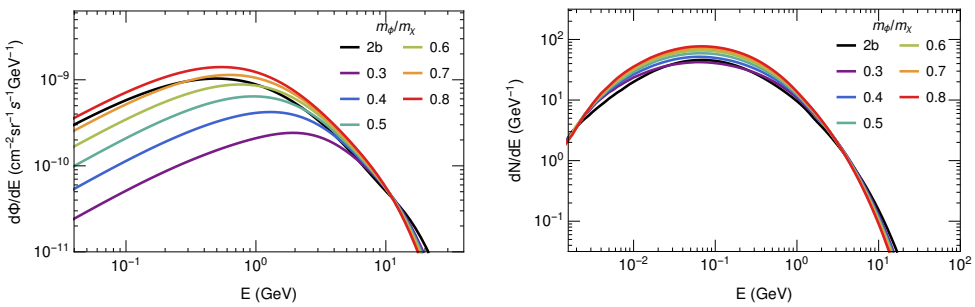

Figure 3.2: Antiproton and gamma-ray spectra for $4b$ final state interactions. The dark matter mass is 100 GeV. Antiproton flux (left) spectra observed at Earth from galactic annihilations, where E is the antiproton's kinetic energy. Gamma-ray spectra (right) from a single annihilation. Note that the shape of the antiproton spectra before and after propagation is nearly identical. Around $m_\phi/m_\chi = 0.7$ the $2b$ and $4b$ spectra are nearly identical. There is little variation in the photon spectra for different mediator masses above Fermi-LAT's sensitivity. For AMS, there are significant differences above the minimum sensitivity. Reprinted with permission from Ref. [28].

$\mathrm{d}\Phi_i/\mathrm{d}E_{\bar{p}}$ is dependent on the inverse square of the dark matter mass in addition to the annihilation spectra. The index i differentiates between two- and four-body terms where the spectral midpoints are equal. This method was chosen due to the correlation between mass, peaks, and widths. With increasing dark matter mass, the spectral width increases while peak remains nearly constant.

4. RESULTS*

In this section, we discuss the motivation for the models investigated and present constraints imposed by the procedures outlined in Sec. 2 and Sec. 3. The models are decaying dark matter (Sec. 4.1), primordial black holes (Sec. 4.2), dark matter annihilations into four-body final states (Sec. 4.3), and dark matter annihilation through a bremsstrahlung gauge boson (Sec. 4.4).

4.1 Decay

In order for a decaying dark matter candidate to survive to today, it must be incredibly stable. However, its influence can still be felt. One such way is by injecting energy that can be observed by 21 cm absorption detection experiments [72, 94–99].

The decay of dark matter is insensitive to small-scale matter density distributions and gives a steady energy injection rate,

$$\frac{\mathrm{d}E}{\mathrm{d}V\mathrm{d}t} = \Gamma_{\mathrm{DM}} \cdot \rho_{\mathrm{c},0}\Omega_{\mathrm{DM}}(1+z)^3, \tag{4.1}$$

where Γ_{DM} is the dark matter decay width, $\rho_{\mathrm{c},0}$ is the current critical density of the Universe. In comparison to the $(1+z)^6$ redshift dependence in dark matter annihilation, the injection rate from dark matter decay drops much slower and can be more significant

*Parts of this section are reprinted with permission from:

S. Clark, B. Dutta, Y. Gao, L. E. Strigari, and S. Watson, "Planck Constraint on Relic Primordial Black Holes," *Phys. Rev.* **D95** no. 8, (2017) 083006, arXiv:1612.07738 [astro-ph.CO]. © 2017 American Physical Society

S. J. Clark, B. Dutta, and L. E. Strigari, "Dark Matter Annihilation into Four-Body Final States and Implications for the AMS Antiproton Excess," *Phys. Rev.* **D97** no. 2, (2018) 023003, arXiv:1709.07410 [astro-ph.HE]. © 2018 American Physical Society

S. Clark, B. Dutta, Y. Gao, Y.-Z. Ma, and L. E. Strigari, "21 cm limits on decaying dark matter and primordial black holes," *Phys. Rev.* **D98** no. 4, (2018) 043006, arXiv:1803.09390 [astro-ph.HE]. © 2018 American Physical Society

S. J. Clark, J. B. Dent, B. Dutta, and L. E. Strigari, "Indirect detection of the partial p wave via the s wave in the annihilation cross section of dark matter," *Phys. Rev.* **D99** no. 8, (2019) 083003, arXiv:1901.01454 [hep-ph]. Published by the American Physical Society.

at lower z. For this work, we restrict ourselves to a minimal dark matter decay scenario for a generic lifetime constraint.

4.1.1 Decay Constraints

For decaying dark matter, we investigated the 21 cm constraints and compared them with existing bounds. Figure 4.1 illustrates the constraint on the decay lifetime $\tau_{\rm DM}$ for dark matter masses from MeV up to 100 TeV. The constraint assumes generic two-body decay channels. The DM$\rightarrow e^+e^-$ channel is the most stringently constrained due to its high fraction of electrons in the final state. $\mu^+\mu^-$ and $b\bar{b}$ final states are also plotted, which have lower $f(E,z)$ in comparison. $\mu^+\mu^-, b\bar{b}$ are also much smoother than e^+e^- due to the wide spectra of stable final particles which results in most of the features of the electron and photon effective efficiencies averaging out. As lower energy injection requires less time to deposit its energy into the intergalactic medium, f increases with lower $M_{\rm DM}$, as demonstrated in the shape of $\tau_{\rm DM}$ constraint. This leads to a significant $\mathcal{O}(10^{27})$s bound for sub-GeV dark matter lifetime that is complementary to gamma-ray search limits [100, 101] from Fermi-LAT data. The 21 cm bound is also stronger than the CMB damping constraint from *Planck* [33] by more than one order of magnitude. This indicates that the $T_{\rm S} \simeq T_{\rm G}$ in the reionization epoch is a very sensitive test of energy injection. $\mu^+\mu^-$ and $b\bar{b}$ final states for masses above 30 GeV produce weaker bounds than Fermi-LAT's dwarf galaxy [100] and Galactic [86, 102] gamma-ray measurements. $\tau^+\tau^-$ final states result in weaker bounds for all tested masses but reach comparable results at $m_{\rm DM} = 10$ GeV. Because e^+e^- produces few gamma-rays and has a high $f(E,z)$, the 21 cm result is expected to be much more constraining than an analysis with Fermi-LAT results.

The shape of the constraints is a direct result from the effective efficiency maps discussed in Sec. 2.1. Masses that occur near a peak absorption efficiency have a corresponding high constraint. The shifting of the peaks between *Planck* and 21 cm results is due to the z dependence of the effective efficiency. Dominant features present

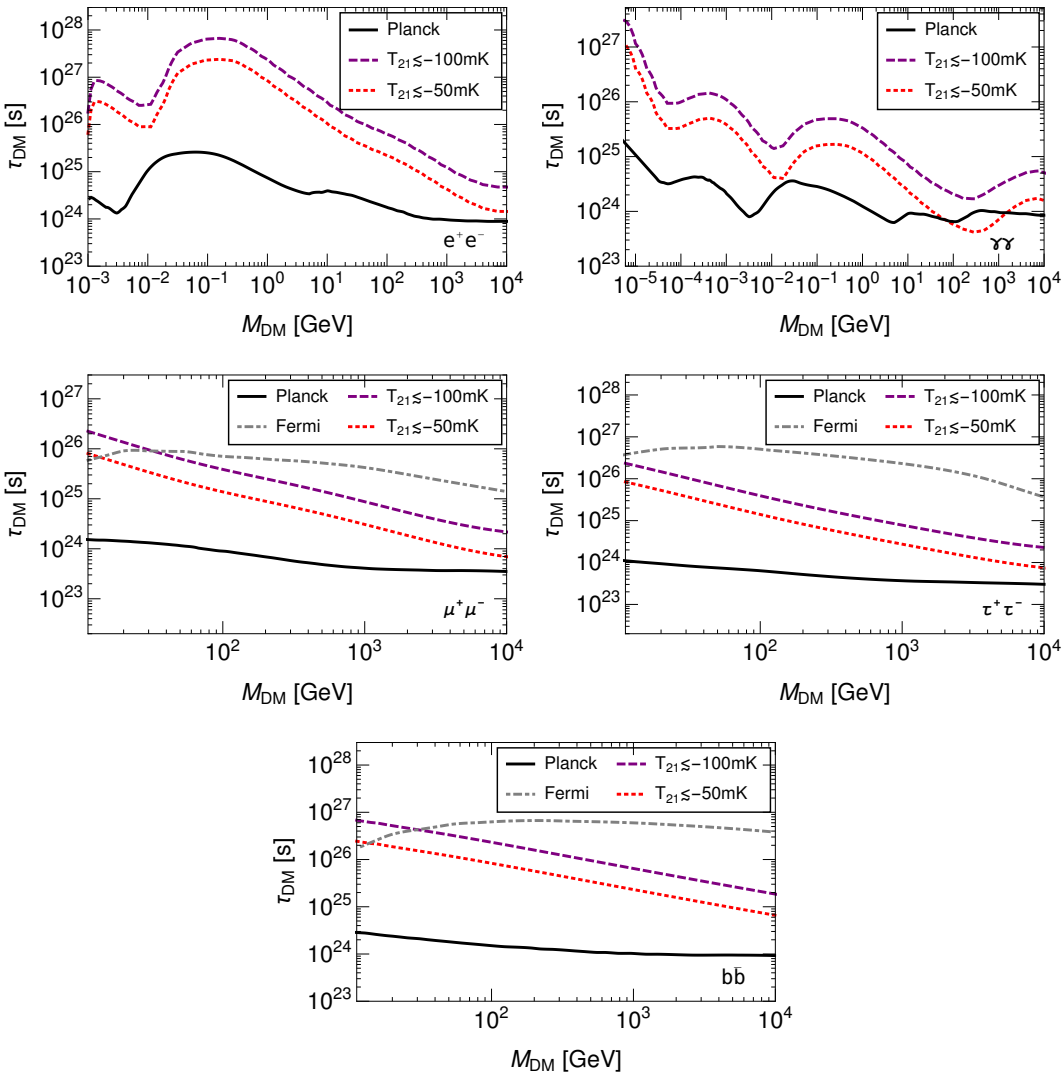

Figure 4.1: Dark matter decay constraints. 21 cm lower-bounds on dark matter decay lifetime. The dark matter decay panels assume DM $\to e^+e^-$ (top left), DM $\to \gamma\gamma$ (top right), DM $\to \mu^+\mu^-$ (center left), DM $\to \tau^+\tau^-$ (center right), and DM $\to b\bar{b}$ (bottom) final states. Current CMB damping constraints [33] from *Planck* (solid) and dwarf galaxy bounds [100] from Fermi-LAT (gray dashed) are also shown for comparison. Reprinted with permission from Ref. [56].

in the efficiency map shift to higher dark matter masses at late redshift and are observed in the calculated maps [19].

Also note the enhanced lifetime in the $\gamma\gamma$ channel at injection below 0.1 MeV due to higher photon energy absorption efficiencies. At ∼KeV mass dark matter, the lifetime bound is higher than 10^{27}s. This bound is below the $10^{29}\text{s}\cdot(M_{\rm DM}/\text{KeV})$ [103] requirement for explaining the 3.5 KeV X-ray excess [104]. Testing this signal would need $\mathcal{O}(\text{mK})$ T_{21} sensitivity at future measurements.

4.2 Primordial Black Holes

Shortly after the Big Bang, large density fluctuations in the early Universe may have resulted in the formation of primordial black holes (PBHs) [105–108]. There is a wide range of allowed masses for PBHs. Depending on the epoch and conditions during formation, PBH masses can be anywhere from approximately a gram to a million solar masses. While low mass PBHs would have already evaporated through Hawking radiation [109], large ones with masses $M_{\rm BH} > 5 \times 10^{14}$ g would still be present today. It is also possible to have prolonged PBH formation during a non-radiation-dominated phase of the Universe where PBHs can form with a continuum mass distribution, rather than mostly at one particular mass scale as in the conventional radiation dominated case [110–113]. Stable PBHs can be cosmologically-significant, and may serve as an ideal dark matter candidate [114]. For a review of PBH formation and relevant constraints, see Ref. [115–117], and Ref. [118] for constraints on horizonless exotic compact objects. Also see Ref. [112, 119, 120] for recent studies of PBH formation under nonthermal conditions.

Depending on PBH abundance, Hawking radiation from PBHs with lifetimes longer than the age of the universe may be observable. Extragalactic gamma-rays strongly constrain PBHs in the mass range $\sim 10^{15} - 10^{17}$ g [114]. PBHs in the mass range $\sim 10^{17} - 10^{20}$ g are bounded by femtolensing of gamma-ray bursts [121], and PBHs in the mass range $\sim 10^{-10} - 10$ $\text{M}_\odot$ are constrained by gravitational microlensing [122].

In addition, PBHs with mass $\gtrsim 10\ M_\odot$ may be constrained by the accretion of matter in the early universe [119, 123, 124]. Black holes at approximately this mass are constrained by X-rays observations [125].

Our focus on PBHs will be to set new constraints in the mass range $\sim 10^{15} - 10^{17}$ g using the most recent *Planck* cosmic microwave background (CMB) data [32] and 21 cm [114, 126] EDGES results [2, 52]. The CMB is sensitive to additional sources of energy injection during the recombination epoch, which leads to damping of the anisotropies. For PBHs, this energy injection is due to Hawking radiation. As we show, the *Planck* and EDGES data now places a stronger bound on PBHs over a larger fraction of this mass range than the previous most stringent bounds derived from the extragalactic gamma-ray background (EGB). Other authors have also used *Planck* data to bound PBHs in the mass regime that we study [127, 128]; as discussed below we precisely identify the mass regime over which the CMB and EGB bounds are dominant. In addition we note that our analysis is distinct from previous studies that used early-time distortions of the CMB to bound PBHs in the mass range $10^{11} - 10^{12}$ g [129].

The theoretical formalism that we utilize to constrain PBHs is similar to that used to constrain dark matter annihilations and decays [16, 19, 21, 22, 130]. From the perspective of energy injection, PBH evaporation is most similar to decaying dark matter in that the energy injection only depends on the PBH mass, PBH abundance, and is occurs at a fairly steady rate to present time. This energy injection can have a significant impact on ionization at low redshift. However unlike dark matter which can frequently produce heavy Standard Model particles, PBHs with mass $> 10^{15}$g mostly radiate electrons, photons, and other (near) massless species, but generally not much heavier particle species. Because PBHs with mass $> 10^{18}$g are too cold to emit electrons, their injection into the CMB is unobservable, and the bounds are weak above this mass.

4.2.1 Blackhole Radiation Properties

PBHs radiate a spectrum of particles through Hawking radiation, which decay into photons, electrons, protons, and neutrinos. These particles then deposit their energy into the IGM, see Sec. 2. PBH energy injection is described by

$$\begin{aligned}\frac{\mathrm{d}E}{\mathrm{d}V\mathrm{d}t} &= \dot{M}_{\mathrm{BH}}\, c^2\, n_{\mathrm{BH}} \\ &= \frac{\dot{M}_{\mathrm{BH}}}{M_{\mathrm{BH}}}\, \rho_c\, c^2\, \Omega_{\mathrm{BH}}(z) \\ &= \frac{\dot{M}_{\mathrm{BH}}}{M_{\mathrm{BH}}}\, \rho_c\, c^2\, \Omega_{\mathrm{BH},0}\, (1+z)^3,\end{aligned} \tag{4.2}$$

where n_{BH} is the PBH number density, ρ_c is the critical density of the Universe today, M_{BH} is the PBH mass, $\Omega_{\mathrm{BH}}(z)$ is the PBH density relative to the critical density, and $\Omega_{\mathrm{BH},0}$ is the value of $\Omega_{\mathrm{BH}}(z)$ today.

Note that the above equations assume that PBHs are comprised of a single mass and the mass does not changes as it radiates. This is satisfied as long as the lifetime is large compared to the age of the universe and is satisfied by the masses considered, $M_{\mathrm{BH}} = 10^{15} - 10^{17}$ g, to at worst the percent level. Apart from some cosmetic differences, Equation 4.2 is identical to that for decaying dark matter, Equation 4.1 [33].

The characteristics of the PBH radiation spectra are equated through Hawking radiation to that of a blackbody object radiating with temperature

$$T_{\mathrm{BH}} = \frac{1}{8\pi G M} = 1.06\,\mathrm{TeV} \times \frac{10^{10}\,\mathrm{g}}{M_{\mathrm{BH}}} \tag{4.3}$$

and with an emission spectrum

$$\frac{\mathrm{d}N}{\mathrm{d}E\mathrm{d}t} \propto \frac{\Gamma_s}{e^{E/T_{\mathrm{BH}}} - (-1)^{2s}}, \tag{4.4}$$

where s is the spin of the radiated particle, and Γ_s is the absorption coefficient for the

particle. For low $T_{\rm BH}$, the absorption coefficient can deviate greatly from the geometric optic limit [131, 132],

$$\Gamma_s(M, E) = \frac{27G^2M^2E^2}{\hbar^2c^6}. \tag{4.5}$$

Hawking radiation causes black holes to lose mass at a rate [114, 131, 132]

$$\dot{M}_{\rm BH} = -5.34 \times 10^{25} F(M_{\rm BH}) M_{\rm BH}^{-2}\,{\rm g}^3\,{\rm s}^{-1}. \tag{4.6}$$

where $F(M_{\rm BH})$ is a measure of the fraction of emitted particles normalized to unity for $M_{\rm BH} \gg 10^{17}$ g, and evaluated by summing over the various particles.

$$F(M_{\rm BH}) = \left(\sum_i f_i\right) \tag{4.7}$$

The fractions for particles of different spins emitted in the region of interest are [132]

$$\begin{aligned} f_0 = 0.267, \quad f_1^\gamma = 0.06, \quad f_{3/2} = 0.02, \\ f_2^g = 0.007, \quad f_{1/2}^\nu = 0.147, \quad f_{1/2}^{e\pm} = 0.142. \end{aligned} \tag{4.8}$$

Equations 4.2 and 4.6 are combined with the emitted spectra fractions from Equation 4.8 to provide the energy injection rate for PBH. For $M_{\rm BH} = 10^{15} - 10^{17}$ g, this rate is

$$\frac{{\rm d}E}{{\rm d}V{\rm d}t} = 3.67 \times 10^{25}\, M_{\rm BH}^{-3}\, \rho_c\, c^2\, \Omega_{\rm BH,0}\, (1+z)^3\, {\rm g}^3\, {\rm s}^{-1}. \tag{4.9}$$

Because neutrinos do not interact with the medium, they have been ignored from this calculation. In order to account for this, they are also ignored in the PBH effective efficiency calculation. We have verified that this simplification for PBHs is valid. The only error introduced with these assumptions is an underestimation in the PBH mass loss rate. Because we are considering PBH that do not change mass by an appreciable amount over the age of the Universe, this underestimation has no affect on the results.

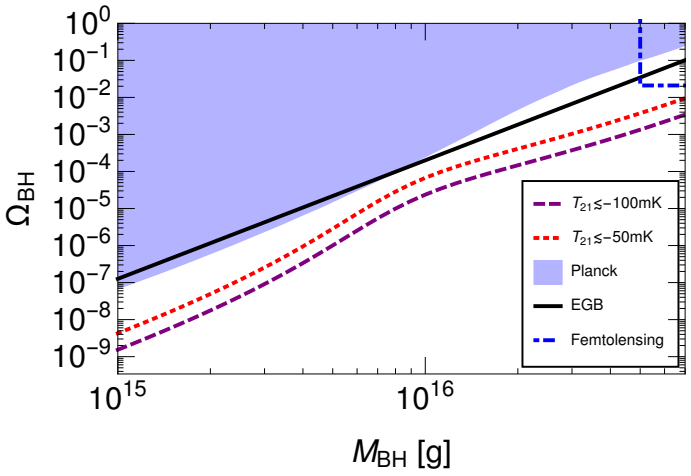

Figure 4.2: PBH constraints. CMB damping exclusion bounds [23] for $\Omega_{\rm BH}$ at the 95% confidence level (shaded region) and the 21 cm bound estimates for ΔT of -100 (dashed) and -150 mK (short dashed) [56] compared with the same exclusion bound enforced by extragalactic gamma-ray background [23, 114] (solid) constraints, assuming 100% of the background produced by PBHs and the femtolensing excluded area [115, 133] (top right). Reprinted with permission from Ref. [56].

4.2.2 PBH constraints

Figure 4.2 shows the 95% confidence limit from *Planck* CMB measurements as well as the 21 cm EDGES estimate bounds for $T_{21} = -50$ and -100 mK. The constraints follow the expected inverse cube relationship to the PBH mass which is predicted by the energy injection formula with 21 cm beating out *Planck* by an order of magnitude.

In addition to the cubic dependence on mass, there is also a highly nonlinear relationship to the effective efficiency. This nonlinearity is most prevalent for PBH masses around $1 - 4 \times 10^{16}$ g [23] for CMB and peaks at 10^{16} g for 21 cm [56]. Comparing effective efficiencies, in Figure 2.4, the trend is correlated with the efficiency values that occur near the time of recombination and reionization respectfully. As the efficiency value decreases, it is required for a larger amount of total energy to be created in order to produce the same effect. For this reason, as the efficiency experiences a large decrease in this mass range, the allowable maximum mass fraction increases. This

nonlinear behavior is also observed in [127] to a much lesser degree.

The EGB constraints were recreated following the prescription outlined in Ref. [114, 115], the number density of photons, $n_{\gamma 0}$, with energy $E_{\gamma 0}$ and their intensity is

$$n_{\gamma 0}(E_\gamma) = \frac{\Gamma_{\rm BH}}{M_{\rm BH}} E_\gamma \int_{t_{\rm min}}^{\min(t_0,\tau)} {\rm d}t (1+z)^{-2} \frac{\dot{N}_\gamma}{E_\gamma}(M_{\rm BH}, (1+z)E_\gamma) \tag{4.10}$$

$$I = \frac{c}{4\pi} n_{\gamma 0} \tag{4.11}$$

where $t_{\rm min}$ is the time when photon creation begins. The quantity $\dot{N}_\gamma / E_\gamma(M_{\rm BH}, E_\gamma)$ is the photon spectrum given by Equation 4.4, which we take at the high energy limit. For PBHs in our mass range, peak intensity occurs at $\sim 1 - 30$ MeV. Constraints were imposed by matching the intensity to the upper bound of the COMPTEL EGB experimental data [134].

EGB constraints are also shown in Figure 4.2 as well as those imposed by femtolensing [115]. Currently, *Planck* provides the strongest constraints on the abundance of PBHs for masses $\sim 10^{15} - 10^{16}$ g, while the EGB dominates for masses $\gtrsim 10^{16}$ g. We find that 21 cm have the potential to be stronger than all of the other results.

Note that while using a similar approach, this conclusion differs from that of Ref. [127]. Figure 4.3 shows a comparison between the results calculated in this work and those from Ref [127]. For low mass PBHs, our work calculates a stronger constraint than the EGB; for larger masses, a weaker constraint is produced. The calculation in Ref [127] has the opposite relationship.

4.2.3 Continuum Photons

Injections also produce a of continuum photons that can affect the CMB by creating spectral distortions [21]. The continuum is defined as the photons produced by injection that are sub 10.2 eV, and thus do not interact with neutral Hydrogen. The continuum photons contribute by altering the CMB signature away from a Boltzmann distribution. Ref. [135] investigated limits to these spectral distortions modeling the distortions as

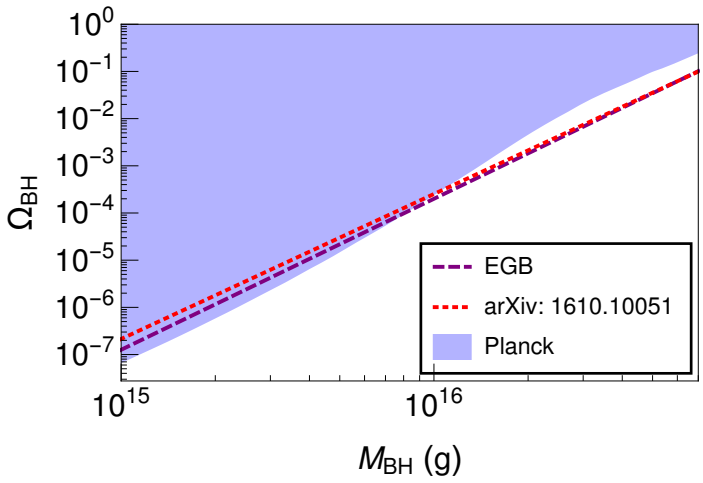

Figure 4.3: Comparison of PBH CMB results to other works. CMB exclusion bounds for $\Omega_{\rm BH}$ at the 95% confidence level (shaded region) [23] compared with the same exclusion bound enforced by EGB, assuming 100% of the background produced by PBHs (dashed). Also included is an approximation of the bound found in Ref. [127] (short dashed). Reprinted with permission from Ref. [23].

a Bose-Einstein distribution with a chemical potential μ, μ-type distortions. In order to get a baseline estimate on the effect that continuum photons produced by a dark matter candidate have on the CMB, we conducted a similar approach. Assuming the injection alters the perfect blackbody spectrum with the same μ-type distortions, these distortions will be approximately

$$\mu = 1.4\frac{\delta\rho_\gamma}{\rho_\gamma} = 1.4\int_{t_1}^{t_2}\frac{\dot{\rho}_\gamma}{\rho_\gamma}\mathrm{d}t, \tag{4.12}$$

where ρ_γ and $\dot{\rho}_\gamma$ are the energy density of the CMB and the distortion injection rate on the CMB respectfully. $\dot{\rho}_\gamma$ is the interaction injection rate into the continuum. The result is

$$\mu = 1.4\int_{z_1}^{z_2}\frac{(\mathrm{d}E/\mathrm{d}V\mathrm{d}t)_{\rm Cont.}}{\rho_c\Omega_\gamma(1+z)^4}\frac{\mathrm{d}z}{(1+z)H(z)}, \tag{4.13}$$

with $\Omega_\gamma h^2 \sim 2.47\times10^{-5}$.

Current limits on these distortions are $|\mu| < 9.0\times10^{-5}$ at two sigma [135]. A

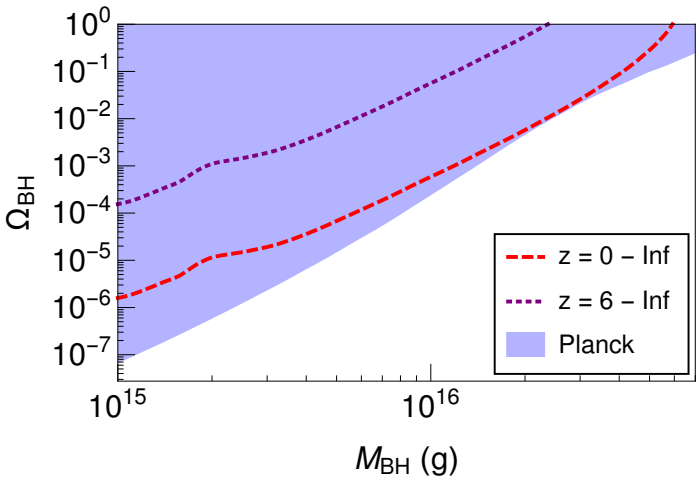

Figure 4.4: PBH CMB constraints compared with limits imposed by spectral distortions. Exclusion bounds for the fraction of dark matter composed of black holes at the 95% confidence level for CMB anisotropies (shaded region) and spectral distortions. The various curves correspond to different integration limits in Equation 4.12. The most constraining uses $z = 0$ to infinity (dashed), and the second uses $z = 6$ to infinity (short dashed). Reprinted with permission from Ref. [23].

comparison of this constraint and the CMB value discussed in this section is shown in Figure 4.4. The constraints produced by CMB are stronger by several orders of magnitude than limits produced assuming a μ-type or similar distortion. The only limits that approach the CMB result are those that consider alterations at extremely late times; however, these can be ignored because CMB photons at late redshifts are already much cooler than the 10.2 eV limit assumed by the injections in this calculation. Therefore, the actual constraints on by more careful analysis would be weaker.

4.3 Four-body Annihilation

Dark matter annihilation into Standard Model (SM) particles is now being probed by many high energy gamma-ray and cosmic ray experiments. Of particular interest are Fermi-LAT observations of dwarf spheroidals (dSphs) [4–8] which have constrained s-wave dark matter at the thermal relic scale for dark matter with mass $\sim 10 - 100$ GeV, for several well-motived annihilation channels. These results are complemented by cosmic microwave background (CMB) data, most recently from the *Planck* satellite [1],

which extend the constraints on thermal relic dark matter to lower masses.

Though the aforementioned observations do not show conclusive evidence for a dark matter annihilation signal, there are several results when considered separately that may be consistent with a dark matter annihilation interpretation. These include the long-standing Fermi-LAT galactic center excess (GCE) [90, 136–139], and more recently the antiproton measurements from AMS [89]. These possible hints of dark matter may be reconciled with the null results from the Fermi-LAT and CMB for some well-motivated dark matter annihilation models [92, 140–145]. However, there is not a large region of dark matter mass and annihilation cross-section parameter space in which the dark matter annihilation interpretation of these data sets are mutually satisfied.

We study a wide range of dark matter annihilation final states, and using these, explore the possibility that all of the above experiments may be consistent with one another. In particular, we focus on four-body final states, final states that arise through the decay of a light mediator. In all of these scenarios, we compute the energy injection into the intergalactic medium (IGM) which imparts a measurable imprint on the CMB, and place constraints on the annihilation cross-section using the latest data from *Planck*. We compare these constraints to similar ones imposed by Fermi-LAT and at higher energies by MAGIC [146] and VERITAS [147]. We explore whether or not these constraints are consistent with the dark matter annihilation interpretation of the antiproton excess measured by AMS [92, 140], and show that for light mediators it is possible to explain the AMS data with dark matter annihilation, and remain consistent with the GCE, for dark matter masses $m_\chi \sim 60 - 100$ GeV and mediator masses $m_\phi/m_\chi \lesssim 1$.

Here, we investigate the differences in constraints between the typical two-body annihilation verse a four-body annihilation. In the two-body case, we assume fermionic dark matter annihilates a Standard Model anti-particle pairs, $\chi\,\chi \to \mathrm{SM}\,\overline{\mathrm{SM}}$. For the

four-body example, fermionic dark matter annihilates to two new scalars. These scalars then decay into Standard Model anti-particle pairs; $\chi\chi \to \phi\,\phi$, followed by $\phi \to \mathrm{SM}\,\overline{\mathrm{SM}}$.

For both cases, the energy injection rate is

$$\frac{\mathrm{d}E}{\mathrm{d}V\,\mathrm{d}t} = \rho_c^2\, c^2\, \Omega_{\mathrm{DM}}^2\, \frac{\langle\sigma v\rangle}{M_{\mathrm{DM}}}\, (1+z)^6, \tag{4.14}$$

where ρ_c is the critical density of the Universe and Ω_{DM} is the dark matter content, both measured at $z = 0$. The thermally averaged cross-section is $\langle\sigma v\rangle$, and m_χ is the dark matter mass [16].

4.3.1 Four-body Annihilation Constraints

We constrained the annihilating dark matter models with *Planck* data. We also compared with results from some high energy gamma-ray experiments, in particular Fermi-LAT, MAGIC, and VERITAS. Most of the published constraints by Fermi-LAT, MAGIC, and VERITAS have been calculated for two-body final state models. Using these constraints, we estimated the four-body constraints following the prescription outlined in Ref. [148]. This procedure hinges upon the photon energy spectrum from multiple species being similar and allows us to cast a calculated constraint from one model into an unknown model simply by comparing the spectra. To perform this relationship, we consider the relation,

$$\langle\sigma v\rangle_4 = \langle\sigma v\rangle_2 \times \left(\frac{m_{\chi,4}}{m_{\chi,2}}\right)^2 \times \int_{E_{min}}^{E_{max}} \frac{\mathrm{d}N_2}{\mathrm{d}E_\gamma}\,\mathrm{d}E_\gamma \times \left(\int_{E_{min}}^{E_{max}} \frac{\mathrm{d}N_4}{\mathrm{d}E_\gamma}\,\mathrm{d}E_\gamma\right)^{-1}, \tag{4.15}$$

where 2 and 4 are tags that denote quantities from the two- and four-body models respectively, E_{min} and E_{max} are the lower and upper bounds for the measured photon energies, and $\mathrm{d}N/\mathrm{d}E_\gamma$ is the photon spectrum from the process, including the decays of unstable products. The four-body dark matter mass is chosen so that its spectrum, defined as $(E_\gamma)^2\mathrm{d}N_4/\mathrm{d}E_\gamma$, has a peak at the same energy as the peak of the two-

Annihilation Model	Fermi-LAT	Fermi-LAT + MAGIC	VERITAS
4τ	2τ	2τ	2τ
$2b2\tau$	$2b$	$2b$	$2b$
$2t$	$2b$	$2b$	—
$4b$	$2b$	$2b$	$2b$

Table 4.1: Spectral combinations for converting constraints from two- to four-body. Estimate constraints for models in the first column were produced for each experiment listed in the first row by converting bounds from the listed model as described in Equation 4.15. The symbol (—) signifies the constraint has already been calculated for the respective experiment. Reprinted with permission from Ref. [28].

body spectrum for a given mass $m_{\chi,2}$. The energies E_{min} and E_{max} are set at 0.5 GeV and m_χ respectively for Fermi-LAT and Fermi-LAT+MAGIC. They are set at 50 GeV and up to 50 TeV for VERITAS. Because we are scaling the four-body spectrum constraints from the two-body constraints, we note that starting with different two-body spectra may produce different constraints on four-body models. To minimize the error introduced through this method, we started with the two-body spectrum that most closely matches the extrapolated model. Table 4.1 lists the two-body spectra used to produce the four-body constraints when using Equation 4.15.

Figure 4.5 combines the limits calculated from *Planck* as well as those converted for Fermi-LAT, MAGIC, and VERITAS. Each line represents the respective 95% confidence limit. The overall effect for the Fermi-LAT, MAGIC, and VERITAS bounds moving from two- to four-body is a slight weakening. This shift originates from a larger fraction of photons being produced below the detection threshold. For *Planck*, on the other hand, the limits for two- and four-body final states are very similar. This similarity is attributed to the CMB being sensitive to the total energy injected into its system rather than on the particular spectra of injected particles, which results in very different models having near identical constraints. Because the *Planck* bound is stationary while Fermi-LAT, MAGIC, and VERITAS weaken in response to changing between two- and four-bodies, the *Planck* bounds tend to strengthen slightly in

comparison to the other constraints.

For the lepton final states, 2τ and 4τ *Planck* constraints are significantly weaker than Fermi-LAT up to mass $\sim$ TeV, above which the *Planck* constraints are stronger as Fermi-LAT loses sensitivity. At higher masses, the *Planck* constraints are comparable to, but slightly weaker than, the VERITAS bounds, and are generally weaker than the MAGIC constraints. The *Planck* constraints on the $2e$ and 2μ final states, on the other hand, are stronger than Fermi-LAT at low masses, and are significantly stronger at higher masses. As the *Planck* constraints continue into the TeV range, they are much stronger than VERITAS. With the addition of MAGIC, the constraints from Fermi-LAT, MAGIC, and VERITAS approach the *Planck* result $\sim$ 400 GeV and $\sim$ 1 TeV. We note that the simple prescription used to estimate constraints based on different channels cannot be used for MAGIC to obtain $2e$ constraints due to the lack of a well defined peak in its spectrum. However, the $2e$ bounds would be expected to be similar to those from 2μ because of their spectral similarities.

For the quark and quark-lepton final states, the constraint for $2t$, $2b$, $4b$, $2b2\tau$, and $2W$ are almost identical because of their similarities in decay chains. At low energies, *Planck* constraints are significantly weaker than Fermi-LAT throughout Fermi-LAT's sensitive range. At higher energies, *Planck* limits are comparable to slightly stronger than the VERITAS bounds up to the end of its range. The MAGIC results are stronger than both *Planck* and VERITAS at high masses.

In general, we note that Fermi-LAT continues to have stronger constraints for lower dark matter masses than *Planck*. At the high end, *Planck* is comparable to VERITAS and at some masses is better than VERITAS; however, it is usually weaker than MAGIC at higher masses. It should be noted that due to Fermi-LAT, MAGIC, and VERITAS having poor efficiencies for light particles, *Planck* produces a stronger constraint for electrons and muons at all dark matter masses.

The tension between Fermi-LAT and galactic center excess dark matter interpreta-

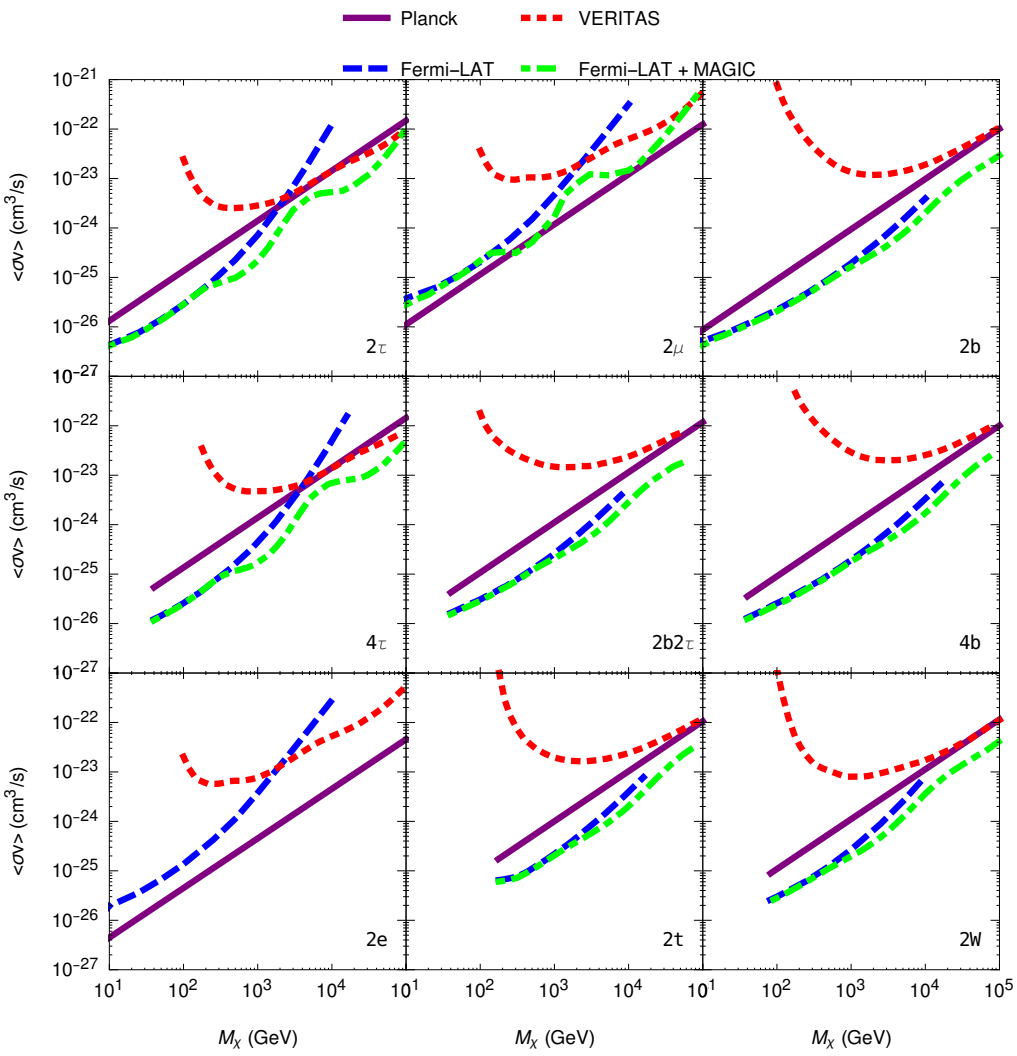

Figure 4.5: Two- and four-body annihilation constraints. Constraints on the annihilation cross-section for several channels using *Planck*, Fermi-LAT, Fermi-LAT + MAGIC and VERITAS. The limits are at the 95% level. Reprinted with permission from Ref. [28].

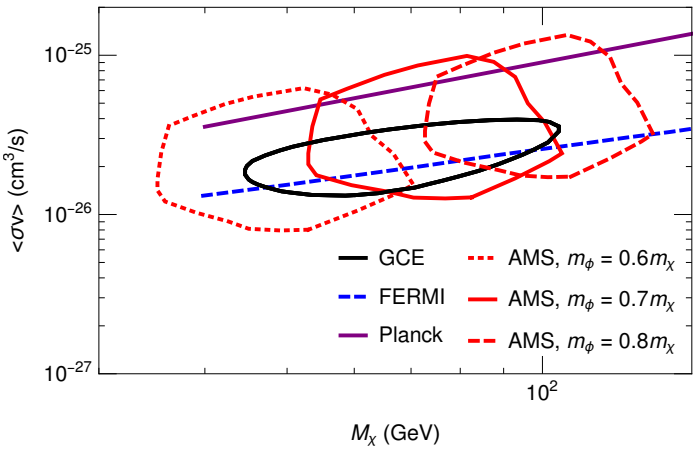

Figure 4.6: $4b$ antiproton best fit results. Constraints imposed by AMS data (red) for $\chi\chi \to \phi\phi$ followed by $\phi \to b\bar{b}$. Also shown are the upper limits on dark matter annihilation calculated by Fermi-LAT (blue), *Planck* (purple), and GCE (black). Reprinted with permission from Ref. [28].

tions is also loosened through transitioning from two- to four-body annihilation [148]. By incorporating these results with those for $4b$ antiproton and connecting it to the $2b$ antiproton constraints from Ref. [92] through a similar process as the photon conversion as described in Sec. 3.3, further constraints on the four-body parameter space can be made. In Figure 4.6, we show the allowed region to explain the antiproton data. Each line represents the respective 95% confidence limit. The preferred region depends greatly on the mediator mass with larger mediators preferring heavier dark matter masses and higher annihilation cross-sections due to the mediator becoming less boosted with increased mass. This shifting of the preferred parameter space permits measurements of the antiproton flux to differentiate between different four-body annihilation models. The best overlap with other experiments occurs at a mediator mass of approximately 70% the dark matter mass. This region shows good overlap with other experiments, particularly the GCE, and is consistent with both Fermi-LAT and *Planck* bounds.

Since the $4b$ final state provides a good fit to the GCE and the AMS antiproton

data, one may wish to construct a model for such final states arising from dark matter annihilation. In Ref. [148], an additional $U(1)_{B-L}$ was considered to fit the GCE after satisfying the null detections from dwarf spheroidal galaxies. In this model, the dark matter candidate annihilates into two new Higgs (ϕ), which finally decays into mostly $2b$ and 2τ via a loop containing an extra heavy Z boson associated with the new gauge symmetry. However, for the combined AMS and the GCE fit, the presence of τ in the final state creates a problem. In this case, an additional $U(1)_{B-xL}$ symmetry can be invoked to obtain the fit where $0 \leq x \leq 1$. For the best fit $x \to 0$ is needed, where each ϕ primarily decays into $2b$ and the dark matter annihilation dominantly produces $4b$ in the final state.

4.4 Bremsstrahlung Annihilation

The annihilation cross-section, $(\sigma v)_{\rm ann}$, is one of the key quantities that describes the nature of dark matter interactions with the Standard Model. The annihilation cross-section in the early universe sets the relic abundance for thermally produced dark matter. There are several observational bounds on the annihilation cross-section, for example high energy gamma-ray data [8, 147] and the cosmic microwave background (CMB) [149] as we saw in Sec. 4.3. The redshifted 21 cm line arising from a spin-flip transition in neutral hydrogen gas prior to the era of recombination [150] has recently been recognized as an important probe of dark matter annihilation and decay. The 21 cm measurements are sensitive to the annihilation cross-section at redshifts $z \lesssim 15$ [52].

The dark matter annihilation cross-section can be expressed as a partial-wave expansion in powers of the square of the relative velocity between the annihilating particles [151]. The evolving nature of the dark matter velocity implies that the leading order annihilation process may differ over the course of the evolution of the universe and during cosmological structure formation. For example, dark matter that is a Majorana fermion can naturally annihilate dominantly as a p-wave process, $(\sigma v)_{\rm ann} \propto v^2$, during the era of dark matter freeze-out where the relative velocity

squared is $v^2 \sim T/m_{\rm DM} \sim 1/20$. There exist s-wave annihilation channels to two fermion final states, for example, but these are chirality suppressed by mass ratio factors of $(m_f/m_{\rm DM})^2$ [152]. This can be contrasted with dark matter in the galactic halo, which has a virial velocity $v^2 \sim 10^{-6}$, and thereby reduces the observational importance of the p-wave process. This implies that annihilation to three-body final states, which proceed via s-wave annihilation due to the bremsstrahlung of a bosonic state [153], can provide the leading order annihilation channel.

Typically, three-body annihilation dominates over two-body annihilation as the mass of the particle mediating the interaction approaches that of the dark matter [154–159]. This also provides an alternative means of accessing the parameter space in the so-called compressed mass region, where the masses are nearly degenerate. However, the degeneracy does not need to be extreme in order to obtain a large effect from vector bremsstrahlung, which provides a natural region of parameter space that can be probed by experiment.

These considerations suggest that, in the case of dark matter annihilation to fermion pairs, final state radiation and internal vector bremsstrahlung of photons and the electroweak W/Z bosons are irreducible processes which present an interesting target for observational searches. Photon bremsstrahlung can produce a line-like spectral feature [153], and the subsequent decay of the radiated W and Z bosons produce additional diffuse photon signals which provide a complementary avenue of investigation.

Here, we examine constraints on dark matter annihilating predominantly through s-wave channels in the present universe as a result of electromagnetic and electroweak bremsstrahlung, but whose relic abundance is set in the early universe by p-wave annihilations. We consider Fermi-LAT observations of dwarf spheroidals (dSphs) and diffuse gamma-ray data. We are thus able to simultaneously probe both of these partial wave components for a single dark matter model. We demonstrate that current observations are able to constrain such models, which can be contrasted with the case

of dark matter annihilating only through p-wave processes which is wholly inaccessible to observational limits. We discuss the constraints in the context of both thermal and non-thermal models. Bounds on the dark matter annihilation cross-section from 21 cm observations are also presented along with a comparison to the constraints from CMB data.

We highlight in particular the final state consisting of neutrinos only. This two-body final state is quite difficult to probe observationally, but the addition of a final state photon allows for more strict experimental constraints. [160] A complication arises due to $SU(2)_L$ invariance, which makes producing a neutrinos-only final state as the dominant annihilation channel a non-trivial task, as one would expect the annihilation to also produce charged leptons. However we introduce a model which produces a neutrino-only final states without allowing final state charged lepton production, while respecting gauge invariance.

4.4.1 Lifting velocity suppression via bremsstrahlung

In what follows, we will adopt a single-component SUSY-inspired simplified model of dark matter consisting of a Majorana dark matter particle, χ, whose fractional abundance gives the totality of the dark matter ($f_{\rm DM} = 1$), and which annihilates to Standard Model particles through t- and u-channel exchange of a charged scalar.

The annihilation cross-section for a pair of non-relativistic dark matter particles of total orbital angular momentum L and relative velocity, v, is expressed as a partial wave expansion $\sigma v \propto v^{2L}$ [151]. Using general considerations [161, 162], one finds that models with Majorana pair annihilation may naturally proceed dominantly through a p-wave process. As it has s-channel annihilations only through pseudoscalar, scalar, or axial-vector exchange with $L = 0$, s-wave processes arise only in models with pseudoscalar mediators, though the pseudoscalar typically couples through a Yukawa-like interaction, introducing a mass suppression in the same mold as chirality suppression. As is well-known [152], the axial-vector exchange also contributes an $L = 0$ partial-wave

which is chirality suppressed for annihilation to light final state fermions of mass m_f by the factor $m_f^2/m_{\rm DM}^2$. There also exist t- and u-channel annihilation modes through scalar exchange (as in SUSY and SUSY-inspired models) that produce chirality suppression, as can be seen through a Fierz transformation to the s-channel where the axial-vector contribution is apparent [163].

Chirality suppression for annihilation to a pair of final state fermions may be evaded by annihilation to a three-body final state through the bremsstrahlung emission of a boson. This has been demonstrated in photon, gluon, and electroweak bremsstrahlung for t- and u-channel annihilation, as well as Higgstrahlung from an s-channel annihilation mode [153–157, 164–168]. For galactic dark matter with virial velocities of $v \sim \mathcal{O}(10^{-3})$, there are regions of parameter space where the three-body final state process can dominate over the two-body final state. Specifically, the three-body final state process will increase relative to the two-body final state as the mediator mass approaches the dark matter mass. However, as we will demonstrate, the splitting between the dark matter mass and mediator mass does not need to be extremely fine tuned in order for a non-negligible effect to arise. This allows for the intriguing situation where the relic abundance of Majorana dark matter can be set by p-wave annihilation while signals at later times are most strongly constrained by s-wave processes induced through bremsstrahlung. It should be emphasized that bounds on dark matter models must necessarily include the effects of such irreducible bremsstrahlung processes.

Inclusion of the photon bremsstrahlung process induces a spectral feature that provides a target in line searches for gamma-ray observatories. This can be seen in the left column of Figure 4.7, which displays the photon spectrum for 100 GeV dark matter annihilating to charged fermion pairs, e^+e^-, $\mu^+\mu^-$, and $\tau^+\tau^-$ for different values of the mediator to dark matter mass ratio from 1.05 to 1.5. We classify these annihilations as two-to-two interactions. We also show the thermally averaged differential cross-section

for $\nu\nu$ cases in Figure 4.8 for mass ratios 1.05 to 2. We use the MSSM with a slepton mediator to calculate the e, μ, τ final states, and introduce a new model to calculate the ν final states, described in the following paragraph. However, this analysis can be applied to any model with the same final states. This spectrum demonstrates the line-like feature that arises at the kinematic endpoint of the annihilation process, as well as showing that the lower energy spectral feature increases as the mediator mass approaches the dark matter mass. If the dark matter mass is large enough to produce on-shell W/Z bosons, as in the right column of Figure 4.7, where the dark matter mass is 300 GeV, the line-like feature persists, but the low energy spectrum is enhanced from W/Z decays.

In addition to searches with final state charged leptons, we also consider neutrino-only final states. Generally speaking, if a model contains a $\nu\bar{\nu}$ final state from dark matter annihilation, indirect detection becomes challenging (though bounds on the annihilation cross-section can be determined [169–172]). However, the situation is improved if a $\nu\bar{\nu}\gamma$ final state is available. One can think about a possible model (for other models that produce a $\nu\bar{\nu}$ final state, see for example [172]) for such a scenario with the following Lagrangian:

$$\mathcal{L} \supset \lambda\phi\phi^*\rho\rho^\dagger + \lambda'\bar{L}_v\rho\nu_R \tag{4.16}$$

Here $\rho = \begin{pmatrix} \rho^+ \\ \rho^0 \end{pmatrix}$ is a Z_2 scalar doublet, which we assume does not get a vacuum expectation value (VEV), and ϕ is a scalar singlet which acts as the dark matter candidate responsible for 27% of the energy density of the universe. The relative masses are such that ϕ is lighter than ρ and L, and ρ can decay to ϕ via a Higgs coupling term given by $\phi^*\rho H$. $\bar{L}_v$ is a vector-like heavy Z_2 odd lepton doublet, and ν_R is a singlet right handed neutrino with a mass of $m_{\nu_R} \simeq 1$ MeV. In such a scenario, the ϕ annihilates into a pair of ν_R via a triangle loop containing $L^\pm$, $\rho^\mp$ or L_v^0, ρ^0. A

photon can be emitted from any of the internal charged legs associated with $L_v^{\pm}$, $\rho^{\mp}$ to make the final state $\nu\bar{\nu}\gamma$.

The spectra were created using the differential cross-section from Ref. [153]. We verified the validity of the expression and also checked that no appreciable variations occur for massive leptons upto the τ mass. We used **Pythia** [24–26] to produce the decay spectrum of unstable particles. The neutrino differential cross-sections were created following the same procedure.

4.4.2 Bremsstrahlung Constraints

The resulting constraints from gamma-ray lines are shown in Figure 4.9 for $\chi\chi \to f\bar{f} + \gamma/W/Z$ final states. We also show the thermally-averaged cross-sections for each of these final states for the scenarios where the dark matter primarily annihilates into $f\bar{f}$ (p-wave dominated) at freeze out. Various colored lines, both for experimental and theory scenarios, are shown for different mediator to dark matter mass ratios. The e, μ, τ final states shown are based on the MSSM model where the neutralino and slepton mass differences vary between 5% and 100%. We note that though we use SUSY for the purposes of an example, this analysis can be applied to any classes of models including t- and u-channel scalar mediators with similar mass ratios to that of the dark matter. LHC searches for slepton masses leave a large amount of unconstrained parameter space for the selectron and smuon for mass differences of $\Delta M(m_{\tilde{e},\tilde{\mu},\tilde{\chi}_1^0}) \leq 60$ GeV with respect to the neutralino DM particle [173], and stau masses are constrained to be $m_{\tilde{\tau}} > 100$ GeV from LEP limits [174–177] (LHC limits on stau masses are approaching a similar level [178]).

The constraints in Figure 4.9 can be used to place constraints on various dark matter scenarios. We find that the constraint rules out a dark matter mass $m_{\rm DM} \lesssim 30$ GeV for a mediator to dark matter mass ratio of $\simeq 5\%$. With the NFWc profile, the constraint becomes 70 GeV for e, μ and τ final states. We used the MSSM parameter space for the charged lepton scenarios. For the $\nu\nu\gamma$ final state we use the model described above

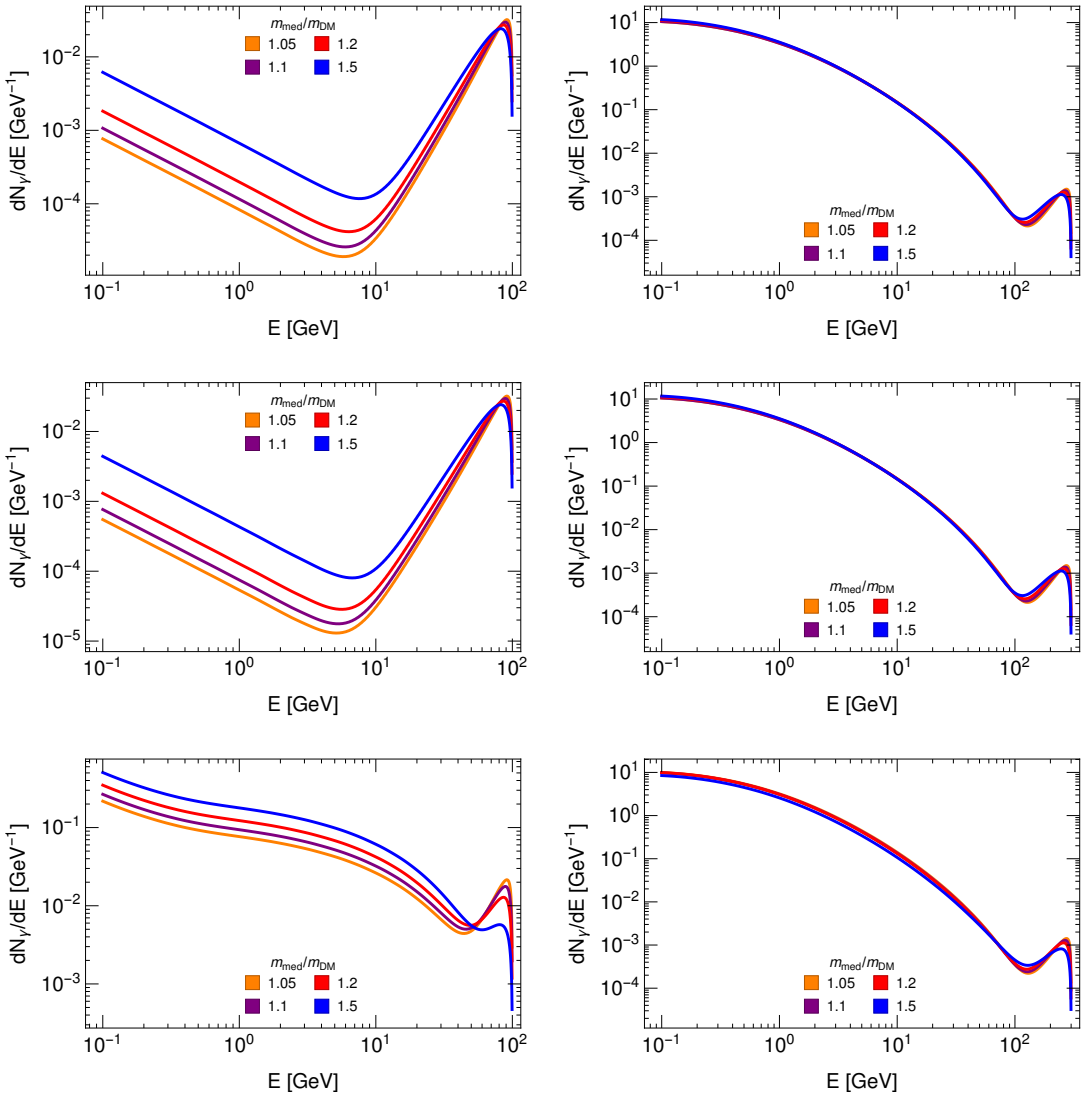

Figure 4.7: Gamma-ray spectra from annihilation to charged leptons and a gauge boson bremsstrahlung. The dark matter has $m_{\rm DM} = 100$ GeV (left) and $m_{\rm DM} = 300$ GeV (right). Various mediator mass ratios, $m_{\rm med}/m_{\rm DM}$, are shown. Lepton final states are electron (top), muon (middle), and tau (bottom). Only the two-to-two and photon bremsstrahlung are considered for the 100 GeV cases while 300 GeV includes the two-to-two and photon/W/Z bremsstrahlung. Reprinted with permission from Ref. [87].

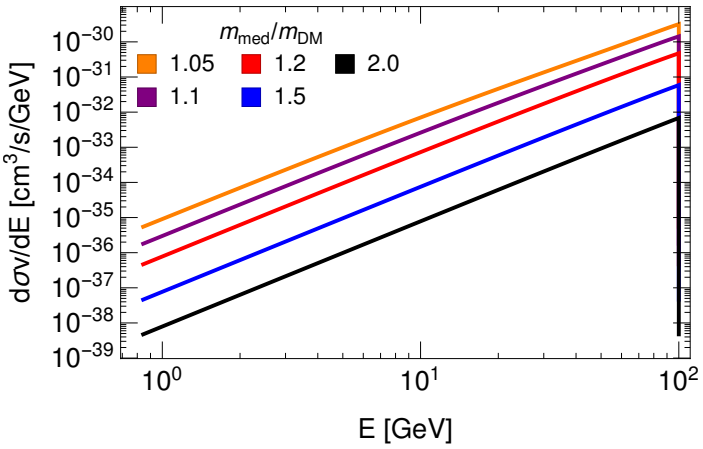

Figure 4.8: Differential thermally averaged cross-section for annihilation to neutrinos and a photon bremsstrahlung. The dark matter has $m_{\rm DM} = 100$ GeV annihilating into neutrino and gamma-ray final states. Various mediator mass ratios, $m_{\rm med}/m_{\rm DM}$, are shown. Reprinted with permission from Ref. [87].

with $\lambda \sim 2$, and we assume all the charged heavy state masses are the same.

In Figure 4.10, we show the current s- and p-wave annihilation rates required to produce the appropriate dark matter abundance. Here we have calculated the mediator to dark matter mass ratios necessary for obtaining the relic abundance with MICROMEGA [179, 180]. In comparison with Figure 4.9, the thermal dark matter line corresponds closely with $m_{\rm med}/m_{\rm DM} = 1.05$ for dark matter masses above 100 GeV. The larger mass ratios presented in the figure can arise in non-thermal scenarios described below. We find that the p-wave component today is small except in the case of lighter dark matter masses. When the dark matter mass becomes small, the mass difference between the mediator and dark matter increases. As the mass ratio increases, the s-wave component is suppressed. We see that the current reach is nearly an order of magnitude from the s-wave component for a dark matter mass around 100 GeV. We do not show the neutrino final state figure here because the p-wave component is model dependent, e.g., based on our Lagrangian we do not have any $\bar{\nu}\nu$ final states unless we assume large values of Dirac mass for the neutrinos. In such a scenario, the $\nu\nu\gamma$ final

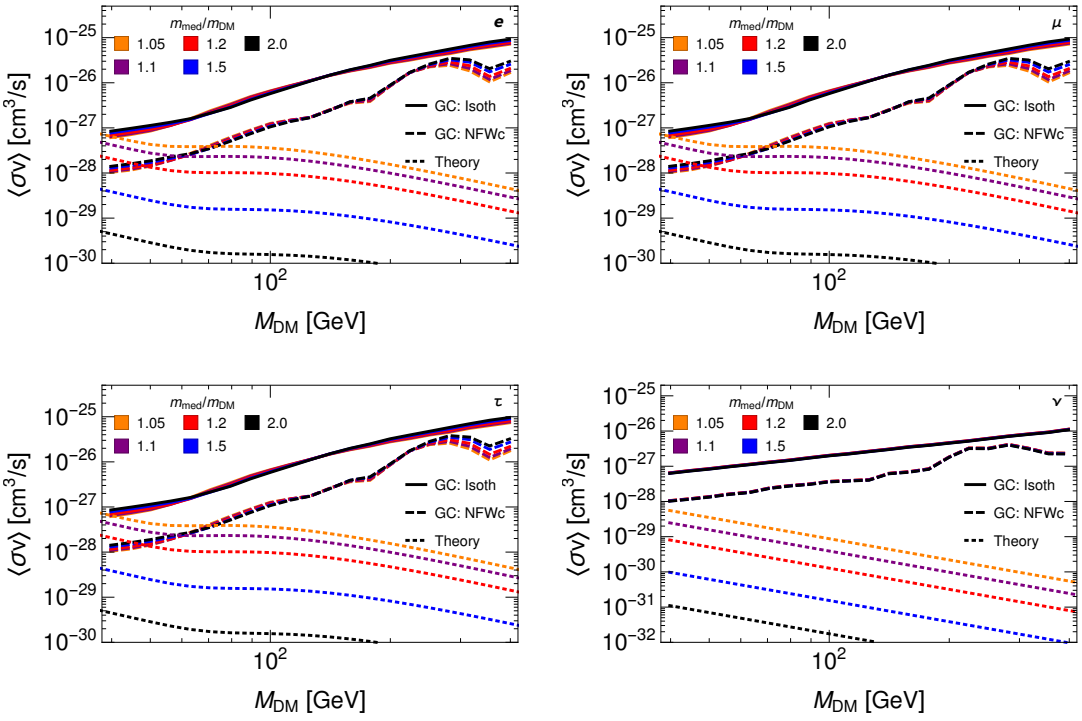

Figure 4.9: Gauge boson bremsstrahlung constraints from the galactic center and theoretical thermal predictions. Constraints on the annihilation cross-section using null detections of gamma-ray lines from Fermi-LAT data (solid lines). These constraints assume the isothermal profile, as defined in the text. The theoretically-calculated cross-section for various mediator mass ratios, $m_{\rm med}/m_{\rm DM}$, are shown as dashed lines. Lepton final states are electron (top left), muon (top right), tau (bottom left), and neutrino (bottom right). The gamma-ray lines constraints using the NFWc dark matter profile are shown as short dashed. Reprinted with permission from Ref. [87].

state would provide the necessary relic abundance.

The non-thermal scenario can be constrained from Figure 4.9. The non-thermal picture emerges generically in UV theories like string theory due to the presence of gravitationally coupled scalars [181–186] which are displaced from their minimum during inflation which can be of order M_P [187]. After the end of inflation, when $H \leq m_{\rm mod}$, the moduli start dominating the energy density of the universe which gets reheated when the moduli decay. Since the moduli are gravitationally coupled, they tend to decay very late with a reheating temperature $T_{\rm rh} \sim \sqrt{\Gamma M_P} \sim m_{\rm mod}\sqrt{m_{\rm mod}/M_P}$, where Γ is the decay width of the modulus and $m_{\rm mod}$ is the mass of the moduli. $T_{\rm rh}$ needs to be larger than $T_{\rm BBN}$ in order to maintain the successful BBN predictions.

If we use the NFWc profile, we can constrain the reheat temperature ($T_{\rm rh} > 0.5$ GeV) for a dark matter mass ~ 100 GeV (with the freeze-out temperature, $T_{\rm f} \sim 5$ GeV) to charged lepton final states for MSSM parameter space. The constraint on $T_{\rm rh}$ is model dependent since the dark matter annihilation calculation not only depends on the mass scales of dark matter, mediator, and final states but also on the couplings. In the case of the MSSM, the coupling is $g_{\rm weak}$. This can be different for other models leading to larger annihilation cross-sections and a reduced $T_{\rm rh}$ lower limit.

In a non-thermal scenario, the dark matter abundance is given by the expression [188, 189]

$$\left(\frac{n_\chi}{s}\right) = \min\left\{\left(\frac{n_\chi}{s}\right)^{\rm obs} \frac{\langle\sigma v\rangle^{\rm th}}{\langle\sigma v\rangle}\sqrt{\frac{g_*(T_{\rm f})}{g_*(T_{\rm rh})}}\frac{T_{\rm f}}{T_{\rm rh}}, \quad Y_\phi {\rm Br}_\phi\right\}, \tag{4.17}$$

$(n_\chi/s)^{\rm obs} \simeq \Omega^{\rm obs}\,(\rho_{\rm crit}/m_\chi s h^2)$, while $Y_\phi \simeq 3T_{\rm rh}/4m_\phi$ is the yield of dark matter abundance from modulus decay, and ${\rm Br}_\phi$ is the branching ratio of the modulus decay into R-parity odd particles. The first term refers to the annihilation scenario, while the second term refers to the branching Scenario. In the branching scenario, the dark matter is frozen-in, and the value of the cross-section is only bounded from above. In

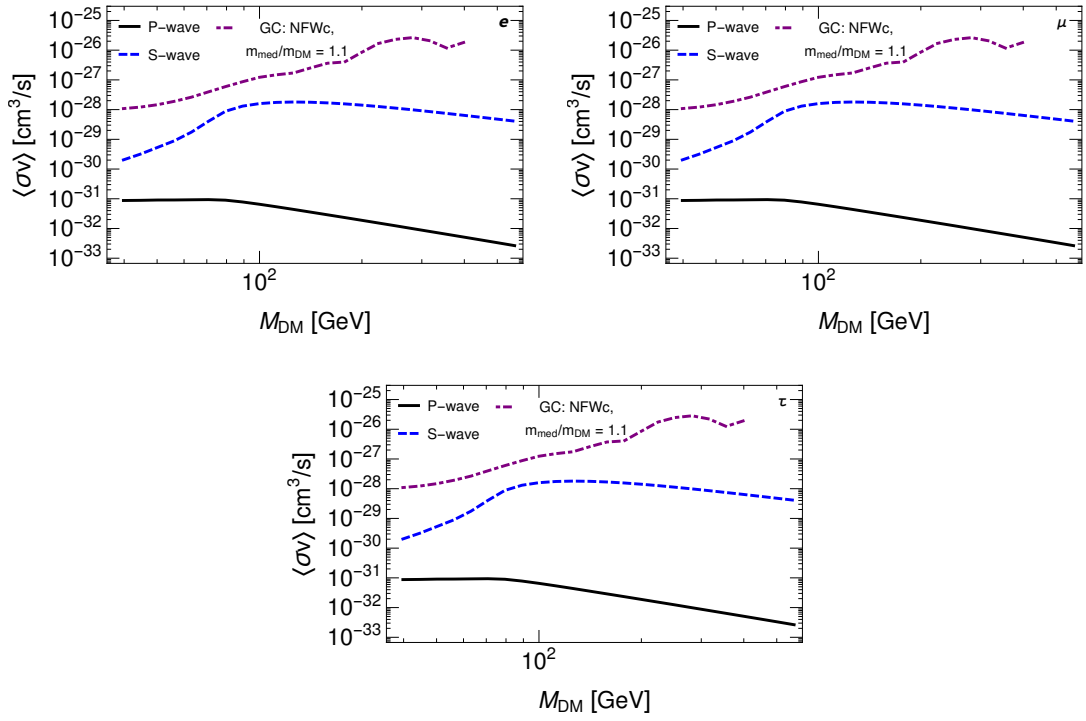

Figure 4.10: Comparison between s- and p-wave galactic virial velocity cross-sections with galactic center constraints. Upper bound constraints imposed by the galactic center (long-short dashed) and the theoretical calculated cross-section for various final states which satisfy the thermal dark matter abundance. The dashed lines show the s-wave and the solid lines show the p-wave component today. Reprinted with permission from Ref. [87].

Figure 4.9, the annihilation scenarios are constrained.

In Figure 4.11, we compare the dSph and diffuse gamma-ray constraints for e^+e^-, $\mu^+\mu^-$, $\tau^+\tau^-$, and $\nu\nu$ final states in conjunction with a final state gauge boson. Generally across the entire mass range, we find that the constraints from diffuse gamma-ray data are more stringent than those from dSphs.

The constraints we find can be compared to those previous found in Ref. [85], which uses a similar approach. At $m_{\rm DM} \sim 90$ GeV, there is a slope change that is present in all cases. This is a direct result of W/Z boson channels becoming dominant pathways. The remaining differences between our results and Ref. [85] may be attributed to binning resolution for the data and the model.

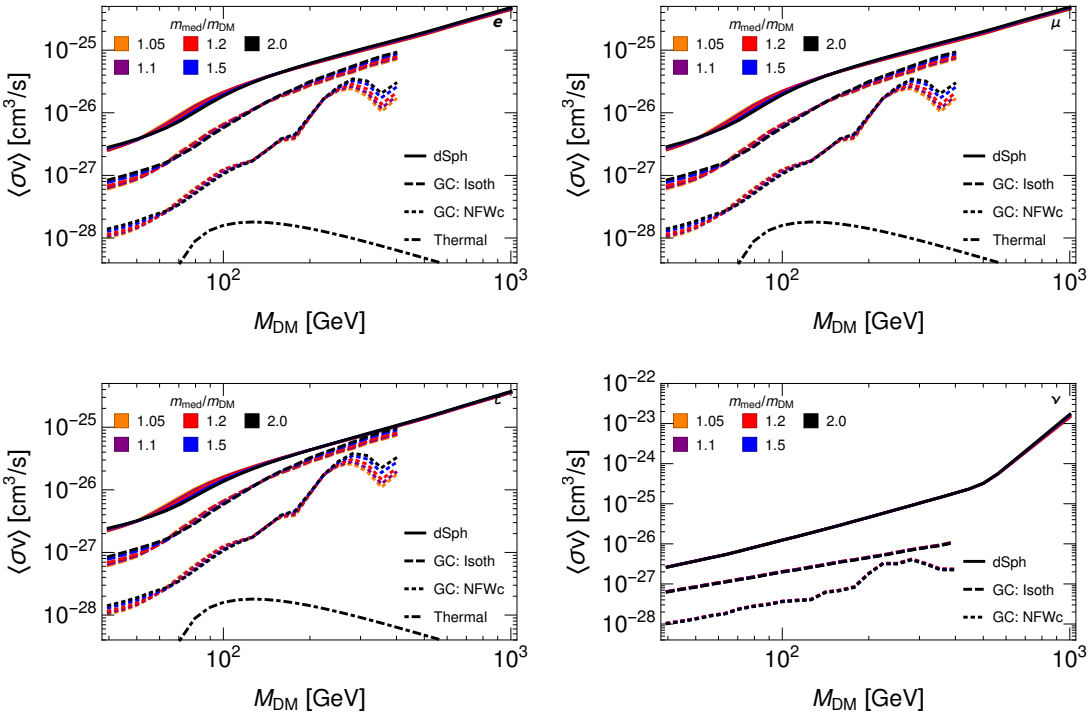

Figure 4.11: Gauge boson bremsstrahlung constraints from the galactic center and dSph with thermal relic predictions. Upper bound constraints imposed by dSph (solid), the galactic center (dashed) and the theoretical calculated cross-section for thermal dark matter (long-short dashed) for various mediator mass ratios, $m_{\rm med}/m_{\rm DM}$. Lepton final states are electron (top left), muon (top right), tau (bottom left), and neutrino (bottom right). We also show the galactic center using a less conservative dark matter profile (short dashed). Reprinted with permission from Ref. [87].

We show 21 cm estimate constraints for the p-wave dominated model in Figure 4.12. We also compare the 21 cm and diffuse constraints for $f\bar{f} + \gamma/W/Z$ and find that the galactic center constraint from Fermi are currently much more constraining than 21 cm observations. In contrast to the diffuse constraints, the $\bar{\nu}\nu\gamma$ final state is constrained at about the same level as the other leptonic final states, rather than providing the most stringent bounds. Although there are currently a few orders of magnitude separating the 21 cm and diffuse bounds, there are upcoming 21 cm observations which can increase the competitiveness of this method, thus providing a useful tool from a different cosmic epoch in the investigation of p-wave models.

The cosmic microwave background (CMB) is an additional method to be considered. Figure 4.13 compares the 21 cm results to those of the CMB. The current 21 cm results are comparable to the CMB with the CMB being slightly stronger by approximately a factor of 5. However, they are both much weaker than both the dSph and diffuse constraints.

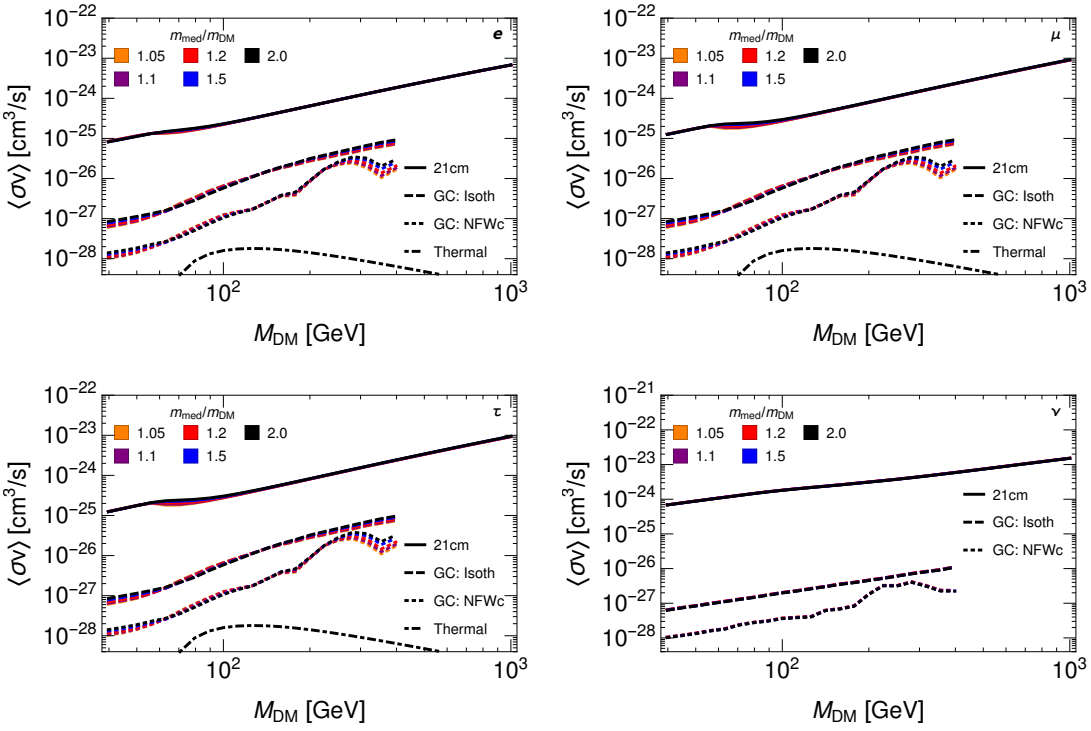

Figure 4.12: Gauge boson bremsstrahlung constraints from the galactic center and 21 cm with thermal relic predictions. Upper bound constraints imposed by 21 cm with $\Delta T = -100$ mK (solid), the galactic center (dashed) and the theoretical calculated cross-section for thermal dark matter (long-short dashed) for various mediator mass ratios, $m_{\rm med}/m_{\rm DM}$. Lepton final states are electron (top left), muon (top right), tau (bottom left), and neutrino (bottom right). We also show the galactic center using a less conservative dark matter profile (short dashed). Reprinted with permission from Ref. [87].

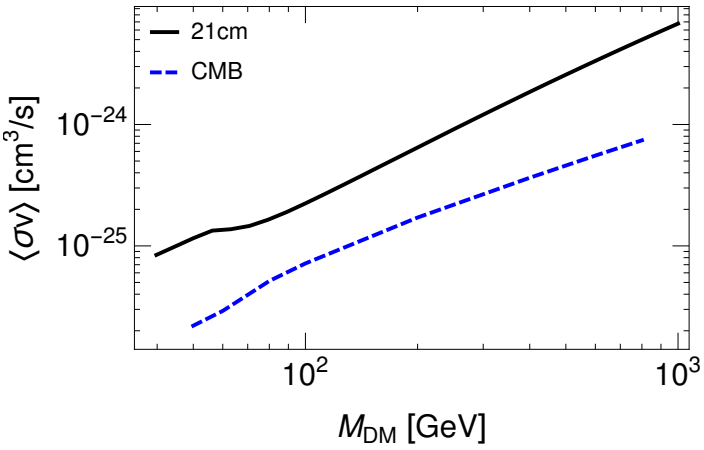

Figure 4.13: Comparison between 21 cm and CMB constraints on annihilation through boson bremsstrahlung. While the CMB (dashed) is more constraining than the 21 cm (solid), it is still much weaker than both GC and dSph. The data set used in the comparison is annihilation to electrons plus a boson with mediator mass ratio 1.1. Reprinted with permission from Ref. [87].

5. CONCLUSION*

We studied multiple indirect detection methods of dark matter including CMB anisotropy, 21 cm absorption, and diffuse and targeted spectral signatures. We connected these methods with available experimental data. We applied these methods to multiple models including decaying, PBHs, annihilations into two and four-bodies, and bremsstrahlung boson emitting annihilations and provide constraints on their parameter spaces.

CMB anisotropies and 21 cm absorption signatures rely upon the history of the Universe. Dark matter candidate interaction inject energy into the Universe thus altering its evolution and change the nature of these two measurements. The key focus of their interactions is an investigation into the absorption's effective efficiencies and alterations to the ionization fraction and gas temperature. We also focused on the alterations to the CMB and 21 cm line as a result of these injections. For our CMB bound, we model the energy absorption not as instantaneous, but rather using redshift dependent efficiency. The energy injection results in an increase in the ionization fraction at late times as well as an increase in the IGM temperature, leading to distortions of the CMB anisotropies. Larger fractional changes occur at large multipoles because of the increase of the width of the last scattering surface. As far as the 21 cm

*Parts of this section are reprinted with permission from:

S. Clark, B. Dutta, Y. Gao, L. E. Strigari, and S. Watson, "Planck Constraint on Relic Primordial Black Holes," *Phys. Rev.* **D95** no. 8, (2017) 083006, arXiv:1612.07738 [astro-ph.CO]. © 2017 American Physical Society

S. J. Clark, B. Dutta, and L. E. Strigari, "Dark Matter Annihilation into Four-Body Final States and Implications for the AMS Antiproton Excess," *Phys. Rev.* **D97** no. 2, (2018) 023003, arXiv:1709.07410 [astro-ph.HE]. © 2018 American Physical Society

S. Clark, B. Dutta, Y. Gao, Y.-Z. Ma, and L. E. Strigari, "21 cm limits on decaying dark matter and primordial black holes," *Phys. Rev.* **D98** no. 4, (2018) 043006, arXiv:1803.09390 [astro-ph.HE]. © 2018 American Physical Society

S. J. Clark, J. B. Dent, B. Dutta, and L. E. Strigari, "Indirect detection of the partial p wave via the s wave in the annihilation cross section of dark matter," *Phys. Rev.* **D99** no. 8, (2019) 083003, arXiv:1901.01454 [hep-ph]. Published by the American Physical Society.

anomaly measured by EDGES, we do not attempt to explain it, but use the experimental error to provide estimations to constraints. We also reviewed spectral detection techniques and incorporated them into measuring multiple types of signals including diffuse gamma-ray emission from the galaxy and the galactic center, gamma-ray source searches from satellite dwarf spheroidal galaxies, and galactic antiproton excess signals.

We considered dark matter decay channels $DM \to e^+e^-, \gamma\gamma, \mu^+\mu^-, \tau^+\tau^-, b\bar{b}$ and obtained $\tau_{\rm DM} \geq 10^{26-27}$s bounds on the dark matter lifetime by requiring the heating process raises the gas temperature to no higher than -100 mK or -50 mK. For e^+e^-, $\gamma\gamma$ final states, the 21 cm observation provides the best bound in the dark matter mass-lifetime parameter space. For $b\bar{b}$ and $\mu^+\mu^-$ final states, the 21 cm observation bound becomes better than all the existing constraint for $m_{\rm DM} < 30$ GeV. For $\tau^+\tau^-$ final states, constraints are similar for $m_{\rm DM} \approx 10$ GeV. The 21 cm bound is found to be better than current CMB damping constraint from *Planck* data.

Since the removal of extremely large foreground from the data is difficult, the EDGES result needs to be verified by future 21 cm experiments like PRIZM, HERA, LEDA, and SKA. If the absorption signal is verified in the future, the 21 cm absorption can prove to be a powerful probe to non-standard heating processes. It is worth emphasizing on the 21 cm's sensitivity to $e^{\pm}, \gamma$ injections in the sub-GeV energy range as demonstrated in Figure 4.1. In contrast to the poor absorption efficiency at TeV or higher energy scale, the sub-GeV bound on decaying dark matter can nicely fill in the MeV-GeV range where the indirect search bounds are current less stringent in comparison to X-ray and hard gamma-ray limits.

PBHs are of great interest in cosmology. They reveal conditions in the early universe and can serve as a dark matter candidate. There are several standard mechanisms that have been proposed to detect PBHs; these include detection of Hawking radiation, detection of radiation produced from accretion disks, and gravitational lensing. Each method is capable of targeting different PBH mass ranges. In this work, we have

focused on PBHs with masses in the range $10^{15} - 10^{17}$ g. We have improved and made more precise the constraints in this mass range using the CMB and 21 cm. We also looked at EGB and spectral distortion considerations.

Using *Planck* data, we show that CMB distortions from Hawking radiation allow for stringent constraints on the density of $10^{15} - 10^{17}$ g PBHs of $\Omega_{\rm BH} \lesssim 3.3 \times 10^{-9}(m_{\rm BH}/M_\star)^{3.8}$. We show that for mass $\sim 10^{15} - 10^{16}$ g, the CMB constraints are stronger than the constraints from the $\sim 1 - 30$ MeV EGB, which imply, $\Omega_{\rm BH} \lesssim 1.4 \times 10^{-8}(m_{\rm BH}/M_\star)^{3.2}$. Constraints imposed by CMB spectral distortions from Hawking radiation producing sub 10.2 eV photons are also much weaker than our constraint. Constraints with 21 cm further strengthen the PBH constraints by an order of magnitude over CMB *Planck* results.

In the future, our theoretical analysis may be improved by including a mass spectrum of PBHs. In addition, even though we have used the EGB to bound the contribution of PBHs, it may be interesting to consider the EGB as a signal of PBHs. This is an exciting possibility because the origin of this $\sim$ MeV gamma-ray background is not yet known [190–192]. Future missions to measure MeV gamma-rays will be especially important for the study of PBHs [193].

We have examined experimental constraints on general four-body dark matter annihilation models, in which the final state Standard Model particles are produced through an unstable mediator. We compare these constraints on the annihilation cross-section to previously reported constraints on two-body decay models, and find that the current gamma-ray and *Planck* data is sufficient to strongly constrain four-body final state models over a large range of interesting parameter space. For most cases considered, we show Fermi-LAT, MAGIC, and VERITAS limits are weaker in the four-body than the two-body channel. This occurs because a larger fraction of photons are produced below the detection threshold of these experiments in the four-body channel. On the other hand, the *Planck* constraints on four-body models are nearly identical to those

on two-body models over a large range of dark matter masses. This is because CMB measurements are relatively insensitive to the shape of the energy spectrum of the decay products.

We have examined the implications of these four-body models in the context of recent AMS antiproton data, finding a sensitivity to the mediator mass not observed in current gamma-ray experiments. We have identified a particular scenario with dark matter mass $\sim 60 - 100$ GeV, and mediator mass $\sim m_\phi/m_\chi \lesssim 1$ in which four-body decay models are able to explain the AMS data. We also find that this regime is consistent with the Fermi-LAT galactic center excess. As a general result, we highlight that including light mediators allows for a plausible dark matter interpretation of the gamma-ray and antiproton data in a larger range of parameter space relative to two-body models.

We further look at an important extension to dark matter annihilation scenarios through bremsstrahlung boson emission. For if dark matter self-annihilates to Standard Model final states, its dominant annihilation channel can vary over the course of cosmic history due to a velocity dependence. This will dramatically suppress p-wave annihilations relative to s-wave for non-relativistic dark matter. If dark matter were to annihilate dominantly through a p-wave process, it will be observationally very challenging to probe with standard indirect detection techniques. We have investigated well-motivated models which annihilate dominantly via a p-wave process to two-body final states in the very early universe, but can have a leading three-body final state annihilation when the dark matter is non-relativistic. The cross-section is enhanced by the well known mechanism of internal and final state vector boson bremsstrahlung of $W/Z/\gamma$, leading to $f\bar{f} + W/Z/\gamma$ final states.

The model framework we have adopted is a rather general, SUSY-inspired model with Majorana dark matter of mass $m_{\rm DM}$ annihilating via t- and u-channel exchange of charged mediators of mass $m_{\rm med}$. Annihilation to three-body final states is enhanced

as the mediator mass approaches that of the dark matter. We have included the dependence of this ratio in our analysis. We find that the bounds are fairly insensitive to $m_{\rm med}/m_{\rm DM}$ as it is varied from 1.05 to 2.0. We have employed complementary aspects of the different final state bosons in order to strengthen the bounds on dark matter annihilation. Specifically, the photon bremsstrahlung can produce line-like features which can be constrained with data from the Fermi satellite via well-known line search techniques. As the dark matter mass is increased, the massive W and Z bosons become kinematically available, providing complementary signals to the photon line search through the addition of a continuum spectrum produced by the W and Z decays.

Some aspects of this work to highlight are the use of recent 21 cm observations to constrain annihilations with vector bremsstrahlung, and the development of constraints using the $\bar{\nu}\nu\gamma$ final state. Developing bounds on dark matter physics from 21 cm observations are quickly becoming a standard tool in the field, though the limits derived in the current work are significantly weaker than those from dSph and diffuse data from the Fermi satellite searches. Final states consisting of neutrinos accompanied by no other particles, or dominantly annihilating to neutrinos without the existence of charged lepton final state channels, lead to a very difficult search. However, we have demonstrated that in some dark matter models, $\bar{\nu}\nu\gamma$ final states can actually provide leading constraints compared to those from charged leptons, $\ell^+\ell^-\gamma$, from diffuse and dSph searches, with the 21 cm observations for $\bar{\nu}\nu\gamma$ final states producing bounds competitive with those from $\ell^+\ell^-\gamma$.

Although models of dark matter dominantly annihilating to two-body final states through p-wave processes are quite challenging to probe observationally, we see that the situation is not hopeless. We found that some dark matter masses are constrained while for non-thermal scenarios the reheating temperature $T_{\rm rh}$ gets constrained. By investigating scenarios where three-body final states open s-wave channels, p-wave

models can still provide a fertile ground for current and future investigations.

REFERENCES

[1] **Planck** Collaboration, P. A. R. Ade *et al.*, "Planck 2015 results. XIII. Cosmological parameters," *Astron. Astrophys.* **594** (2016) A13, arXiv:1502.01589 [astro-ph.CO].

[2] J. D. Bowman, A. E. E. Rogers, R. A. Monsalve, T. J. Mozdzen, and N. Mahesh, "An absorption profile centred at 78 megahertz in the sky-averaged spectrum," *Nature* **555** no. 7694, (2018) 67–70.

[3] R. Barkana, "Possible interaction between baryons and dark-matter particles revealed by the first stars," *Nature* **555** no. 7694, (2018) 71–74.

[4] A. Geringer-Sameth and S. M. Koushiappas, "Exclusion of canonical WIMPs by the joint analysis of Milky Way dwarfs with Fermi," *Phys. Rev. Lett.* **107** (2011) 241303, arXiv:1108.2914 [astro-ph.CO].

[5] **Fermi-LAT** Collaboration, M. Ackermann *et al.*, "Constraining Dark Matter Models from a Combined Analysis of Milky Way Satellites with the Fermi Large Area Telescope," *Phys. Rev. Lett.* **107** (2011) 241302, arXiv:1108.3546 [astro-ph.HE].

[6] **Fermi-LAT** Collaboration, M. Ackermann *et al.*, "Dark matter constraints from observations of 25 Milky Way satellite galaxies with the Fermi Large Area Telescope," *Phys. Rev.* **D89** (2014) 042001, arXiv:1310.0828 [astro-ph.HE].

[7] A. Geringer-Sameth, S. M. Koushiappas, and M. G. Walker, "Comprehensive search for dark matter annihilation in dwarf galaxies," *Phys. Rev.* **D91** no. 8, (2015) 083535, arXiv:1410.2242 [astro-ph.CO].

[8] **Fermi-LAT** Collaboration, M. Ackermann *et al.*, "Searching for Dark Matter Annihilation from Milky Way Dwarf Spheroidal Galaxies with Six Years of Fermi Large Area Telescope Data," *Phys. Rev. Lett.* **115** no. 23, (2015) 231301, arXiv:1503.02641 [astro-ph.HE].

[9] N. Padmanabhan and D. P. Finkbeiner, "Detecting dark matter annihilation with CMB polarization: Signatures and experimental prospects," *Phys. Rev.* **D72** (2005) 023508, arXiv:astro-ph/0503486 [astro-ph].

[10] S. Galli, F. Iocco, G. Bertone, and A. Melchiorri, "CMB constraints on Dark Matter models with large annihilation cross-section," *Phys. Rev.* **D80** (2009) 023505, arXiv:0905.0003 [astro-ph.CO].

[11] T. R. Slatyer, N. Padmanabhan, and D. P. Finkbeiner, "CMB Constraints on WIMP Annihilation: Energy Absorption During the Recombination Epoch," *Phys. Rev.* **D80** (2009) 043526, arXiv:0906.1197 [astro-ph.CO].

[12] S. Galli, F. Iocco, G. Bertone, and A. Melchiorri, "Updated CMB constraints on Dark Matter annihilation cross-sections," *Phys. Rev.* **D84** (2011) 027302, arXiv:1106.1528 [astro-ph.CO].

[13] D. P. Finkbeiner, S. Galli, T. Lin, and T. R. Slatyer, "Searching for Dark Matter in the CMB: A Compact Parameterization of Energy Injection from New Physics," *Phys. Rev.* **D85** (2012) 043522, arXiv:1109.6322 [astro-ph.CO].

[14] T. R. Slatyer, "Energy Injection And Absorption In The Cosmic Dark Ages," *Phys. Rev.* **D87** no. 12, (2013) 123513, arXiv:1211.0283 [astro-ph.CO].

[15] S. Galli, T. R. Slatyer, M. Valdes, and F. Iocco, "Systematic Uncertainties In Constraining Dark Matter Annihilation From The Cosmic Microwave Background," *Phys. Rev.* **D88** (2013) 063502, arXiv:1306.0563 [astro-ph.CO].

[16] M. S. Madhavacheril, N. Sehgal, and T. R. Slatyer, "Current Dark Matter Annihilation Constraints from CMB and Low-Redshift Data," *Phys. Rev.* **D89** (2014) 103508, arXiv:1310.3815 [astro-ph.CO].

[17] Y. Ali-Haimoud and C. M. Hirata, "HyRec: A fast and highly accurate primordial hydrogen and helium recombination code," *Phys. Rev.* **D83** (2011) 043513, arXiv:1011.3758 [astro-ph.CO].

[18] K. M. Belotsky and A. A. Kirillov, "Primordial black holes with mass $10^{16} - 10^{17}$ g and reionization of the Universe," *JCAP* **1501** no. 01, (2015) 041, arXiv:1409.8601 [astro-ph.CO].

[19] H. Liu, T. R. Slatyer, and J. Zavala, "Contributions to cosmic reionization from dark matter annihilation and decay," *Phys. Rev.* **D94** no. 6, (2016) 063507, arXiv:1604.02457 [astro-ph.CO].

[20] P. J. E. Peebles, "Recombination of the Primeval Plasma," *Astrophys. J.* **153** (1968) 1.

[21] T. R. Slatyer, "Indirect Dark Matter Signatures in the Cosmic Dark Ages II. Ionization, Heating and Photon Production from Arbitrary Energy Injections," *Phys. Rev.* **D93** no. 2, (2016) 023521, arXiv:1506.03812 [astro-ph.CO].

[22] T. R. Slatyer, "Indirect dark matter signatures in the cosmic dark ages. I. Generalizing the bound on s-wave dark matter annihilation from Planck results," *Phys. Rev.* **D93** no. 2, (2016) 023527, arXiv:1506.03811 [hep-ph].

[23] S. Clark, B. Dutta, Y. Gao, L. E. Strigari, and S. Watson, "Planck Constraint on Relic Primordial Black Holes," *Phys. Rev.* **D95** no. 8, (2017) 083006, arXiv:1612.07738 [astro-ph.CO].

[24] T. Sjostrand, S. Mrenna, and P. Z. Skands, "PYTHIA 6.4 Physics and Manual," *JHEP* **05** (2006) 026, arXiv:hep-ph/0603175 [hep-ph].

[25] T. Sjostrand, S. Mrenna, and P. Z. Skands, "A Brief Introduction to PYTHIA 8.1," *Comput. Phys. Commun.* **178** (2008) 852–867, arXiv:0710.3820 [hep-ph].

[26] M. Cirelli, G. Corcella, A. Hektor, G. Hutsi, M. Kadastik, P. Panci, M. Raidal, F. Sala, and A. Strumia, "PPPC 4 DM ID: A Poor Particle Physicist Cookbook for Dark Matter Indirect Detection," *JCAP* **1103** (2011) 051, arXiv:1012.4515 [hep-ph]. [Erratum: JCAP1210,E01(2012)].

[27] P. Ciafaloni, D. Comelli, A. Riotto, F. Sala, A. Strumia, and A. Urbano, "Weak Corrections are Relevant for Dark Matter Indirect Detection," *JCAP* **1103** (2011) 019, arXiv:1009.0224 [hep-ph].

[28] S. J. Clark, B. Dutta, and L. E. Strigari, "Dark Matter Annihilation into Four-Body Final States and Implications for the AMS Antiproton Excess," *Phys. Rev.* **D97** no. 2, (2018) 023003, arXiv:1709.07410 [astro-ph.HE].

[29] J. S. Bolton, G. D. Becker, S. Raskutti, J. S. B. Wyithe, M. G. Haehnelt, and W. L. W. Sargent, "Improved measurements of the intergalactic medium temperature around quasars: possible evidence for the initial stages of He-II reionisation at z 6," arXiv:1110.0539 [astro-ph.CO].

[30] J. S. Bolton, G. D. Becker, J. S. B. Wyithe, M. G. Haehnelt, and W. L. W. Sargent, "A first direct measurement of the intergalactic medium temperature around a quasar at z=6," *Mon. Not. Roy. Astron. Soc.* **406** (2010) 612, arXiv:1001.3415 [astro-ph.CO].

[31] M. A. Schenker, R. S. Ellis, N. P. Konidaris, and D. P. Stark, "Line Emitting Galaxies Beyond a Redshift of 7: An Improved Method for Estimating the Evolving Neutrality of the Intergalactic Medium," *Astrophys. J.* **795** no. 1, (2014) 20, arXiv:1404.4632 [astro-ph.CO].

[32] **Planck** Collaboration, N. Aghanim *et al.*, "Planck 2015 results. XI. CMB power spectra, likelihoods, and robustness of parameters," *Astron. Astrophys.* **594** (2016) A11, arXiv:1507.02704 [astro-ph.CO].

[33] T. R. Slatyer and C.-L. Wu, "General Constraints on Dark Matter Decay from the Cosmic Microwave Background," *Phys. Rev.* **D95** no. 2, (2017) 023010, arXiv:1610.06933 [astro-ph.CO].

[34] A. Lewis, A. Challinor, and A. Lasenby, "Efficient computation of CMB anisotropies in closed FRW models," *Astrophys. J.* **538** (2000) 473–476, arXiv:astro-ph/9911177 [astro-ph].

[35] C. Howlett, A. Lewis, A. Hall, and A. Challinor, "CMB power spectrum parameter degeneracies in the era of precision cosmology," *JCAP* **1204** (2012) 027, arXiv:1201.3654 [astro-ph.CO].

[36] A. Lewis and S. Bridle, "Cosmological parameters from CMB and other data: A Monte Carlo approach," *Phys. Rev.* **D66** (2002) 103511, arXiv:astro-ph/0205436 [astro-ph].

[37] A. Lewis, "Efficient sampling of fast and slow cosmological parameters," *Phys. Rev.* **D87** no. 10, (2013) 103529, arXiv:1304.4473 [astro-ph.CO].

[38] **Planck** Collaboration, P. A. R. Ade *et al.*, "Planck 2013 results. XVI. Cosmological parameters," *Astron. Astrophys.* **571** (2014) A16, arXiv:1303.5076 [astro-ph.CO].

[39] S. Furlanetto, S. P. Oh, and F. Briggs, "Cosmology at Low Frequencies: The 21 cm Transition and the High-Redshift Universe," *Phys. Rept.* **433** (2006) 181–301, arXiv:astro-ph/0608032 [astro-ph].

[40] J. R. Pritchard and A. Loeb, "21-cm cosmology," *Rept. Prog. Phys.* **75** (2012) 086901, arXiv:1109.6012 [astro-ph.CO].

[41] S. A. Wouthuysen, "On the excitation mechanism of the 21-cm (radiofrequency) interstellar hydrogen emission line," *Astron.J.* **57** (1952) 31–32.

[42] G. B. Field, "Excitation of the hydrogen 21-cm line," *Proc.Ire.* **46** (1958) 240–250.

[43] A. Fialkov, R. Barkana, and A. Cohen, "Constraining Baryon–Dark Matter Scattering with the Cosmic Dawn 21-cm Signal," *Phys. Rev. Lett.* **121** (2018) 011101, arXiv:1802.10577 [astro-ph.CO].

[44] A. Berlin, D. Hooper, G. Krnjaic, and S. D. McDermott, "Severely Constraining Dark Matter Interpretations of the 21-cm Anomaly," *Phys. Rev. Lett.* **121** no. 1, (2018) 011102, arXiv:1803.02804 [hep-ph].

[45] R. Barkana, N. J. Outmezguine, D. Redigolo, and T. Volansky, "Strong constraints on light dark matter interpretation of the EDGES signal," *Phys. Rev.* **D98** no. 10, (2018) 103005, arXiv:1803.03091 [hep-ph].

[46] J. B. Muñoz and A. Loeb, "A small amount of mini-charged dark matter could cool the baryons in the early Universe," *Nature* **557** no. 7707, (2018) 684, arXiv:1802.10094 [astro-ph.CO].

[47] S. Fraser *et al.*, "The EDGES 21 cm Anomaly and Properties of Dark Matter," *Phys. Lett.* **B785** (2018) 159–164, arXiv:1803.03245 [hep-ph].

[48] Z. Kang, "Post-recombination Dark Matter for the 21-cm Signal," arXiv:1803.04928 [hep-ph].

[49] T. R. Slatyer and C.-L. Wu, "Early-Universe constraints on dark matter-baryon scattering and their implications for a global 21 cm signal," *Phys. Rev.* **D98** no. 2, (2018) 023013, arXiv:1803.09734 [astro-ph.CO].

[50] S. Hirano and V. Bromm, "Baryon-dark matter scattering and first star formation," *Mon. Not. Roy. Astron. Soc.* **480** no. 1, (2018) L85–L89, arXiv:1803.10671 [astro-ph.GA].

[51] M. S. Mahdawi and G. R. Farrar, "Constraints on Dark Matter with a moderately large and velocity-dependent DM-nucleon cross-section," *JCAP* **1810** no. 10, (2018) 007, arXiv:1804.03073 [hep-ph].

[52] G. D'Amico, P. Panci, and A. Strumia, "Bounds on Dark Matter annihilations from 21 cm data," *Phys. Rev. Lett.* **121** no. 1, (2018) 011103, arXiv:1803.03629 [astro-ph.CO].

[53] Y. Yang, "Contributions of dark matter annihilation to the global 21 cm spectrum observed by the EDGES experiment," *Phys. Rev.* **D98** no. 10, (2018) 103503, arXiv:1803.05803 [astro-ph.CO].

[54] K. Cheung, J.-L. Kuo, K.-W. Ng, and Y.-L. S. Tsai, "The impact of EDGES 21-cm data on dark matter interactions," *Phys. Lett.* **B789** (2019) 137–144, arXiv:1803.09398 [astro-ph.CO].

[55] H. Liu and T. R. Slatyer, "Implications of a 21-cm signal for dark matter annihilation and decay," *Phys. Rev.* **D98** no. 2, (2018) 023501, arXiv:1803.09739 [astro-ph.CO].

[56] S. Clark, B. Dutta, Y. Gao, Y.-Z. Ma, and L. E. Strigari, "21 cm limits on decaying dark matter and primordial black holes," *Phys. Rev.* **D98** no. 4, (2018) 043006, arXiv:1803.09390 [astro-ph.HE].

[57] A. Mitridate and A. Podo, "Bounds on Dark Matter decay from 21 cm line," *JCAP* **1805** no. 05, (2018) 069, arXiv:1803.11169 [hep-ph].

[58] A. Hektor, G. Hütsi, L. Marzola, M. Raidal, V. Vaskonen, and H. Veermäe, "Constraining Primordial Black Holes with the EDGES 21-cm Absorption Signal," *Phys. Rev.* **D98** no. 2, (2018) 023503, arXiv:1803.09697 [astro-ph.CO].

[59] A. Lidz and L. Hui, "Implications of a prereionization 21-cm absorption signal for fuzzy dark matter," *Phys. Rev.* **D98** no. 2, (2018) 023011, arXiv:1805.01253 [astro-ph.CO].

[60] A. A. Costa, R. C. G. Landim, B. Wang, and E. Abdalla, "Interacting Dark Energy: Possible Explanation for 21-cm Absorption at Cosmic Dawn," *Eur. Phys. J.* **C78** no. 9, (2018) 746, arXiv:1803.06944 [astro-ph.CO].

[61] M. Pospelov, J. Pradler, J. T. Ruderman, and A. Urbano, "Room for New Physics in the Rayleigh-Jeans Tail of the Cosmic Microwave Background," *Phys. Rev. Lett.* **121** no. 3, (2018) 031103, arXiv:1803.07048 [hep-ph].

[62] C. Li and Y.-F. Cai, "Searching for the Dark Force with 21-cm Spectrum in Light of EDGES," *Phys. Lett.* **B788** (2019) 70–75, arXiv:1804.04816 [astro-ph.CO].

[63] L.-B. Jia, "Dark photon portal dark matter with the 21-cm anomaly," *Eur. Phys. J.* **C79** no. 1, (2019) 80, arXiv:1804.07934 [hep-ph].

[64] M. Safarzadeh, E. Scannapieco, and A. Babul, "A limit on the warm dark matter particle mass from the redshifted 21 cm absorption line," *Astrophys. J.* **859** no. 2, (2018) L18, arXiv:1803.08039 [astro-ph.CO].

[65] G. Lambiase and S. Mohanty, "The 21-cm axion," arXiv:1804.05318 [hep-ph].

[66] K. Lawson and A. R. Zhitnitsky, "The 21 cm absorption line and the axion quark nugget dark matter model," *Phys. Dark Univ.* (2018) 100295, arXiv:1804.07340 [hep-ph]. [Phys. Dark Univ.100295,2019(2018)].

[67] T. Moroi, K. Nakayama, and Y. Tang, "Axion-photon conversion and effects on 21 cm observation," *Phys. Lett.* **B783** (2018) 301–305, arXiv:1804.10378 [hep-ph].

[68] A. Schneider, "Constraining noncold dark matter models with the global 21-cm signal," *Phys. Rev.* **D98** no. 6, (2018) 063021, arXiv:1805.00021 [astro-ph.CO].

[69] P. Sikivie, "Axion dark matter and the 21-cm signal," *Phys. Dark Univ.* (2018) 100289, arXiv:1805.05577 [astro-ph.CO].

[70] L. Zhang, X.-L. Chen, Y.-A. Lei, and Z.-G. Si, "The impacts of dark matter particle annihilation on recombination and the anisotropies of the cosmic microwave background," *Phys. Rev.* **D74** (2006) 103519, arXiv:astro-ph/0603425 [astro-ph].

[71] E. Ripamonti, M. Mapelli, and A. Ferrara, "The impact of dark matter decays and annihilations on the formation of the first structures," *Mon. Not. Roy. Astron. Soc.* **375** (2007) 1399–1408, arXiv:astro-ph/0606483 [astro-ph].

[72] S. R. Furlanetto, S. P. Oh, and E. Pierpaoli, "The Effects of Dark Matter Decay and Annihilation on the High-Redshift 21 cm Background," *Phys. Rev.* **D74** (2006) 103502, arXiv:astro-ph/0608385 [astro-ph].

[73] M. Zaldarriaga, S. R. Furlanetto, and L. Hernquist, "21 Centimeter fluctuations from cosmic gas at high redshifts," *Astrophys. J.* **608** (2004) 622–635, arXiv:astro-ph/0311514 [astro-ph].

[74] C. M. Hirata, "Wouthuysen-Field coupling strength and application to high-redshift 21 cm radiation," *Mon. Not. Roy. Astron. Soc.* **367** (2006) 259–274, arXiv:astro-ph/0507102 [astro-ph].

[75] P. C. Breysse, Y. Ali-Haïmoud, and C. M. Hirata, "Ultimate frontier of 21-cm cosmology," *Phys. Rev.* **D98** no. 4, (2018) 043520, arXiv:1804.10626 [astro-ph.CO].

[76] A. Cohen, A. Fialkov, R. Barkana, and M. Lotem, "Charting the Parameter Space of the Global 21-cm Signal," *Mon. Not. Roy. Astron. Soc.* **472** no. 2, (2017) 1915–1931, arXiv:1609.02312 [astro-ph.CO].

[77] J. Mirocha and S. R. Furlanetto, "What does the first highly-redshifted 21-cm detection tell us about early galaxies?," *Mon. Not. Roy. Astron. Soc.* **483** no. 2, (2019) 1980–1992, arXiv:1803.03272 [astro-ph.GA].

[78] J. B. Peterson, T. C. Voytek, A. Natarajan, J. M. J. Garcia, and O. Lopez-Cruz, "Measuring the 21 cm Global Brightness Temperature Spectrum During the Dark Ages with the SCI-HI Experiment," in *Proceedings, 49th Rencontres de Moriond on Cosmology: La Thuile, Italy, March 15-22, 2014*, pp. 129–134. 2014. arXiv:1409.2774 [astro-ph.IM]. http://inspirehep.net/record/1315669/files/arXiv:1409.2774.pdf.

[79] D. R. DeBoer *et al.*, "Hydrogen Epoch of Reionization Array (HERA)," *Publ. Astron. Soc. Pac.* **129** (2017) 045001, arXiv:1606.07473 [astro-ph.IM].

[80] D. C. Price, L. J. Greenhill, A. Fialkov, G. Bernardi, H. Garsden, B. R. Barsdell, J. Kocz, M. M. Anderson, S. A. Bourke, J. Craig, M. R. Dexter, J. Dowell, M. W. Eastwood, T. Eftekhari, S. W. Ellingson, G. Hallinan, J. M. Hartman, R. Kimberk, T. J. W. Lazio, S. Leiker, D. MacMahon, R. Monroe, F. Schinzel, G. B. Taylor, D. Werthimer, and D. P. Woody, "Design and characterization of the Large-Aperture Experiment to Detect the Dark Age (LEDA) radiometer systems," *ArXiv e-prints* (Sept., 2017) , arXiv:1709.09313 [astro-ph.IM].

[81] **Cosmology-SWG, EoR/CD-SWG** Collaboration, J. Pritchard *et al.*, "Cosmology from EoR/Cosmic Dawn with the SKA," *PoS* **AASKA14** (2015) 012, arXiv:1501.04291 [astro-ph.CO].

[82] D. J. Fixsen *et al.*, "ARCADE 2 Measurement of the Extra-Galactic Sky Temperature at 3-90 GHz," *Astrophys. J.* **734** (2011) 5, arXiv:0901.0555 [astro-ph.CO].

[83] C. Feng and G. Holder, "Enhanced global signal of neutral hydrogen due to excess radiation at cosmic dawn," *Astrophys. J.* **858** no. 2, (2018) L17, arXiv:1802.07432 [astro-ph.CO].

[84] B. Ciardi and P. Madau, "Probing beyond the epoch of hydrogen reionization with 21 centimeter radiation," *Astrophys. J.* **596** (2003) 1–8, arXiv:astro-ph/0303249 [astro-ph].

[85] T. Bringmann, X. Huang, A. Ibarra, S. Vogl, and C. Weniger, "Fermi LAT Search for Internal Bremsstrahlung Signatures from Dark Matter Annihilation," *JCAP* **1207** (2012) 054, arXiv:1203.1312 [hep-ph].

[86] **Fermi-LAT** Collaboration, M. Ackermann *et al.*, "Updated search for spectral lines from Galactic dark matter interactions with pass 8 data from the Fermi Large Area Telescope," *Phys. Rev.* **D91** no. 12, (2015) 122002, arXiv:1506.00013 [astro-ph.HE].

[87] S. J. Clark, J. B. Dent, B. Dutta, and L. E. Strigari, "Indirect detection of the partial p wave via the s wave in the annihilation cross section of dark matter," *Phys. Rev.* **D99** no. 8, (2019) 083003, arXiv:1901.01454 [hep-ph].

[88] **DES, Fermi-LAT** Collaboration, A. Albert *et al.*, "Searching for Dark Matter Annihilation in Recently Discovered Milky Way Satellites with Fermi-LAT," *Astrophys. J.* **834** no. 2, (2017) 110, arXiv:1611.03184 [astro-ph.HE].

[89] **AMS** Collaboration, M. Aguilar *et al.*, "Precision Measurement of the Boron to Carbon Flux Ratio in Cosmic Rays from 1.9 GV to 2.6 TV with the Alpha Magnetic Spectrometer on the International Space Station," *Phys. Rev. Lett.* **117** no. 23, (2016) 231102.

[90] **Fermi-LAT** Collaboration, M. Ackermann *et al.*, "The Fermi Galactic Center GeV Excess and Implications for Dark Matter," *Astrophys. J.* **840** no. 1, (2017) 43, arXiv:1704.03910 [astro-ph.HE].

[91] **AMS-02** Collaboration, S. Caroff, "High Statistics Measurement of the Positron Fraction in Primary Cosmic Rays with the Alpha Magnetic Spectrometer on the International Space Station," in *25th European Cosmic Ray Symposium (ECRS 2016) Turin, Italy, September 04-09, 2016*. 2016. arXiv:1612.09579 [astro-ph.HE]. https://inspirehep.net/record/1507292/files/arXiv:1612.09579.pdf.

[92] A. Cuoco, J. Heisig, M. Korsmeier, and M. Krämer, "Probing dark matter annihilation in the Galaxy with antiprotons and gamma rays," *JCAP* **1710** no. 10, (2017) 053, arXiv:1704.08258 [astro-ph.HE].

[93] I. V. Moskalenko, A. W. Strong, J. F. Ormes, and S. G. Mashnik, "Propagation of secondary antiprotons and cosmic rays in the Galaxy," *Adv. Space Res.* **35** (2005) 156–161, arXiv:astro-ph/0301450 [astro-ph].

[94] X.-L. Chen and M. Kamionkowski, "Particle decays during the cosmic dark ages," *Phys. Rev.* **D70** (2004) 043502, arXiv:astro-ph/0310473 [astro-ph].

[95] S. Kasuya and M. Kawasaki, "Early reionization by decaying particles and cosmic microwave background radiation," *Phys. Rev.* **D70** (2004) 103519, arXiv:astro-ph/0409419 [astro-ph].

[96] E. Pierpaoli, "Decaying particles and the reionization history of the universe," *Phys. Rev. Lett.* **92** (2004) 031301, arXiv:astro-ph/0310375 [astro-ph].

[97] Y. A. Shchekinov and E. O. Vasiliev, "Particle decay in the early universe: predictions for 21 cm," *Mon. Not. Roy. Astron. Soc.* **379** (2007) 1003–1010, arXiv:astro-ph/0604231 [astro-ph].

[98] M. Mapelli, A. Ferrara, and E. Pierpaoli, "Impact of dark matter decays and annihilations on reionzation," *Mon. Not. Roy. Astron. Soc.* **369** (2006) 1719–1724, arXiv:astro-ph/0603237 [astro-ph].

[99] E. Ripamonti, M. Mapelli, and A. Ferrara, "Intergalactic medium heating by dark matter," *Mon. Not. Roy. Astron. Soc.* **374** (2007) 1067–1077, arXiv:astro-ph/0606482 [astro-ph].

[100] M. G. Baring, T. Ghosh, F. S. Queiroz, and K. Sinha, "New Limits on the Dark Matter Lifetime from Dwarf Spheroidal Galaxies using Fermi-LAT," *Phys. Rev.* **D93** no. 10, (2016) 103009, arXiv:1510.00389 [hep-ph].

[101] W. Liu, X.-J. Bi, S.-J. Lin, and P.-F. Yin, "Constraints on dark matter annihilation and decay from the isotropic gamma-ray background," *Chin. Phys.* **C41** no. 4, (2017) 045104, arXiv:1602.01012 [astro-ph.CO].

[102] T. Cohen, K. Murase, N. L. Rodd, B. R. Safdi, and Y. Soreq, "Gamma-ray Constraints on Decaying Dark Matter and Implications for IceCube," *Phys. Rev. Lett.* **119** no. 2, (2017) 021102, arXiv:1612.05638 [hep-ph].

[103] E. Bulbul, M. Markevitch, A. Foster, R. K. Smith, M. Loewenstein, and S. W. Randall, "Detection of An Unidentified Emission Line in the Stacked X-ray spectrum of Galaxy Clusters," *Astrophys. J.* **789** (2014) 13, arXiv:1402.2301 [astro-ph.CO].

[104] A. Boyarsky, O. Ruchayskiy, D. Iakubovskyi, and J. Franse, "Unidentified Line in X-Ray Spectra of the Andromeda Galaxy and Perseus Galaxy Cluster," *Phys. Rev. Lett.* **113** (2014) 251301, arXiv:1402.4119 [astro-ph.CO].

[105] Y. B. Zel'dovich and I. D. Novikov, "The Hypothesis of Cores Retarded during Expansion and the Hot Cosmological Model," *Astronomicheskii Zhurnal* **43** (1966) 758.

[106] Y. B. Zel'dovich and I. D. Novikov, "The Hypothesis of Cores Retarded during Expansion and the Hot Cosmological Model," *Soviet Astronomy* **10** (Feb., 1967) 602.

[107] S. Hawking, "Gravitationally collapsed objects of very low mass," *Mon. Not. Roy. Astron. Soc.* **152** (1971) 75.

[108] B. J. Carr and S. W. Hawking, "Black holes in the early Universe," *Mon. Not. Roy. Astron. Soc.* **168** (1974) 399–415.

[109] S. W. Hawking, "Black hole explosions," *Nature* **248** (1974) 30–31.

[110] A. G. Polnarev and M. Y. Khlopov, "Primordial Black Holes and the ERA of Superheavy Particle Dominance in the Early Universe," *Soviet Astronomy* **25** (Aug., 1981) 406.

[111] M. Yu. Khlopov, "Primordial Black Holes," *Res. Astron. Astrophys.* **10** (2010) 495–528, arXiv:0801.0116 [astro-ph].

[112] J. Georg, G. Şengör, and S. Watson, "Nonthermal WIMPs and primordial black holes," *Phys. Rev.* **D93** no. 12, (2016) 123523, arXiv:1603.00023 [hep-ph].

[113] T. Harada, C.-M. Yoo, K. Kohri, K.-i. Nakao, and S. Jhingan, "Primordial black hole formation in the matter-dominated phase of the Universe," *Astrophys. J.* **833** no. 1, (2016) 61, arXiv:1609.01588 [astro-ph.CO].

[114] B. J. Carr, K. Kohri, Y. Sendouda, and J. Yokoyama, "New cosmological constraints on primordial black holes," *Phys. Rev.* **D81** (2010) 104019, arXiv:0912.5297 [astro-ph.CO].

[115] B. Carr, F. Kuhnel, and M. Sandstad, "Primordial Black Holes as Dark Matter," *Phys. Rev.* **D94** no. 8, (2016) 083504, arXiv:1607.06077 [astro-ph.CO].

[116] A. M. Green, "Microlensing and dynamical constraints on primordial black hole dark matter with an extended mass function," *Phys. Rev.* **D94** no. 6, (2016) 063530, arXiv:1609.01143 [astro-ph.CO].

[117] B. Carr, M. Raidal, T. Tenkanen, V. Vaskonen, and H. Veermae, "Primordial black hole constraints for extended mass functions," *Phys. Rev.* **D96** no. 2, (2017) 023514, arXiv:1705.05567 [astro-ph.CO].

[118] M. Raidal, S. Solodukhin, V. Vaskonen, and H. Veermäe, "Light Primordial Exotic Compact Objects as All Dark Matter," *Phys. Rev.* **D97** no. 12, (2018) 123520, arXiv:1802.07728 [astro-ph.CO].

[119] L. Chen, Q.-G. Huang, and K. Wang, "Constraint on the abundance of primordial black holes in dark matter from Planck data," *JCAP* **1612** no. 12, (2016) 044, arXiv:1608.02174 [astro-ph.CO].

[120] J. Georg and S. Watson, "A Preferred Mass Range for Primordial Black Hole Formation and Black Holes as Dark Matter Revisited," *JHEP* **09** (2017) 138, arXiv:1703.04825 [astro-ph.CO]. [JHEP09,138(2017)].

[121] R. J. Nemiroff, G. F. Marani, J. P. Norris, and J. T. Bonnell, "Limits on the cosmological abundance of supermassive compact objects from a millilensing search in gamma-ray burst data," *Phys. Rev. Lett.* **86** (2001) 580, arXiv:astro-ph/0101488 [astro-ph].

[122] K. Griest, A. M. Cieplak, and M. J. Lehner, "New Limits on Primordial Black Hole Dark Matter from an Analysis of Kepler Source Microlensing Data," *Phys. Rev. Lett.* **111** no. 18, (2013) 181302.

[123] M. Ricotti, J. P. Ostriker, and K. J. Mack, "Effect of Primordial Black Holes on the Cosmic Microwave Background and Cosmological Parameter Estimates," *Astrophys. J.* **680** (2008) 829, arXiv:0709.0524 [astro-ph].

[124] Y. Ali-Haïmoud and M. Kamionkowski, "Cosmic microwave background limits on accreting primordial black holes," *Phys. Rev.* **D95** no. 4, (2017) 043534, arXiv:1612.05644 [astro-ph.CO].

[125] D. Gaggero, G. Bertone, F. Calore, R. M. T. Connors, M. Lovell, S. Markoff, and E. Storm, "Searching for Primordial Black Holes in the radio and X-ray sky," *Phys. Rev. Lett.* **118** no. 24, (2017) 241101, arXiv:1612.00457 [astro-ph.HE].

[126] K. J. Mack and D. H. Wesley, "Primordial black holes in the Dark Ages: Observational prospects for future 21cm surveys," arXiv:0805.1531 [astro-ph].

[127] V. Poulin, J. Lesgourgues, and P. D. Serpico, "Cosmological constraints on exotic injection of electromagnetic energy," *JCAP* **1703** no. 03, (2017) 043, arXiv:1610.10051 [astro-ph.CO].

[128] P. Stöcker, M. Krämer, J. Lesgourgues, and V. Poulin, "Exotic energy injection with ExoCLASS: Application to the Higgs portal model and evaporating black holes," *JCAP* **1803** no. 03, (2018) 018, arXiv:1801.01871 [astro-ph.CO].

[129] H. Tashiro and N. Sugiyama, "Constraints on Primordial Black Holes by Distortions of Cosmic Microwave Background," *Phys. Rev.* **D78** (2008) 023004, arXiv:0801.3172 [astro-ph].

[130] L. Zhang, X. Chen, M. Kamionkowski, Z.-g. Si, and Z. Zheng, "Constraints on radiative dark-matter decay from the cosmic microwave background," *Phys. Rev.* **D76** (2007) 061301, arXiv:0704.2444 [astro-ph].

[131] J. H. MacGibbon and B. R. Webber, "Quark and gluon jet emission from primordial black holes: The instantaneous spectra," *Phys. Rev.* **D41** (1990) 3052–3079.

[132] J. H. MacGibbon, "Quark and gluon jet emission from primordial black holes. 2. The Lifetime emission," *Phys. Rev.* **D44** (1991) 376–392.

[133] A. Barnacka, J. F. Glicenstein, and R. Moderski, "New constraints on primordial black holes abundance from femtolensing of gamma-ray bursts," *Phys. Rev.* **D86** (2012) 043001, arXiv:1204.2056 [astro-ph.CO].

[134] G. Weidenspointner, *The Origin of the Cosmic Gamma-Ray Background in the COMPTEL Energy Range*. PhD thesis, Technical University of Munich, 1999.

[135] J. Zavala, M. Vogelsberger, and S. D. M. White, "Relic density and CMB constraints on dark matter annihilation with Sommerfeld enhancement," *Phys. Rev.* **D81** (2010) 083502, arXiv:0910.5221 [astro-ph.CO].

[136] L. Goodenough and D. Hooper, "Possible Evidence For Dark Matter Annihilation In The Inner Milky Way From The Fermi Gamma Ray Space Telescope," arXiv:0910.2998 [hep-ph].

[137] D. Hooper and L. Goodenough, "Dark Matter Annihilation in The Galactic Center As Seen by the Fermi Gamma Ray Space Telescope," *Phys. Lett.* **B697** (2011) 412–428, arXiv:1010.2752 [hep-ph].

[138] **Fermi-LAT** Collaboration, M. Ajello *et al.*, "Fermi-LAT Observations of High-Energy γ-Ray Emission Toward the Galactic Center," *Astrophys. J.* **819** no. 1, (2016) 44, arXiv:1511.02938 [astro-ph.HE].

[139] C. Karwin, S. Murgia, T. M. P. Tait, T. A. Porter, and P. Tanedo, "Dark Matter Interpretation of the Fermi-LAT Observation Toward the Galactic Center," *Phys. Rev.* **D95** no. 10, (2017) 103005, arXiv:1612.05687 [hep-ph].

[140] M.-Y. Cui, Q. Yuan, Y.-L. S. Tsai, and Y.-Z. Fan, "Possible dark matter annihilation signal in the AMS-02 antiproton data," *Phys. Rev. Lett.* **118** no. 19, (2017) 191101, arXiv:1610.03840 [astro-ph.HE].

[141] M. Cirelli, P. Panci, K. Petraki, F. Sala, and M. Taoso, "Dark Matter's secret liaisons: phenomenology of a dark U(1) sector with bound states," *JCAP* **1705** no. 05, (2017) 036, arXiv:1612.07295 [hep-ph].

[142] L.-B. Jia, "Interpretation of the gamma-ray excess and AMS-02 antiprotons: Velocity dependent dark matter annihilations," *Phys. Rev.* **D96** no. 5, (2017) 055009, arXiv:1703.06938 [hep-ph].

[143] G. C. Yalcin and C. Beck, "Generalized statistical mechanics of cosmic rays: Application to positron-electron spectral indices," *Sci. Rep.* **8** no. 1, (2018) 1764, arXiv:1705.01334 [astro-ph.HE].

[144] B. Eiteneuer, A. Goudelis, and J. Heisig, "The inert doublet model in the light of Fermi-LAT gamma-ray data: a global fit analysis," *Eur. Phys. J.* **C77** no. 9, (2017) 624, arXiv:1705.01458 [hep-ph].

[145] G. Arcadi, F. S. Queiroz, and C. Siqueira, "The Semi-Hooperon: Gamma-ray and anti-proton excesses in the Galactic Center," *Phys. Lett.* **B775** (2017) 196–205, arXiv:1706.02336 [hep-ph].

[146] **Fermi-LAT, MAGIC** Collaboration, M. L. Ahnen *et al.*, "Limits to dark matter annihilation cross-section from a combined analysis of MAGIC and Fermi-LAT observations of dwarf satellite galaxies," *JCAP* **1602** no. 02, (2016) 039, arXiv:1601.06590 [astro-ph.HE].

[147] **VERITAS** Collaboration, S. Archambault *et al.*, "Dark Matter Constraints from a Joint Analysis of Dwarf Spheroidal Galaxy Observations with VERITAS," *Phys. Rev.* **D95** no. 8, (2017) 082001, arXiv:1703.04937 [astro-ph.HE].

[148] B. Dutta, Y. Gao, T. Ghosh, and L. E. Strigari, "Confronting Galactic center and dwarf spheroidal gamma-ray observations with cascade annihilation models," *Phys. Rev.* **D92** no. 7, (2015) 075019, arXiv:1508.05989 [hep-ph].

[149] **Planck** Collaboration, N. Aghanim *et al.*, "Planck 2018 results. VI. Cosmological parameters," arXiv:1807.06209 [astro-ph.CO].

[150] P. Madau, A. Meiksin, and M. J. Rees, "21-CM tomography of the intergalactic medium at high redshift," *Astrophys. J.* **475** (1997) 429, arXiv:astro-ph/9608010 [astro-ph].

[151] L. D. Landau and E. M. Lifshitz, *Quantum mechanics: non-relativistic theory.* Pergamon Press, 1959.

[152] H. Goldberg, "Constraint on the Photino Mass from Cosmology," *Phys. Rev. Lett.* **50** (1983) 1419. [,219(1983)].

[153] N. F. Bell, J. B. Dent, A. J. Galea, T. D. Jacques, L. M. Krauss, and T. J. Weiler, "W/Z Bremsstrahlung as the Dominant Annihilation Channel for Dark Matter, Revisited," *Phys. Lett.* **B706** (2011) 6–12, arXiv:1104.3823 [hep-ph].

[154] L. Bergstrom, "Radiative Processes in Dark Matter Photino Annihilation," *Phys. Lett.* **B225** (1989) 372–380.

[155] R. Flores, K. A. Olive, and S. Rudaz, "Radiative Processes in Lsp Annihilation," *Phys. Lett.* **B232** (1989) 377–382.

[156] E. A. Baltz and L. Bergstrom, "Detection of leptonic dark matter," *Phys. Rev.* **D67** (2003) 043516, arXiv:hep-ph/0211325 [hep-ph].

[157] T. Bringmann, L. Bergstrom, and J. Edsjo, "New Gamma-Ray Contributions to Supersymmetric Dark Matter Annihilation," *JHEP* **01** (2008) 049, arXiv:0710.3169 [hep-ph].

[158] L. Bergstrom, T. Bringmann, and J. Edsjo, "New Positron Spectral Features from Supersymmetric Dark Matter - a Way to Explain the PAMELA Data?," *Phys. Rev.* **D78** (2008) 103520, arXiv:0808.3725 [astro-ph].

[159] V. Barger, Y. Gao, W. Y. Keung, and D. Marfatia, "Generic dark matter signature for gamma-ray telescopes," *Phys. Rev.* **D80** (2009) 063537, arXiv:0906.3009 [hep-ph].

[160] F. S. Queiroz, C. E. Yaguna, and C. Weniger, "Gamma-ray Limits on Neutrino Lines," *JCAP* **1605** no. 05, (2016) 050, arXiv:1602.05966 [hep-ph].

[161] N. F. Bell, J. B. Dent, T. D. Jacques, and T. J. Weiler, "Electroweak Bremsstrahlung in Dark Matter Annihilation," *Phys. Rev.* **D78** (2008) 083540, arXiv:0805.3423 [hep-ph].

[162] J. Kumar and D. Marfatia, "Matrix element analyses of dark matter scattering and annihilation," *Phys. Rev.* **D88** no. 1, (2013) 014035, arXiv:1305.1611 [hep-ph].

[163] N. F. Bell, J. B. Dent, T. D. Jacques, and T. J. Weiler, "W/Z Bremsstrahlung as the Dominant Annihilation Channel for Dark Matter," *Phys. Rev.* **D83** (2011) 013001, arXiv:1009.2584 [hep-ph].

[164] P. Ciafaloni, M. Cirelli, D. Comelli, A. De Simone, A. Riotto, and A. Urbano, "On the Importance of Electroweak Corrections for Majorana Dark Matter Indirect Detection," *JCAP* **1106** (2011) 018, arXiv:1104.2996 [hep-ph].

[165] M. Garny, A. Ibarra, and S. Vogl, "Antiproton constraints on dark matter annihilations from internal electroweak bremsstrahlung," *JCAP* **1107** (2011) 028, arXiv:1105.5367 [hep-ph].

[166] M. Garny, A. Ibarra, and S. Vogl, "Dark matter annihilations into two light fermions and one gauge boson: General analysis and antiproton constraints," *JCAP* **1204** (2012) 033, arXiv:1112.5155 [hep-ph].

[167] J. Kumar, J. Liao, and D. Marfatia, "Dark matter annihilation with s-channel internal Higgsstrahlung," *Phys. Lett.* **B759** (2016) 277–281, arXiv:1605.00611 [hep-ph].

[168] N. F. Bell, Y. Cai, J. B. Dent, R. K. Leane, and T. J. Weiler, "Enhancing Dark Matter Annihilation Rates with Dark Bremsstrahlung," *Phys. Rev.* **D96** no. 2, (2017) 023011, arXiv:1705.01105 [hep-ph].

[169] J. F. Beacom, N. F. Bell, and G. D. Mack, "General Upper Bound on the Dark Matter Total Annihilation Cross Section," *Phys. Rev. Lett.* **99** (2007) 231301, arXiv:astro-ph/0608090 [astro-ph].

[170] A. Albert *et al.*, "Results from the search for dark matter in the Milky Way with 9 years of data of the ANTARES neutrino telescope," *Phys. Lett.* **B769** (2017) 249–254, arXiv:1612.04595 [astro-ph.HE].

[171] **IceCube** Collaboration, M. G. Aartsen *et al.*, "Search for Neutrinos from Dark Matter Self-Annihilations in the center of the Milky Way with 3 years of IceCube/DeepCore," *Eur. Phys. J.* **C77** no. 9, (2017) 627, arXiv:1705.08103 [hep-ex].

[172] C. El Aisati, C. Garcia-Cely, T. Hambye, and L. Vanderheyden, "Prospects for discovering a neutrino line induced by dark matter annihilation," *JCAP* **1710** no. 10, (2017) 021, arXiv:1706.06600 [hep-ph].

[173] **ATLAS** Collaboration, M. Aaboud *et al.*, "Search for electroweak production of supersymmetric states in scenarios with compressed mass spectra at $\sqrt{s} = 13$ TeV with the ATLAS detector," *Phys. Rev.* **D97** no. 5, (2018) 052010, arXiv:1712.08119 [hep-ex].

[174] **ALEPH** Collaboration, A. Heister *et al.*, "Search for scalar leptons in e+ e- collisions at center-of-mass energies up to 209-GeV," *Phys. Lett.* **B526** (2002) 206–220, arXiv:hep-ex/0112011 [hep-ex].

[175] **DELPHI** Collaboration, J. Abdallah *et al.*, "Searches for supersymmetric particles in e+ e- collisions up to 208-GeV and interpretation of the results within the MSSM," *Eur. Phys. J.* **C31** (2003) 421–479, arXiv:hep-ex/0311019 [hep-ex].

[176] **L3** Collaboration, P. Achard *et al.*, "Search for scalar leptons and scalar quarks at LEP," *Phys. Lett.* **B580** (2004) 37–49, arXiv:hep-ex/0310007 [hep-ex].

[177] **OPAL** Collaboration, G. Abbiendi *et al.*, "Search for anomalous production of dilepton events with missing transverse momentum in e+ e- collisions at s**(1/2) = 183-Gev to 209-GeV," *Eur. Phys. J.* **C32** (2004) 453–473, arXiv:hep-ex/0309014 [hep-ex].

[178] **CMS** Collaboration, A. M. Sirunyan *et al.*, "Search for supersymmetry in events with a τ lepton pair and missing transverse momentum in proton-proton collisions at $\sqrt{s} = 13$ TeV," *JHEP* **11** (2018) 151, arXiv:1807.02048 [hep-ex].

[179] G. Belanger, F. Boudjema, A. Pukhov, and A. Semenov, "MicrOMEGAs: A Program for calculating the relic density in the MSSM," *Comput. Phys. Commun.* **149** (2002) 103–120, arXiv:hep-ph/0112278 [hep-ph].

[180] G. Belanger, F. Boudjema, A. Pukhov, and A. Semenov, "micrOMEGAs: Version 1.3," *Comput. Phys. Commun.* **174** (2006) 577–604, arXiv:hep-ph/0405253 [hep-ph].

[181] G. D. Coughlan, W. Fischler, E. W. Kolb, S. Raby, and G. G. Ross, "Cosmological Problems for the Polonyi Potential," *Phys. Lett.* **131B** (1983) 59–64.

[182] T. Banks, D. B. Kaplan, and A. E. Nelson, "Cosmological implications of dynamical supersymmetry breaking," *Phys. Rev.* **D49** (1994) 779–787, arXiv:hep-ph/9308292 [hep-ph].

[183] B. de Carlos, J. A. Casas, F. Quevedo, and E. Roulet, "Model independent properties and cosmological implications of the dilaton and moduli sectors of 4-d strings," *Phys. Lett.* **B318** (1993) 447–456, arXiv:hep-ph/9308325 [hep-ph].

[184] B. S. Acharya, P. Kumar, K. Bobkov, G. Kane, J. Shao, and S. Watson, "Non-thermal Dark Matter and the Moduli Problem in String Frameworks," *JHEP* **06** (2008) 064, arXiv:0804.0863 [hep-ph].

[185] B. Dutta, L. Leblond, and K. Sinha, "Mirage in the Sky: Non-thermal Dark Matter, Gravitino Problem, and Cosmic Ray Anomalies," *Phys. Rev.* **D80** (2009) 035014, arXiv:0904.3773 [hep-ph].

[186] R. Allahverdi, M. Cicoli, B. Dutta, and K. Sinha, "Nonthermal dark matter in string compactifications," *Phys. Rev.* **D88** no. 9, (2013) 095015, arXiv:1307.5086 [hep-ph].

[187] M. Dine, L. Randall, and S. D. Thomas, "Baryogenesis from flat directions of the supersymmetric standard model," *Nucl. Phys.* **B458** (1996) 291–326, arXiv:hep-ph/9507453 [hep-ph].

[188] T. Moroi and L. Randall, "Wino cold dark matter from anomaly mediated SUSY breaking," *Nucl. Phys.* **B570** (2000) 455–472, arXiv:hep-ph/9906527 [hep-ph].

[189] L. Aparicio, M. Cicoli, B. Dutta, F. Muia, and F. Quevedo, "Light Higgsino Dark Matter from Non-thermal Cosmology," *JHEP* **11** (2016) 038, arXiv:1607.00004 [hep-ph].

[190] L. E. Strigari, J. F. Beacom, T. P. Walker, and P. Zhang, "The Concordance Cosmic Star Formation Rate: Implications from and for the supernova neutrino and gamma ray backgrounds," *JCAP* **0504** (2005) 017, arXiv:astro-ph/0502150 [astro-ph].

[191] P. Ruiz-Lapuente, L.-S. The, D. Hartmann, M. Ajello, R. Canal, F. K. Röpke, S. T. Ohlmann, and W. Hillebrandt, "The origin of the cosmic gamma-ray background in the MeV range," *Astrophys. J.* **820** no. 2, (2016) 142, arXiv:1502.06116 [astro-ph.HE].

[192] S. Horiuchi and J. F. Beacom, "Revealing Type Ia supernova physics with cosmic rates and nuclear gamma rays," *Astrophys. J.* **723** (2010) 329–341, arXiv:1006.5751 [astro-ph.CO].

[193] **e-ASTROGAM** Collaboration, A. De Angelis *et al.*, "The e-ASTROGAM mission," *Exper. Astron.* **44** no. 1, (2017) 25–82, arXiv:1611.02232 [astro-ph.HE].